Hydrogen Effect on Dislocation Motion in Fe and Ferritic Alloys

Shuai Wang

Division of Materials Science, Graduate School of Engineering

Hokkaido University

A thesis submitted for the degree of

PhilosophiæDoctor (PhD)

2013/10

1. Reviewer: Prof. Somei Ohnuki

2. Reviewer: Prof. Seiji Miura

3. Reviewer: Prof. Kazuaki Sasaki

Day of the defense:

Signature from head of PhD committee:

Abstract

This dissertation contains research work attempting to solve many unknown problems in hydrogen embrittlement phenomenon of BCC iron. Experimental and computational methods have been employed and the dislocation motion under hydrogen environment are investigated.

To evaluate the hydrogen effect on coupled evolution of dislocation velocity and mobile dislocation density in Fe-based alloys, thermal activation parameters and dislocations structures were obtained using repeated stress relaxation tests on pure iron, Fe-8Cr alloy and F82H (IEA heat) steel. For all of the samples, the rates of stress relaxation are increased by hydrogen. Referring to constant strain, hydrogen charging decreases the thermal activation volume, internal stress ratio, and exhausting rate of mobile dislocation density.

In pure iron, The effective activation volume and the thermal stress were determined at different hydrogen concentrations. The effective activation volume decreases immediately with cathodic charging. At high hydrogen concentrations, the activation volume decreases to lower level and the thermal stress increases rapidly. The density of mobile dislocations in the hydrogen-charged iron has lower exhausting rate than the hydrogen-free one. The average dislocation velocity increases as a function of hydrogen concentration. By using transmission electron microscopy (TEM), hydrogen-induced tangled dislocations are found, which indicates that the repulsive stress field between dislocations becomes weak. Hydrogen has two aspect effect in these metals: shielding the dislocation-barrier interaction due to hydrogen

concentration difference; impeding dislocation motion in low concentration due to solute-solution effect and the produced tangled dislocation. Normally the softening will be observed in well annealed steel. However, the two-aspect effect may invoke increase of flow stress in some case, which is depending on the deformation history, surface condition and internal structure of metals.

In Fe-8Cr alloy and F82H steel, due to the existing of precipitates, the hydrogen concentration is 10 times and 100 times more than in pure iron respectively. hydrogen enhanced softening leads to tangled and polygonized dislocation structures along precipitates. A general expression of hydrogen-induced thermal activation energy is derived. The activation energies is reduced in pure iron, while in Fe-8Cr and F82H steel, the activation energies are almost stable on account of the pinning effect of precipitates. The short-range interaction of dislocation and energy barrier is the key factor dominating the hydrogen-dislocation motion in BCC metals. This interaction varies the thermal activation energy in a narrow range, but makes the dislocations be tangled or network or even cell structures. The mechanical property changes mainly due to the organised dislocation structures in local area.

By using the density functional theory, hydrogen atoms are found to increase the density of free electrons in the simulation cell and have bonding interaction with Fe atom. The increased electron density improves metallic character of iron and enhances softening phenomenon observed by stress relaxation tests. Caused by anisotropic strain components of hydrogen atoms in the tetrahedral sites, elastic interaction for hydrogen with screw dislocation has been found.

Employing a density function theory based embedded-atom method potentials, the evolution of edge and screw dislocation core structures are calculated at different hydrogen concentrations. The hydrogen-screw interaction predicted by the density functional theory has been proved. The core energy and Peierls potential of the dislocations are

reduced by hydrogen. A broaden-core and a quasi-split core structure are observed for edge and screw dislocation respectively. The screw dislocation and hydrogen interaction in body-centred cubic iron is not due to the change of elastic modulus, but the variation of dislocation core structure. The short-range interaction predict by simulation coincides with our experimental work.

While we look not at the things which are seen, but at the things which are not seen: for the things which are seen are temporal; but the things which are not seen are eternal.

2 Corinthians 4:18

Acknowledgements

It is the new dawn! Behind the sheer black cliff rises the golden glory of the invisible sun. Almost falling Christophe at last reaches the bank, and he says to the to the Child : " Here we are! How heavy thou wert! Child, who art thou?" And the Child answers: " I am the day soon to be born"– Jean-Christophe: Journey′s end.

I would like to express my heartfelt gratitude to Professor Naoyuki Hashimoto, Dr. Yongming Wang, Dr. Shigehito Isobe and Professor Somei Ohnuki, who are not only my mentors but dear friends. I could not complete my Ph.D course without their patience, kindness and encouragement. I am proud of my academic roots, in turn, I hope that I can pass on the research values and the dreams that they have given to me.

To Professor Seiji Miura and Professor Kazuaki Sasaki, my examiners who provided encouraging and constructive feedback. I am very indebted to your thoughtful and detailed comments during my doctoral course, and the knowledge you have imparted for the improvement of this work. Your indispensable discussion and advice are very much appreciated.

Many thanks to Ian M Research Group at University of Illinois at Urbanan-Champaign for providing help and suggestions in my research. To Professor Ian Robertson and Professor Petros Sofronis, it has been an honour working with you and I am extremely grateful to have inspiring ideas and discussion from you. To May Martin, Mohsen Dadfarnia, Bai Cui, Stephen House, Virginia McCreary, Benjamin Etink, David Gross, Kaila Morgen, and all my friends in Illinois, thank you for your care and precious help during my staying.

My appreciation likewise extends to my lab family, the informal support and encouragement of many friends here are invaluable. To our dear secretary Kaori Kobayashi, who has supported me by providing research and living assistantship over the three years, I am appreciate you being our source of love and energy. To Takenobu Wakasugi and Norihito Yamaguchi, I am thankful for picking me up at airport when I arrived at first time, guiding me and giving care in my international student life. To the computation team in our lab, a lot of thanks to Keisuke Takahashi for amount of help in my simulation work, also thank you to Seiji Sakuraya, and Katsuhira Kubo who helped the simulation project as graduate students, you are amazing guys and hope you have great prospect in the future. To Tao Ma, Chuanzhi Yu, Chuanxin Liu, Bin Zhou, Hao Yao, Siwei Chen, and Tengfei Zhang, I am glad to have so many Chinese friends during my study in Japan, your warming care and lighting encouragement have helped me getting over homesick, and I could not forget the joy we have together. To Ayaka Umeda, Yuki Nakagawa, Hiroshi Oka, Hiroto Hayashi, Bumsu Park, Kohei Tadaki, Shotaro Chiba, Tomonori Kimura, Hirotaka Homma, Ryo Yamagami, and Yudai Ikarashi, it was a pleasure to share doctoral studies and life with you guys, I will always remember the days we experienced together.

And last, but not least, I would take this opportunity to express the profound gratitude from my deep heart to my beloved parents my parents, grandparents, and and my siblings for their love and continuous support. I am thankful for your great love which has been giving me passion and courage in research work and life.

Contents

List of Figures

List of Tables

Chapter 1

Introduction

1.1 Motivation

Hydrogen almost always has a deleterious effect on mechanical properties a phenomenon generally known as hydrogen embrittlement (HE) (2, 4, 5, 6, 7, 8). The phenomenon of HE of iron and steel has been known since 1874 by Johnson (4), after that it has been found to be pervasive and occurs with few exceptions in all pure metals and their alloys. The HE appears as a loss of toughness that can result in a sudden catastrophic failure of components at loads significantly below the design load. The loss of ductility is frequently accompanied by a change in fracture mode from ductile rupture to cleavage or to intergranular failure. Many attention has been paid on the degradation of ductility (9), fracture toughness (10), and fatigue crack growth properties (11) of steels employed in hydrogen environment, for example, the hydrogen tanks for storage high pressure hydrogen gases (12, 13), and the structure material for next generation fusion reactor (14, 15). In those materials, significant cost and weight savings would be possible by utilizing a higher strength steel. Unfortunately, it is found that hydrogen enhances the susceptibility of high strength steels to brittle fracture, i.e. the higher the strength the higher the susceptibility (16).

Tensile test under simultaneous hydrogen cathodic charging condition is a convenient way for investigating dislocation-hydrogen interaction (17, 18). However, the ordinary quasi-static tensile test only provides a little information of dislocation motion. In pure iron (19, 20, 21, 22) and also Ni, Al and V (23, 24, 25),

contradictory tensile results were found: referring to similar material, hydrogen induces softening effect (flow stress decreasing) in some research works but hardening effect (flow stress increasing) in others. Some researchers believe this variety of results is attributable to unrecoverable damage induced by cathodic charging process (23). A considerable effort has been expended to avoid damage or phase formation on surface. They believe the softening effect is due to high mobility of dislocations with hydrogen. In turn, other researchers give totally different mechanism based on hardening effect (26). Kirchheim and co-workers (27, 28) pointed out that there are actually two aspects of hydrogen effects: on one hand, hydrogen enhances dislocation mobility by decreasing line energy; while, on the other hand, hydrogen has a dragging effect on dislocation, i.e., hydrogen can both resist and enhance dislocation motion.

Fe-based alloys with 8 wt% Cr have been intensively studied during the last decade as candidates for the engineering materials of the first wall and blanket for the fusion reactor. Due to (n,p) transmutation reaction under 14 MeV neutrons irradiation, hydrogen production rate in the first wall materials is predicted to be about 0.9 wppm/dpa (29), and in practical operation, the hydrogen concentration in structural materials would have a quite high value (30). As an example, in low operating temperature of 373 K the hydrogen content in the first wall is tens wppm (31), for the steady state condition of the fusion reactor the temperature is 573 K, an estimate of about 35 wppm of hydrogen was reported (32). By the method of tensile test under hydrogen charging condition, it has been reported that 6 wppm of total hydrogen content in Fe-Cr steel leads to a decrease of reduction of area from 60% to 15% (33).

1.2 Problem statement

In the course of attempts to understand the mechanisms of HE, a wide range of observations have been made on the interaction of hydrogen with dislocations and on changes it induces in the macroscopic stressstrain response of metals. Many of these studies suffer from a number of shortcomings. Since HE presents a serious technical problem, many studies were carried out on commercial alloys, the

complexity of which mitigates against the development of a mechanistic understanding of the phenomena observed. In addition, many studies were not designed to focus on the mechanism(s) by which hydrogen affects plastic behavior, in that they did not take the "special" properties of solute hydrogen into account.

There are many open questions (unknowns) in the HE research:

1. Dislocations-hydrogen interactions:

   a) Dynamics of dislocation-hydrogen interactions hardening vs. softening. (In particular, BCC metal);

   b) Relationship between hydrogen enhanced plasticity and failure and fatigue needs to be investigated, validated and generalized;

   c) Quantification of the hydrogen-dislocation binding energies for a wide range of materials;

   d) Need to understand dislocation core structures and how atomic hydrogen alters the structure - dislocation dynamics.

2. Hydrogen interaction with grain boundaries

   a) Quantitative and predictive understanding of H-boundary interactions;

   b) Need better understanding of grain boundary structure and effect of impurities including hydrogen computer modeling and experiment (advances in electron microscopes offer an exciting opportunity in this regard);

   c) H-binding energies, H segregation and distribution as a function of grain boundary misorientation;

   d) Effect of other segregants, both competitive and synergistic.

3. Hydrogen effects not only on tensile properties but on fatigue need to be understood and predictive models developed.

Many of these questions can not be solved by either one experimental or computational results. Among those questions, the hydrogen-dislocation interaction is the physical basis for interpreting other problems, controlling and mitigating the HE. We will focus on solve the following problems in this dissertation:

1. Finding better methods to evaluate the hydrogen-dislocation interactions;
2. Understanding the hydrogen-induced softening in BCC metal;
3. Relation between hydrogen enhanced plasticity and failure;
4. Binding energy of hydrogen trapped in dislocation and hydrogen interaction with different type of dislocations;
5. Hydrogen influence on the dislocation core structures.

1.3 Research objective

The research objective of this dissertation is to use experimental and computational method to examine the hydrogen and dislocation interaction, hydrogen effect on dislocation motion in iron and ferritic alloys. This research objective is met through designing and performing systematic studies that answer the aforementioned research questions and any subsequent questions that arise.

For the first and second questions, the normal tensile test is easy to be influenced by surface conditions, deformation history, and other factors during experiment. A repeat stress relaxation test is considered for its advantage on understanding the thermally activated behaviour of dislocations. The hydrogen-induced softening will be observed from stress relaxation test at hydrogen charging conditions. The advances in electron microscopes will offer convenience for investigating the variations of dislocation structures at different hydrogen concentrations.

For the third question, Fe-8Cr modelling alloy and commercial steel F82H will be used to study the hydrogen effect in practical cases. because in these metals, precipitates, second phases, grain boundary have much more complicated condition compared with the well annealed pure iron. The failure of these metal in hydrogen environment will give a relation between the dislocation motion and fracture mechanism. The data would be useful for evaluating the resistance of HE in steel production.

The research questions four and five is not easy to be solved by experimental approach. Density functional theory (DFT) and molecular dynamics (MD)

simulations will be employed for prove (or predict) some key points for these two questions. DFT have the advantage for combing the electron structures in angstrom scale with the strain, energy, and dislocation properties in nano-scale, but it is hard to simulate a large scale system. The MD simulation is use for understanding the static and dynamic dislocation behaviour in finite temperature. The simulation work is expected to show clues for interpreting dislocation and hydrogen interactions observed in experiments.

1.4 Dissertation structure

This dissertation is organised as follows. The background of this research, the hydrogen properties in metals, in particular BCC iron, the historical researches of HE, and the existed mechanisms are presented in Chapter 2. The experimental methods (stress relaxation test) and computational information (DFT and MD calculations) are also introduced in Chapter 2.

Corresponding to the research objectives, the research results for this dissertation are broken down into four parts: (1) The research of thermal activation analysis for pure iron, by the means of stress relaxation tests, are placed in the Chapter 3. The yield stress, hydrogen concentrations, activation volume and density of mobile dislocations are discussed based on the concept of existed HE theories. (2) The Chapter 4 is about the ferritic alloys, in which the activation volume and other important information for dislocation thermally activated motion is presented. (3) The DFT simulation about strain field of hydrogen atom in Fe bulk and dislocation hydrogen interaction energy forms the Chapter 5. (4) MD simulation results concerning dislocation behaviour with hydrogen atmosphere is putted in the Chapter 6. The format of each chapter is based on submitted and published journal papers, whereby a "Introduction–Methodology–Results–Discussion–Summary" format is used. In this respect, each chapter is self-contained, although some knowledge of concepts or summary in other chapters may be required.

The significant overall contribution of this dissertation as a whole is summarised in Chapter 7. A summary of each chapter is discussed along with several

important conclusions for each chapter. Last, future research directions that build upon this work are discussed.

Chapter 2

Background and methodology

2.1 Properties of hydrogen in metals

Hydrogen is a ubiquitous element that enters materials from many different sources. Different from other solutes, it have several very important respects. These need to be clarified before we attempt to understand the effects of H on dislocations and mechanical properties.

2.1.1 Diffusion of Hydrogen atoms

Following the result of Hegi, hydrogen diffusion coefficient in normal lattice sites of iron can be described by an Arrhenius relation (34):

$$D = 1.1 \times 10^{-7} \exp(\frac{-6700}{RT}) \tag{2.1}$$

where R is the gas constant (8.31 J $\text{mol}^{-1}\text{K}^{-1}$), and T is temperature. The diffusivity of H is extremely high in the vicinity of 300 K and its behavior is characterized by very small activation enthalpies, as shown in Table 2.1.

In addition to the high H diffusivity, the mobility of H is very dependent on trapping at lattice defects (35). As a consequence, the effective diffusivity, D_{eff} is described by:

$$D_{eff} = D\frac{K}{K + (\alpha N_T)/(\beta N_L)(\theta_T/\theta_L)} \tag{2.2}$$

where D is the lattice diffusivity; N_T is the density of traps; α, the number of hydrogen atoms that can be accommodated per trap; N_L denotes the number

Table 2.1: Hydrogen diffusivity in metals (3).

System	Diffusivity at 300 K (m^2s^{-1})	Activation enthalpy (eV)
Pd (FCC)	3.9×10^{-11}	0.230
Ni (FCC)	6.0×10^{-14}	0.42
Stainless steels (FCC)	1.7×10^{-16}	0.561
Fe (BCC) (34)	7.5×10^{-9}	0.070
Steels (BCC)	1.5×10^{-9}	0.083
V (BCC)	5.4×10^{-9}	0.045

of solvent atoms per unit volume; β, the number of lattice interstitial sites per solvent atom; and $K = \exp(E_B/kT)$, the equilibrium constant with E_B being the trapping (binding) enthalpy, k, Boltzmanns constant, and T, the absolute temperature. Hydrogen occupancy in normal interstitial lattice sites (NILS) θ_L and occupancy in trap sites θ_T in Eq. 2.2 can be related as:

$$\frac{\theta_T}{1-\theta_T} = \frac{\theta_L}{1-\theta_L} \exp \frac{E_B}{kT} \tag{2.3}$$

The experimental values of the binding enthalpies indicate very strong trapping at defects in the temperature range of interest for plasticity and dislocation studies. In systems such as ferritic steels and stainless steels, the H diffusivity is greatly reduced by the presence of traps (3, 35) making it difficult to categorize the effects of H on plasticity without taking this into account, see Table 2.2 for reference. In the vicinity of 300 K, the range of D_{eff} in different steels is about four orders of magnitude lower than in pure metals as a result of trapping effects.

2.1.2 Lattice sites for H atoms

Hydrogen resides in interstitial octahedral (1/2, 0, 0) and tetrahedral sites (1/2, 1/4, 0) in BCC and FCC metals as shown in Fig 2.1 (40). As calculated in Fig 2.1 using 2.52 Åfor diameter of iron atom, the octahedral sites in FCC iron and tetrahedral sites in BCC iron have a larger space for trapping interstitial atoms. In FCC system, octahedral site is alway considered as the trapping site for hydrogen at room temperature (41). In BCC systems, magnetic spin precession studies of muons in iron indicate tetrahedral site occupancy is favored by hydrogen

Table 2.2: Data for trapping of hydrogen in pure iron.

System	Trapping enthalpy (eV)	Reference
H-H	0.046	(36)
H-grain boundary	0.18	(37)
H-dislocation	0.28	(37)
H-Microvoid	0.36	(37)
H-dislocation core (mixed)	0.61	(38)
H-free surface	0.73	(39)
H-Fe_3C interface	0.87	(6)

atoms(42). Also, a number of measurements for Group V-A metals, where higher solubilities make such measurements feasible, indicate tetrahedral site occupancy for hydrogen and deuterium and this is generally accepted as inferential evidence for such site occupancy in iron.

Despite the fact that its atomic size is small, hydrogen has a large partial molal volume of solution, V_H, and hence a large distortion field. Curiously, V_H is a constant fraction of the atomic volume in most bcc systems and is constant, independent of composition, H/M, over the complete range of solid solutions in fcc systems. For BCC systems, V_H=0.17Ω, where Ω is the atomic volume.

In the case of BCC iron which will be the main objective material in this study, the the diameter of tetrahedral site is 0.72 Å. However, hydrogen atom have a diameter of 1.06 Å. This induces a distortion of the host lattice.

2.1.3 Hydrogen atom induced strain field

The octahedral and tetrahedral sites posses a tetragonal symmetry and assuming a coordinate system with the tetragonal axis along the 3-direction, the strain field can be expressed in a form as:

$$S_H = \begin{pmatrix} \epsilon_{11} & 0 & 0 \\ 0 & \epsilon_{22} & 0 \\ 0 & 0 & \epsilon_{33} \end{pmatrix} \tag{2.4}$$

The long rage elastic field can be represented in terms of point force couples centered at the interstitial site (43), and the average strain produced in a

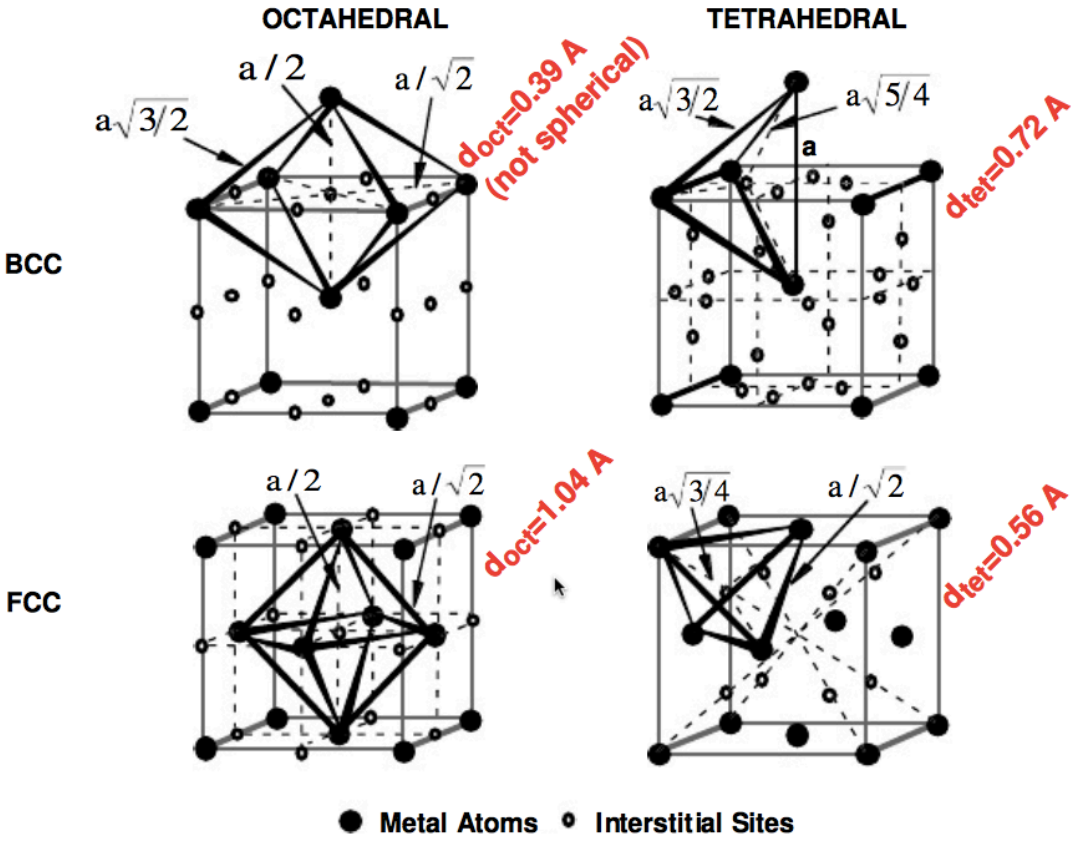

Figure 2.1: Octahedral sites and tetrahedral sites. - Interstitial sites for H atom in BCC and FCC iron (40).

macroscopic body of volume V by a set of couples composed of point force f at positions x is:

$$\epsilon_{ij} = \int_V S_{ijkl} f_k x_l dV \tag{2.5}$$

where S_{ijkl} is the elastic compliance. A single interstitial is represented by a pair of forces f_1 and $-f_1$ at positions $h_1/2$, $-h_1/2$ and two orthogonal pairs f_2 and $-f_2$ at positions $h_2/2$, $-h_2/2$, thus the strains in Eq. 5.1 are:

$$\epsilon_{11} = S_{1111} f_1 h_1 + 2S_{1122} f_2 h_2 \tag{2.6}$$

$$\epsilon_{22} = \epsilon_{33} = S_{2222} f_2 h_2 + S_{1122}(f_1 h_1 + f_2 h_2) \tag{2.7}$$

The dilatation produced by single interstitial is:

$$V_H/V_{Fe} = (S_{1111} + 2S_{1122}) f_1 h_1 + (S_{2222} + 2S_{1122}) f_2 h_2 = (f_1 h_1 + 2 f_2 h_2)/3B \tag{2.8}$$

here B is bulk modulus. Observation of $\epsilon_{11} = \epsilon_{22} = \epsilon_{33}$ can indicate that $f_1 h_1 = f_2 h_2$. If $\epsilon_{11} \neq \epsilon_{22}$, a Snoek type internal friction peak should occur (6).

Because of the small solubility of hydrogen in iron and of the high probability of trapping at defect sites at low temperature, the direct and indirect experiment for strain field of H in Fe are in absence of general agreement. Based on diffuse neutron scattering (44, 45) and Huang diffuse X-ray scattering (45, 46), indicate that $f_1 h_1 = f_2 h_2$. However, the hydrogen-induced Snoek type internal friction peak has been observed in both BCC and FCC iron (47, 48), which indicate that the possibility of $\epsilon_{11} \neq \epsilon_{22}$.

This complication is quit interesting and important in understanding the H-dislocation interaction. As a perfect screw dislocation only expresses shear stress field, it will not interact with the interstitial atoms which have isotropic strain tensor. Following one of the most accepted theory (49), if $\epsilon_{11} = \epsilon_{22}$, the interaction of H with screw dislocations is not due to the deviatoric components of the distortion field but may be attributed to a second-order interaction caused by the local elastic moduli change close to the H interstitial. On the other hand, the interaction with edge dislocations would result from the dilatational components of the distortion field as well as from the local moduli changes. Details of this issue will be discussed further in other sections of this thesis.

2.1.4 Mechanisms for hydrogen embrittlement

In non-hydride-forming systems, nowadays, the changes of mechanical properties caused by hydrogen are described commonly in terms of one of the following models:

1. The decohesion model (hydrogen-induced decohesion, HID), which is based on hydrogen causing a reduction in the strength of atomic bonds (5, 50, 51). According to HID mechanism, hydrogen reduces the cohesive strength of a crystalline compounds along crystallographic plans, grain boundaries, or particle/matrix interfaces, thus degrading the fracture toughness of materials. It should be noted that there is no direct experimental evidence for the HID mechanism.

2. The hydrogen-enhanced dislocation emission model in which hydrogen lowers the surface energy, and this facilitates the injection of dislocations from the surface. Lynch (52) reported that the fracture surfaces of the liquid-metal and gaseous hydrogen embrittled surfaces showed evidence of slip, dimples and tear ridges. These features are all evidence of dislocation activity and led Lynch to propose that crack growth occurred by localized plastic ow in both hydrogen and liquid metal embrittlement. Hydrogen embrittlement, like liquid metal embrittlement, was attributed to the chemisorption of the embrittling element at the crack tip weakening the interatomic bonds, which facilitated the nucleation and emission of dislocations from the crack tip. In this model, crack advance in vacuum occurred not by the emission of dislocations from the crack tip but by dislocations from the bulk moving to and being absorbed at the crack tip.

3. The hydrogen-enhanced localized plasticity mechanism in which the hydrogen atmosphere attached to the dislocation effectively lowers the interactions with elastic obstacles, which means that the shear stress for dislocation motion is reduced. Beachem (53), based on observations of tear ridges and dimples on fracture surfaces of hydrogen embrittled steels, suggested that the effect of hydrogen was to “unlock” rather than “lock” dislocations. That is “it (hydrogen) allows them (dislocations) to multiply or move at reduced

> stresses". Beachem′s model was, until the late 1970s, basically ignored by the scientific community despite evidence on fracture surfaces for ductile processes occurring during hydrogen embrittlement. To explain the effect of hydrogen on dislocation mobility Sirois and Birnbaum (54) and Birnbaum and Sofronis (2) proposed a mechanism in which hydrogen formed an atmosphere around dislocations and other elastic stress centers. The redistribution of the hydrogen atmospheres as the stress-fields merge effectively shields the dislocation from the elastic center, reducing the interaction energy between the dislocation and the obstacle. Consequently, dislocations can move at lower levels of applied stress.

However, with the exception of the hydrogen-enhanced plasticity model, there is a paucity of direct experimental evidence for the other mechanisms (2). The experimental evidence supporting them is associated with *a posteriori* interpretation of macroscopic tests and observations, see Fig. 2.2 as an example, which illustrates TEM observation of aluminum with different hydrogen pressure (These are composite images formed by superimposing a positive image (black) showing the initial position of the dislocation on a negative image (white) showing the final position). That is, the underlying physical processes responsible for the macroscopic effect are interpreted based on anticipated and expected deformation responses rather than through direct observation. Alternatively, they are based on simulations and models that consider simple and ideal situations that remain to be validated experimentally.

Of many suggestions for an explanation of the HE, the mechanism of hydrogen enhanced localized plasticity (HELP) appears to be a most accepted one (2, 54, 55). The HELP mechanism stated that hydrogen-induced screening stress from obstacles including dislocations and precipitates which is the physical basis for the plastic deformation process with hydrogen. A series of experimental observations (56, 57) and theoretical calculations (41, 58) has proved that, hydrogen is able to increase the velocity of dislocation, which leads to heterogeneously localized plastic strain and stress concentrations presumably sufficient to enable the growth of subcritical crack.

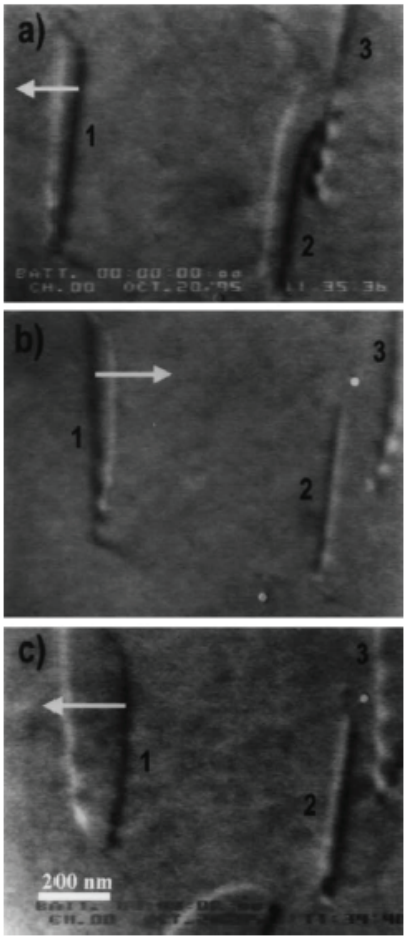

Figure 2.2: Reversal of the direction of motion of dislocations on adding and removing hydrogen from high-purity aluminum. (a) Hydrogen pressure is increased from 15 to 75 torr, (b) decreased from 75 to 9 torr, and (c) increased from 9 to 75 torr (1).

Sofronis and Birnbaum (54) have calculated, by using linear elasticity theory and finite element techniques, the effect of a hydrogen atmosphere on the interaction energy between edge dislocations of the same Burgers vector and between an edge dislocation and a solute atom. In considering the formation of H atmospheres around dislocations, they considered two elastic interactions, a first-order interaction associated with introducing a hydrogen atom in the stress eld of a defect and a second-order interaction that results from the change in local elas-

tic moduli caused by solute hydrogen. The interaction energy of the first-order interaction, W_{int1}, can be expressed as:

$$W_{int1} = \sigma_{ij}^{d} \epsilon_{ij}^{H} \tag{2.9}$$

where σ_{ij}^{d} represents the stress field of the dislocation and ϵ_{ij}^{H} the strain field of the hydrogen solute. The W_{int1} interaction energy varies as $1/r$, where r is the distance from the dislocation. As shown in Fig. 2.3, the hydrogen concentration changes as the distance of two edge dislocation decreases. The chemical concentration differences induces change in strain field of dislocations, and thus the interaction between them.

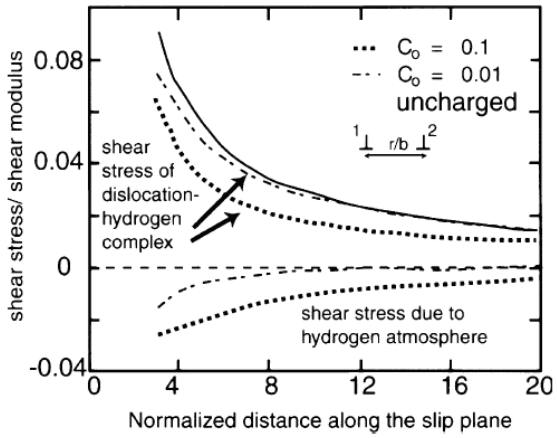

Figure 2.3: Effect of the redistribution of hydrogen on the shear stress experienced by one edge dislocation due to the presence of the other. Both dislocations are on the same slip plane (2).

The interaction energy of the first-order interaction, W_{int2}, can be expressed as:

$$W_{int2} = \frac{1}{2} \epsilon_{ij}^{d} \epsilon_{kl}^{d} V_H (C'_{ijkl} - C_{ijkl}) \tag{2.10}$$

where ϵ_{ij}^{d} and ϵ_{kl}^{d} are the dislocation strain components, and $C'_{ijkl} - C_{ijkl}$ is the difference in elastic constants in the presence of hydrogen. This second-order interaction varies as $1/r^2$, and can lead to a weak, short-range hydrogen atmosphere if $C'_{ijkl} - C_{ijkl} < 0$ or a short-range depletion of hydrogen if $C'_{ijkl} - C_{ijkl} > 0$.

In an isotropic material, the second-order interaction appears through the dependence of the shear and bulk modulus on the solute concentration. The first order interaction will dominate solute interactions with edge dislocations, whereas the second-order interaction describes the interaction of solutes with an isotropic distortion field and a screw dislocation.

These calculations show that the hydrogen-induced elastic shielding causes a short-range decrease in the elastic force between a dislocation and an obstacle. The magnitude of the effect decreases with increasing distance between the dislocation and the obstacle, and increases with increasing hydrogen concentration. Sofronis and Birnbaum calculated that for a H/M concentration of 0.01, the force between two edge dislocations separated by a distance of $3b$ decreases by about 8%. Increasing the hydrogen concentration to H/M=0.1 results in a decrease of 21%. Although the framework of the theory has been built up, investigation for quantifying the hydrogen effect in BCC alloys is still limited (1, 2).

2.2 Thermal activation analysis and the stress relaxation test

To fully explain dislocation-hydrogen interaction mechanism, some researchers realized that thermal activation analysis would be more favorable rather than simple tensile test. Short-range interaction of dislocation with energy barrier (e.g. impurities, solute atoms, forest dislocations) takes place in a small volume that it is strongly influenced by thermal vibrations. As shown in Fig. 2.4, when dislocation pass through a range of energy barriers, it goes from one equilibrium position (x_1) to another(x_2). The swapped area ΔA is the activation area of dislocation, and $V = \Delta A \times b$ is the physical activation volume. This short-range thermally activated process reflects the nature of dislocation-obstacle interaction. There are many ways to estimate thermal activation parameters, e.g. strain rate jump test, stress relaxation test and creep test (59). Stress relaxation test was developed in 1960s (60, 61, 62). It can mainly measure the thermal activation volume and activation energy.

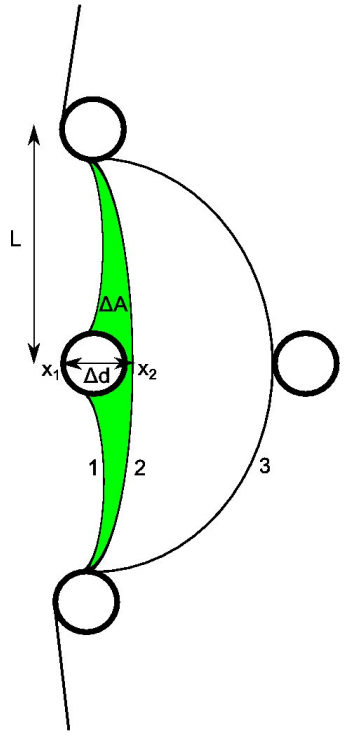

Figure 2.4: Model of thermal activation process.

As illustrated by the arrows in Fig. 2.5, the stress decrease during relaxation is accounted for by an increase in plastic strain γ_p which relieves the elastic strain τ/M, where M is the elastic constant for machine and specimen. The eqnarray of stain for the tensile system can express as:

$$\gamma = \tau/M + \gamma_p \tag{2.11}$$

Its derivative with respect to time is:

$$\dot{\gamma} = \dot{\tau}/M + \dot{\gamma}_p \tag{2.12}$$

During a stress relaxation tests, the tensile machine cross-head is stopped after a yield point, and subsequently the sample is maintained at a constant total strain, while the stress decreases by an amount of $\Delta\tau$ with a negative quantity. When the tensile cross head is stopped, $\dot{\gamma} = 0$. Here the plastic strain rate is proportional to the stress relaxation rate:

$$\dot{\tau}/M = -\dot{\gamma}_p \tag{2.13}$$

In practice, the relaxation curves can exhibit a logarithmic variation of stress with time or a non-logarithmic one. The former case has been reported for a range of materials and deformation conditions and corresponds to a relaxation curve of eqnarray:

$$\Delta\tau = \frac{-kTln(1 + t/C_r)}{V_r} \tag{2.14}$$

where t is the time variable, C_r is the time constant and $\Delta\tau$ is the decay of the stress as a function of time during the stress relaxation. Note that V_r here is the apparent activation volume, not the physical (or effective) one.

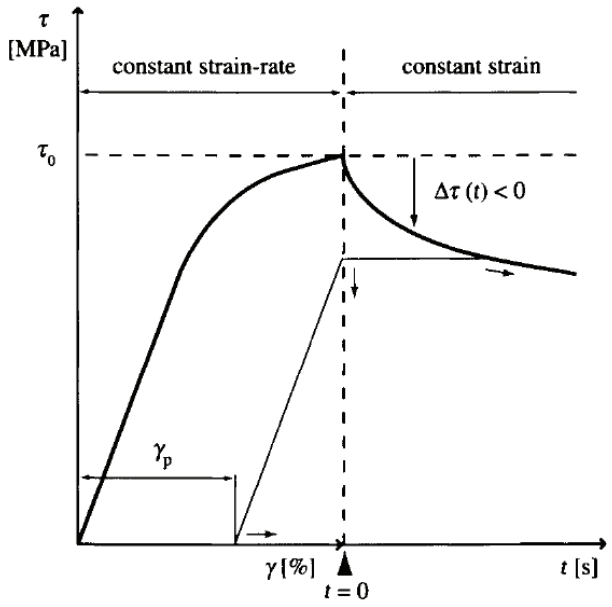

Figure 2.5: Schematic representation of a stress relaxation test. Arrows indicate how some parameters evolve with time.

The single stress relaxation test in early days provided little information of the mobile dislocation density evolution during relaxation, and it couldn't give convincing value of the effective activation volume. After a long time evolution, Spätig invented the repeated stress relaxation test

The essential "trick" of Spätig′s method is that the quasi elastic reloading prevents any substructural changes. As an example in Fig. 2.6, γ_{i2}, and γ_{f2}

which correspond, respectively, to the end of stress relaxation 1 and the onset of stress relaxation 2 can be compared. The same dislocation density is moving in both cases. Therefore, effective activation volume in Fig.2.4 can be calculated as:

$$V_{eff} = \frac{kTln(\dot{\gamma}_i 2)/\dot{\gamma}_f 1}{\Delta\tau} \tag{2.15}$$

which characterizes the stress dependence of the dislocation velocity.(63).

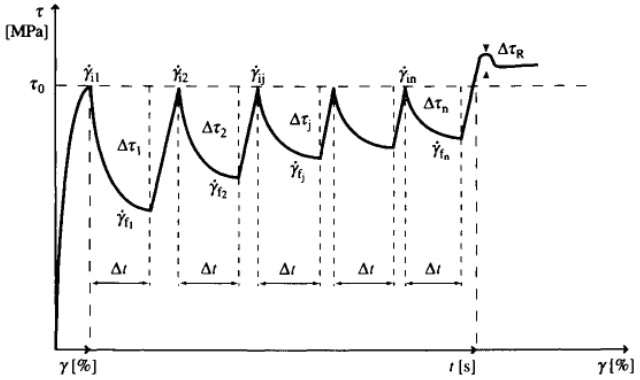

Figure 2.6: The procedure of successive stress relaxations (schematics). Definition of the parameters used. See text.

In the early work of Oriani and Josephic (64), they used stress relaxation test to investigate hydrogen charged AISI 1045 steel and found a obvious relaxation after a critical hydrogen concentration. This result was originally interpreted as hydrogen-induced decohesion and decohesive growth of microvoids. Hydrogen was not thought to have a direct influence on dislocation mobility. After Oriani, though stress relaxation tests of hydrogen charged Ni and Ni-C alloys, Sirois' team found that solute hydrogen atoms have ability to decrease the activation area and the activation enthalpy for dislocation overcoming barriers (54). This result was also considered as a strong evidence for HELP mechanism. Abraham and Altstetter finished a similar work focused on 310s stainless steel (26). They suggested that hydrogen enhances the mobility of slowly moving dislocations which can drag hydrogen atmosphere along.

Nevertheless, in the research topic of hydrogen-dislocation interaction, it is not easy to find more papers using stress relaxation test. Substantial achievements

have been gained by many other characterization methods. TEM in-situ observations over a number of metals have confirmed that hydrogen is able to improve the velocity of dislocations. (1, 56, 57, 65). Some researchers demonstrated that the formation of new dislocation slip planes and nucleation of equilibrium vacancies in hydrogen environment (66, 67). Moreover, it also indicated that hydrogen solutes influences dislocation motion by weakening stress field between dislocations and localized obstacles, named as hydrogen induced shielding effect (or screening effect). A large amount of calculation and simulation work has been presented based on this belief (41, 58). However, detail experimental data for quantifying dislocation velocity, thermal activation energy, and mobile dislocation density evolutions, are still scarce.

2.3 Density functional theory and electron structure analysis

Electronic structure calculations have become an indispensable tool for simulations of condensed-matter systems. Nowadays systems ranging from atoms and small molecules to nanostructures with several hundreds of atoms are studied routinely with density functional theory (DFT).

Since inception of quantum mechanics by Heisenberg, Born, and Jordan in 1925, and Schrödinger in 1926, there were basically two competing approaches to find the energy of a system of electrons. One of the approaches was to derive the many particle wave function $\Psi(\mathbf{r}_1, \mathbf{r}_2, \cdots \mathbf{r}_N, t)$ (where the $\mathbf{r}_1$ denotes the coordinates of the 1st electron, $\mathbf{r}_2$ the 2nd electron, and so on, and t is time) and solve the stationary (time-independent) Schrödinger equation for the system:

$$\hat{H}\Psi_k(\mathbf{r}_1, \mathbf{r}_2, \cdots \mathbf{r}_N) = E_k\Psi_k(\mathbf{r}_1, \mathbf{r}_2, \cdots \mathbf{r}_N) \tag{2.16}$$

(where $\hat{H}$ is the hamiltonian, i.e., the operator of the total energy for the system), and calculate the set of possible wave functions (called eigenfunctions) Ψ_k and corresponding energies (eigenvalues) E_k. This approach is used in tshe traditional *ab-initio* calculations, e.g. Hartree-Hock method.

Another one was rooted in statisticial mechanics and the fundamental variable was the total electron density $\rho(\mathbf{r})$, i.e., the number of electrons per unit volume at a given point in space (e.g., in cartesian coordinates: $\mathbf{r} = (x, y, z)$). In this approach, electrons were treated as particles forming a special gas, called *electron gas*. The special case, the uniform electron gas, corresponds to the $\rho(\mathbf{r}) = const.$ The density functional theory is based on this approach.

Kohn & Sham proposed an ingenious method of marrying wave function and density approach in 1965 (68), which becomes the basis for the modern DFT calculation and made Walter Kohn award the Nobel Prize in Chemistry in 1998. They repartitioned the total energy functional into following parts:

$$E[\rho] = T_0[\rho] + \int \left[\hat{V}_{ext}(\mathbf{r}) + \hat{U}_{cl}(\mathbf{r})\right] \rho(\mathbf{r}) d\mathbf{r} + E_{xc}[\rho] \tag{2.17}$$

where $T_0[\rho]$ is the kinetic energy of electrons in a system which has the same density ρ as the real system, but in which there is no electron-electron interactions (but electrons still interact with nuclei).

$$\hat{U}_{cl}(\mathbf{r}) = \int \frac{\rho(\mathbf{r}')}{|\mathbf{r}' - \mathbf{r}|} d\mathbf{r}' \tag{2.18}$$

is a pure Coulomb ("classical") interaction between electrons. It includes electron self-interaction explicitly, since the corresponding energy is

$$E_{cl}[\rho] = \int \int \frac{\rho(\mathbf{r}')\rho(\mathbf{r})}{|\mathbf{r}' - \mathbf{r}|} d\mathbf{r} d\mathbf{r}' \tag{2.19}$$

and it represents interaction of ρ with itself. $\hat{V}_{ext}(\mathbf{r})$ is the external potential, i.e., potential coming from nuclei:

$$\hat{V}_{ext} = \sum_{\alpha} \frac{-Z_\alpha}{|\mathbf{R}_\alpha - \mathbf{r}|} \tag{2.20}$$

The last functional, $E_{xc}[\rho]$, called exchange-correlation energy.

With DFT theory, the properties of a many-electron system can be determined by using functionals, which in this case is the spatially dependent electron density. Hence the name density functional theory comes from the use of functionals of the electron density. DFT has come to prominence over the last decade as a method potentially capable of very accurate results at low cost, when compared to

traditional methods, such as HartreeFock method aforementioned. In many cases the results of DFT calculations for solid-state systems agree quite satisfactorily with experimental data.

There are many approximation to solve Kohn-Sham equations. In this work, we use a real-space-based implementation of the projector augmented-wave (PAW) method (69), the open-source program package GPAW to investigate the strain field of hydrogen atoms and the correlated electron densities. This code solve the Kohn-Sham equation is done via the "residual minimization method - direct inversion in iterative subspace" (RMM-DIIS) method (70). It is an all-electron method (frozen core approximation) and there is a one to one transformation between the pseudo and all-electron quantities. The detail parameters will be introduced in the corresponding chapter.

2.4 Molecular dynamics and minimum energy path

In the simplest physical terms, molecular dynamics (MD) may be characterized as a method of "particle tracking". Operationally it is a method for generating the trajectories of a system of N particles by direct numerical integration of Newton's eqnarrays of motion, with appropriate specification of an interatomic potential and suitable initial and boundary conditions. MD is an atomistic modeling and simulation method when the particles in question are the atoms which constitute the material of interest. The underlying assumption is that one can treat the ions and electrons as a single, classical, entity. When this is no longer a reasonable approximation, one needs to consider both ion and electron motions. One can then distinguish two versions of MD, classical and *ab initio*, the former for treating atoms as classical entities (position and momentum) and the latter for treating separately the electronic and ionic degrees of freedom, where a wave function description is used for the electrons. In this study, we will use the later one, and an *ab initio* based embedded atom method (EAM) potential is applied.

A common and important problem in theoretical chemistry and in condensed matter physics is the identification of a lowest energy path for a rearrangement

of a group of atoms from one stable configuration to another, such a path is often referred to as the Minimum Energy Path (MEP). The Nudged Elastic Band (NEB) method is used to find reaction pathways when both the initial and final states are known. Using this code, the MEP for any given chemical process may be calculated, however both the initial and final states must be known. The method works by optimizing a number of intermediate images along the reaction path. Each "image" corresponds to a specific geometry of the atoms on their way from the initial to the final state, a snapshot along the reaction path. Each image finds the lowest energy possible while maintaining equal spacing to neighboring images. This constrained optimization is done by adding spring forces along the band between images and by projecting out the component of the force due to the potential perpendicular to the band. Thus, once the energy of this string of images has been minimized, the true MEP is revealed. In this dissertation, the dislocation migration path along $1b$ distance will be calculation by using the NEB method within a EAM potential system.

Chapter 3

Effect of hydrogen on thermally activated motion of dislocations in pure iron

3.1 Introduction

The HELP mechanism states that hydrogen interstitials shield (or weaken) the stress field of dislocations and effectively lower its interactions with barriers (e.g. impurities, solute atoms, forest dislocations), which is the physical basis for the plastic deformation process with hydrogen. TEM *in-situ* experiments on a number of metals (1, 56, 57) have shown that hydrogen can increase the velocity of dislocations and induce shear localization. For these reasons, the resolved shear stress for dislocation motion is reduced (softening). The underlying physical processes responsible for those dislocation-hydrogen interactions are mainly interpreted alternatively by simulations or models which consider ideal situations (41, 58), and remain to be validated experimentally.

Hydrogen mainly affects short-range energy barriers that impede dislocation motion in small volume. Therefore the hydrogen-dislocation interaction is mainly determined by thermal vibrations. In thermally activated process, a swept area resulted from dislocation line overcoming the barriers is termed an activation area. The product of the activation area and Burgers vector (b) is the effective

activation volume. There is a range of ways to estimate thermal activation parameters, including strain rate jump, stress relaxation, and creep tests (71). The stress relaxation test was proposed in the 1960s (60, 61, 62), it mainly measures the thermal activation volume and activation energy. Single stress relaxation tests reveal little information of mobile dislocation densities during relaxation, and provide no generally acceptable value of the effective (or physical) activation volume. A repeated stress relaxation test developed by Spätig (63) has shown advantages in measuring the thermal activation parameters, e.g. effective thermal activation volume (V_{eff}), strain rate sensitivity (m), and mobile dislocation density (ρ_m).

Oriani and Josephic(64) reported large increase in stress relaxation rate after a critical hydrogen concentration by using the single stress relaxation tests on hydrogen charged AISI 1045 steel. However, the results were originally interpreted as a hydrogen-induced decohesive growth of microvoids, and hydrogen was not thought to have a direct influence on the dislocation mobility in the specimens. Based on stress relaxation experiments of Ni and Ni-C alloys, Sirois and Birnbaum suggested that solute hydrogen atoms have the ability of lowering the activation area and activation enthalpy of dislocations (54), which was considered to be an important evidence for the HELP mechanism. Abraham and Altstetter have reported similar work on 310S stainless steel (26), and suggested that hydrogen enhances the mobility of slowly moving dislocations. However, in the case of body-centered cubic (b.c.c.) metal, e.g. iron and ferrite-based alloys, experimental data for quantifying the dislocation velocity (v), V_{eff}, and evolution of (ρ_m) is very limited.

In this part we report thermal activation analysis on pure iron under simultaneous hydrogen cathodic charging conditions, by method of stress relaxation test developed by Spätig (63). The V_{eff} determined from this test is a physical microscopic activation volume and a real signature of the operating deformation mechanism. The ρ_m is monitored during stress relaxation process, and the hydrogen-enhanced dislocation motion is discussed by combining with TEM observation.

3.2 Experimental methodology

Pure iron, purity better than 99.95% (produced by Johnson Matthey Chem. Ltd.) was used as the specimen material. Rods of 5.0 mm diameter were cold rolled to plates and punched into tensile specimens with the shape and dimensions in Fig. 3.1. The punched out specimens were placed in a vacuum in a quartz tube (1×10^{-4} Pa) and then annealed at 873 K for 1 h. Then the specimens were removed from the tube, and to ensure a smooth surface and eliminate stress concentrations on the surface, the specimens were electrochemically polished with Acetic acid: Perchloric acid = 19:1, giving a final specimen thickness of around 0.25 mm. A polymer coating on the ends of the specimens protected these areas from hydrogen charging.

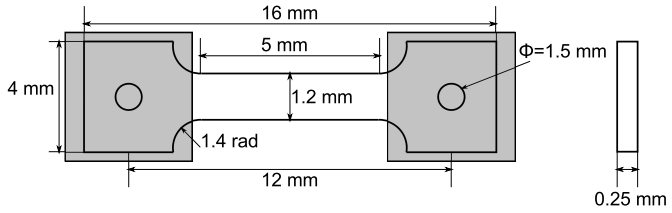

Figure 3.1: Shape and dimensions of the tensile test specimen.

The repeated stress relaxation tests were performed on an Instron 5564 universal test machine (Instron Ltd.) with a electrolytic cell for hydrogen charging, as outlined in Fig. 3.2. The electrolyte for the cathodic charging was 0.5 mol/l H_2SO_4 with 50 g/l Thiourea as a promoter. For the isothermal stress relaxation test, the test temperature was kept on 293 K and the strain rate was set to 1×10^{-4} s^{-1} which ensures hydrogen is transported by dislocations moving at low speed (72). The specimen was initially subjected to 5% plastic deformation (after yield point).Then the tensile cross-head was stopped and this state was maintained for 30s and the strain is constant during relaxation. The stress of the specimen relaxed during this period, and stress data was recorded at 0.3 s intervals. Subsequently the stress at the onset of the previous relaxation was restored before the cross-head was stopped again. Every 30 s in this test is one cycle and which was repeated till no relaxation was recorded in the relaxation stage. The load relaxation due to the machine was obtained with zero-gauge samples and subsequently

subtracted from the stress decay curves. While there is only elastic deformation between end of one cycle and onset of the next cycle, without undesired nucleation of total dislocations, the stress relaxation test gives an information of the mobile dislocation behavior (73). Continuous cathodic charging was applied during the whole of the relaxation progress with cathodic current densities of 5 mA/cm^2 to 75 mA/cm^2 at a interval of 10 mA/cm^2. The cathodic polarization curve of the tensile sample was measured to get the potentials corresponding to the imposed current densities, with a voltage scan rate of 10 mV/s. The surfaces of specimens were carefully examined to establish if there was surface blistering or other irreversible damage after the stress relaxation tests. The stress relaxation tests with the hydrogen-free samples (no cathodic current applied) were conducted at temperatures from 293 K to 373 K, to establish the zero stress thermal activation energy.

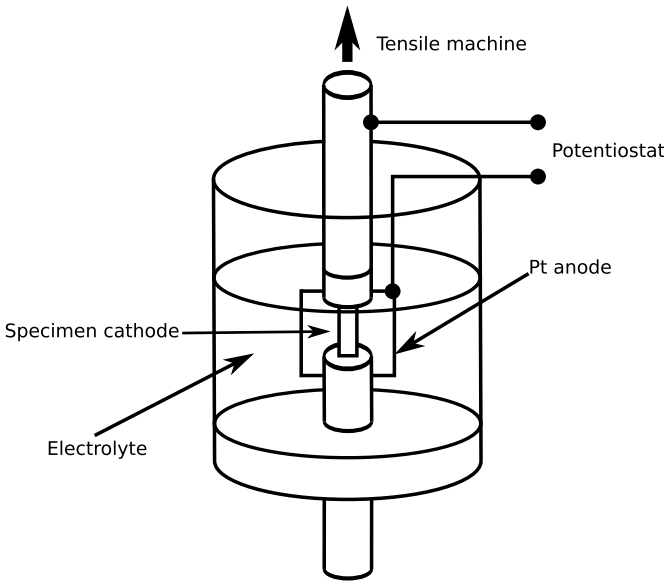

Figure 3.2: Schematic outline of the equipment for the hydrogen charging stress relaxation test.

As the magnetic property of iron influences the observations of dislocations, the sample preparation for the TEM observations in these experiments will be explained as follows (74). One mm diameter disks were punched out of the hydrogen charged areas of the tensile specimens and inserted into 3 mm 316F austenite

stainless steel disks. The hybrid foils were prepared by a Struers Tenuupol-5 double-jet electro-polisher, and subjected to TEM (JEM-2010) observations immediately after the insertion to inhibit surface oxidation. For comparison of the dislocation structures and total dislocation densities, relaxed specimens not subjected to hydrogen charging, specimens with hydrogen charging at current densities of 25 mA/cm^2, 45 mA/cm^2, 75 mA/cm^2 were observed in TEM. In order to investigate if there is multiplication of dislocations during stress relaxation test with simultaneous hydrogen charging condition, ordinary uniaxial strained hydrogen-free specimens with elongations of 5% (same as the onset of stress relaxation) to 30% were also observed.

The shear stress τ and its components are related to the normal stress σ and its corresponding components by Taylor orientation factor, and this paper uses a Taylor factor of 3 for iron (75, 76, 77): $\sigma = 3\tau$, $\dot{\varepsilon} = \dot{\gamma}/3$.

3.3 Results

3.3.1 Hydrogen concentration

The hydrogen concentration is an important parameter for the analysis of repeated transients at different cathodic currents, and should be determined at first. Hydrogen occupancy in normal interstitial lattice sites (NILS) θ_L and occupancy in trap sites θ_T follows the Oriani's theory (35):

$$\frac{\theta_T^{(i)}}{1-\theta_T^{(i)}} = \frac{\theta_L}{1-\theta_L} \exp \frac{E_B^{(i)}}{RT} \tag{3.1}$$

where i denotes the type of trap sites, for well annealed pure iron, there are mainly two: dislocations (d) and grain boundaries (g), $E_B^{(i)}$ represents the trap energy, and R is the gas constant, 8.31 J·mol^{-1}K^{-1}. Hydrogen concentrations in NILS and trapping sites (measured in atoms per unit volume) are phrased as:

$$C_L = \theta_L \beta N_L \tag{3.2}$$

and

$$C_T = \theta_T^{(i)} \alpha^{(i)} N_T \tag{3.3}$$

Table 3.1: Parameters for hydrogen concentration calculations.

Parameter	Value
Lattice site density N_L (m^{-3}) (80)	8.46×10^{28}
Lattice parameter a (m) (80)	2.8865×10^{-10}
$\alpha^{(d)}$ and $\alpha^{(g)}$(81)	1
Lattice sites per solvent atom β	6
Dislocation density (m^{-2})	1.2×10^{14}
Permeation constant φ_0 (78)	3.70×10^{-6}
Diffusion constant $D_0(m^2s^{-1})$ (82)	1.1×10^{-7}
Trap energy (kJ/mol) (6)	$E_B^{(d)} = 30$, $E_B^{(g)} = 50$

respectively, here $\alpha^{(i)}$ is the number of trapping sites per trap, β is the number of interstitial sites per solvent atom, N_L denotes the number of solvent atoms per unit volume, and N_T is the trap density.

At a cathodic current density of i_c, the equilibrium H concentration in lattice sites can be described by the Sievert's law, $C_L = K i_c^{1/2}$. The constant K for cathodic charging with H_2SO_4 has been reported by Johnson and Wu (78, 79):

$$C_L = \frac{\varphi_0 N_A}{D_0} \exp[\frac{-11000(J \cdot mol^{-1})}{RT}] i_c^{1/2} \tag{3.4}$$

where φ_0 is the permeation constant of hydrogen, D_0 is the diffusion constant of hydrogen, and N_A is Avogadro constant. The total hydrogen concentration $C_H = C_L + C_T$.

The parameters for hydrogen concentration calculation are shown in Table 3.1. The hydrogen concentration increases from 7.08 appm to 25.77 appm as cathodic current density increases from 5 mA/cm^2 to 75 mA/cm^2 (Table 3.2). The hydrogen atoms in trapping sites occupy about 15 % of the total hydrogen concentrations.

Table 3.2: Hydrogen concentrations at different cathodic current densities and corresponding yield stresses.

i_c (mA/m^2)	C_H (appm)	C_T (appm)	σ_{YS} (MPa)
0	0	0	179.25
5	7.08	1.24	179.72
15	12.01	1.90	182.11
25	15.33	2.28	183.29
35	17.98	2.54	178.38
45	20.25	2.75	173.35
55	22.27	2.91	171.20
65	24.10	3.05	168.80
75	25.77	3.18	163.94

3.3.2 Evolution of dislocation structures during uniaxial tensile test

The yield stresses (σ_{YS}) at different hydrogen concentrations were obtained on the basis of the average tensile results of at least three tensile specimens (error $\pm$ 3 MPa), and listed in Table 3.2. Yield stress increases 4 MPa at C_H lower than 15.33 appm. Since the increments of yield stress are about at the numerical error obtained by tensile tests, we conclude they can be neglected and therefore the operation of dislocation was hardly influenced at low C_H. At C_H higher than 25.77 appm, σ_{YS} is decreased by more than 10 MPa, indicating the operation of dislocations is encouraged by hydrogen.

The average grain size of iron after heat-treatment was measured to be 74 μm ($\pm 15 \mu m$). The stress-strain curve of the iron by an ordinary uniaxial tensile test in air with strain rate of 1×10^{-4} s^{-1} is plotted in Fig. 3.3. The ordinate axis at right side in Fig. 3.3 shows total dislocation densities at certain strain, which was calculated from related dislocation structures observed by TEM. The TEM images with different strains are illustrated in Fig. 3.4. Fig. 3.4(a) to Fig. 3.4(d) represent microstructures of specimens which were drawn to 5%, 10%, 20%, and 30% respectively. Dislocation density of tensile sample at 30% strain is

over 10 times more than the stress-free sample, with dense of tangling dislocation structures.

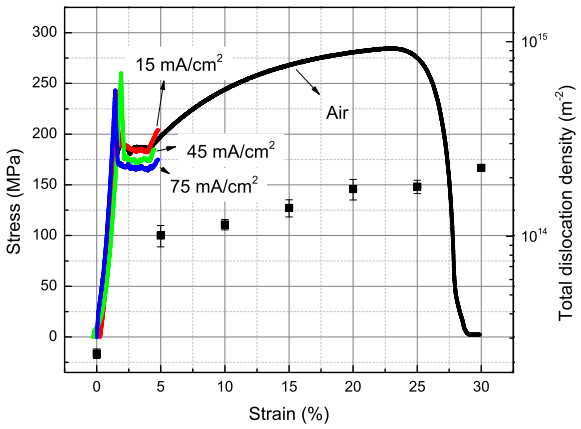

Figure 3.3: Variation of dislocation density during a uniaxial tensile test.

Also stress-strain curve of hydrogen charged specimen is illustrated in Fig. 3.3. In low current density like 15 mA/cm^2, the yield stress and flow stress shows a little increase, which indicates that H could act as a strengthening factor in plastic deformation according to solute-drag mechanism. Up to 45 mA/cm^2 and 75 mA/cm^2 both of the stresses decrease, and H induced softening effect was observed.

3.3.3 Stress relaxation curves

Fig. 3.5 shows stress relaxation curves and indicate that there are apparent differences between the hydrogen-free and hydrogen charged samples. In Fig. 3.5(a), for a specimen not subjected to hydrogen charging, the stress relaxation test can only be repeated for 2 cycles. While in Fig. 3.5(b) with a cathodic current density of 35 mA/cm^2, more than 8 cycles cycles are possible and the relaxation rate in each cycle is larger.

As illustrated in Fig. 3.6(a), stress relaxation can be repeated for more than 50 cycles in 45 mA/cm^2 treated specimens. At 75 mA/cm^2, the 19th cycle is the

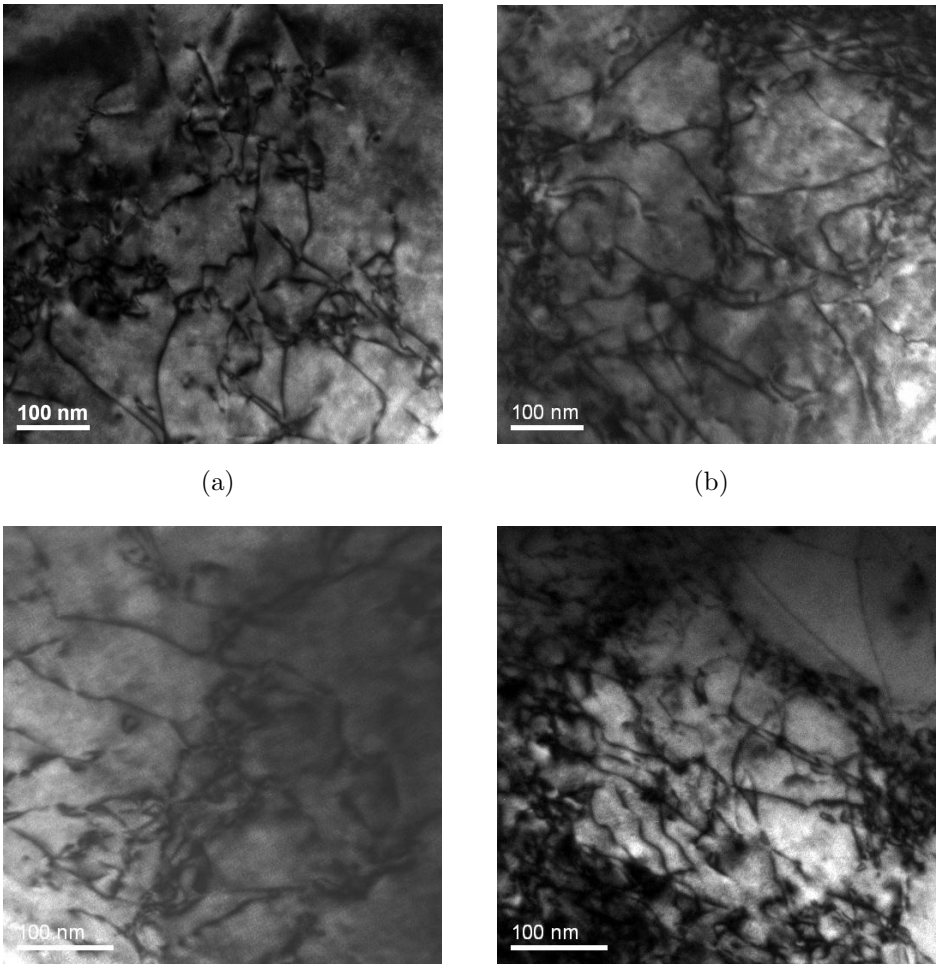

(a) (b)

(c) (d)

Figure 3.4: Dislocation structures at different strain. (a) 5%; (b) 10% (c) 20% (d) 30%.

final cycle of relaxation as shown in as shown in Fig. 3.6(b), as the specimen fractured at the end of the curve under the low strain level.

3.3.4 Thermal activation parameters

The concept of activation volume is central to characterizing thermally activated motion of dislocations in metal. Driven by an effective stress τ_{eff}, a swept area resulting from a dislocation line overcoming short-range obstacles is termed an

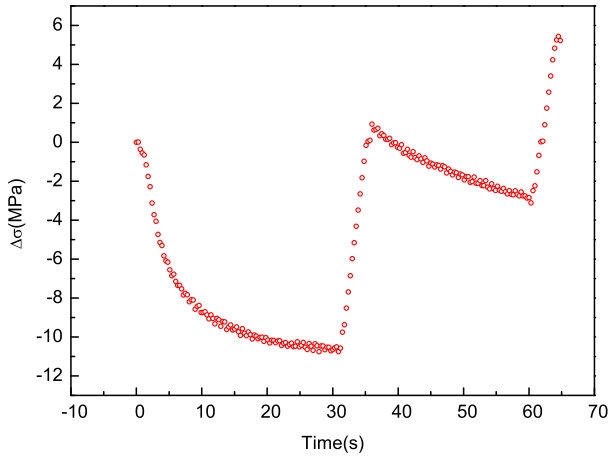

(a)

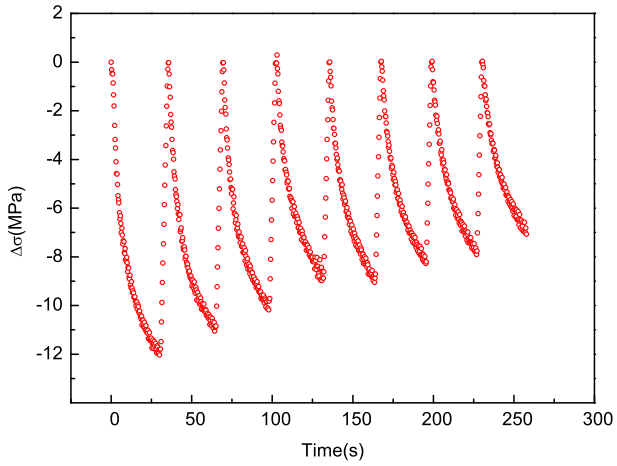

(b)

Figure 3.5: Influence of hydrogen on the stress-time plot of repeated stress relaxation cycles. (a) without hydrogen; (b) with cathodic hydrogen charging at 35 mA/cm^2.

activation area. The product of the activation area and the Burgers vector is the effective activation volume V_{eff}. The effective stress is the source of an effective energy of $\tau_{eff}V_{eff}$. The Gibbs free energy ΔG (or apparent activation energy)

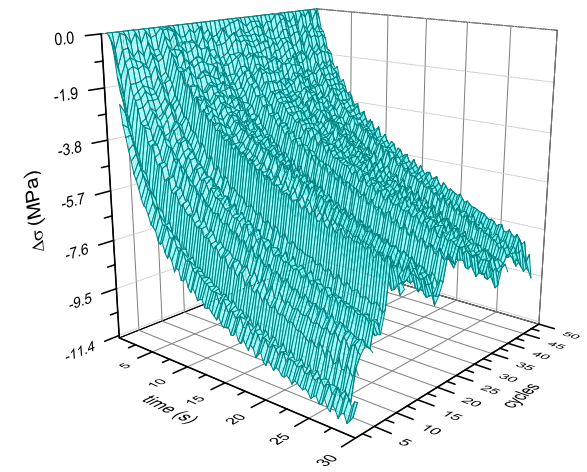

(a)

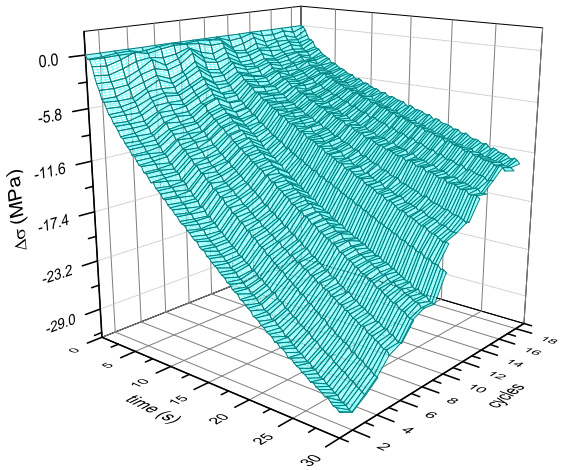

(b)

Figure 3.6: Hydrogen induced relaxation cycles at two cathodic current densities. (a) 45 mA/cm^2; (b) 75 mA/cm^2.

arising from thermal agitation in a stress-assisted thermal activation process is negatively correlated with the effective stress: (59, 83):

$$\Delta G = \Delta F - \tau_{eff} V_{eff} \tag{3.5}$$

where $\Delta F = \Delta G(\tau_{eff} = 0)$, is the activation energy required at zero effective stress. With the above considerations, the rate controlling deformation mechanism of b.c.c. metal under uniaxial tension in a thermally activated process, with negligible backward flow and all short-range obstacles identical, is described by an Arrhenius-type law (84):

$$\dot{\gamma}_p = \dot{\gamma}_0 \exp \frac{-\Delta G}{kT} = \dot{\gamma}_0 \exp \left(-\frac{\Delta F - \tau_{eff} V_{eff}}{kT}\right) \tag{3.6}$$

where k is Boltzmann constant, equal to 1.381×10^{-23} J/K, T is the temperature, and $\dot{\gamma}_0$ is a characteristic strain rate:

$$\dot{\gamma}_0 = \rho_m v_D |\vec{b}|^2 \tag{3.7}$$

here ρ_m represents the mobile dislocation density, $v_D \approx 10^{-13}\mathrm{s}^{-1}$ is the Debye frequency, and $|\vec{b}|$ is Burgers vector of dislocation.

Groh and Conte found that the relaxed apparent stress τ yields a function of strain rate and activation volume (85):

$$\dot{\tau} = K\dot{\gamma}_p + \frac{\ddot{\gamma}_p kT}{\dot{\gamma}_p V_{eff}} \tag{3.8}$$

where K is a plastic strain-hardening coefficient. The apparent activation volume V_a and the effective activation volume V_{eff} yield the relation:

$$V_a = V_{eff}(1 + \frac{K}{M}) \tag{3.9}$$

with the strain-hardening term for the activation volume $V_h = V_{eff}K/M$, the apparent activation volume can be divided into two parts: $V_a = V_{eff} + V_h$.

With Eq. (2.14), the apparent activation volume V_a can be determined from a logarithmic fitting of the $\Delta\tau$-time curve. Note that a single relaxation curve is not sufficient to determine the effective activation volume V_{eff} which is a physically significant parameter in interpreting the true deformation mechanism, and it is necessary to establish V_h from a series of successive curves then V_{eff} can be obtained.

3.3.4.1 Components of applied stress

The external stress τ in stress relaxation test has two components:

$$\tau = \tau_{eff} + \tau_{\mu} \tag{3.10}$$

where τ_{μ} is the internal stress signifying the athermal contribution to the flow stress.

In strain rate controlling plastic deformation, the local effective stress is the driving force for dislocation motion and the internal stress is the resistance against this motion. Supposing an external stress at $t = 0$ is applied to a sample, $\tau = \tau_0$, then after the passage of sufficient time, it may be assumed that τ reaches the average value of internal stress τ_{μ}. The plotting of external stress and time in stress relaxation test was found to follow a hyperbolic expression (86):

$$\tau = \frac{\tau_{\mu} + \delta\tau_0}{t + \delta} \tag{3.11}$$

where t denotes time, and δ is a positive coefficient. The thermal and athermal components of the applied stress can be determined by hyperbolic fitting of the relaxation curve. Based on the external stresses imposed at the beginning of the stress relaxation tests ($\varepsilon = 5\%$), Fig. 3.7(a) shows the stress components allowing an evaluation of the ratios of these stress components.

Bellow 25 mA/cm^2, the increase in the ratio of effective stress is low. The yield stress shows small variations which could result in hardening or softening effects as has been reported and detailed above. As hydrogen concentration increases, up to 35 mA/cm^2 there is a marked reduction in yield stress and a rise in effective stress. Fig. 3.8 illustrates cathodic polarization curve in electrolyte of this study. The potential in the cathodic reaction area decreases gradually towards the minus direct as current density increases, it indicates the variations of mechanical properties are related to the hydrogen concentration directly.

3.3.4.2 Activation volume and strain rate sensitivity

The time derivative of Eq. 2.14 in Section 2.2 gives the stress rate $\dot{\sigma}(t)$. Assuming the stress rate at the beginning of the jth cycle as $\dot{\sigma}_{i,j}$ $(j = 1, 2, 3...)$, and at the end of the cycle as $\dot{\sigma}_{f,j} (j = 1, 2, 3...)$, V_h can be determined after measuring $\dot{\sigma}_{i,j}$

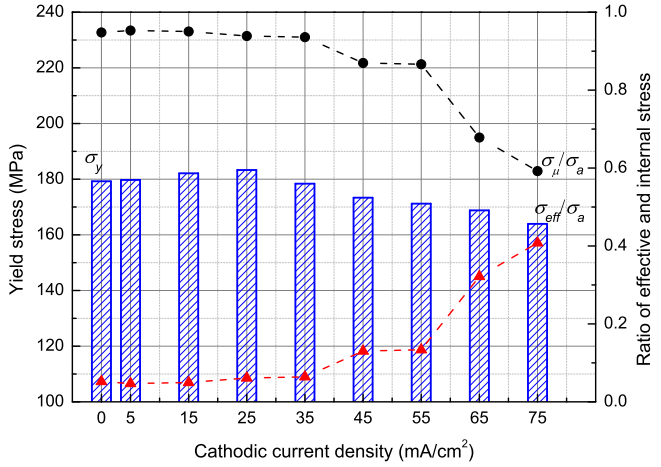

(a)

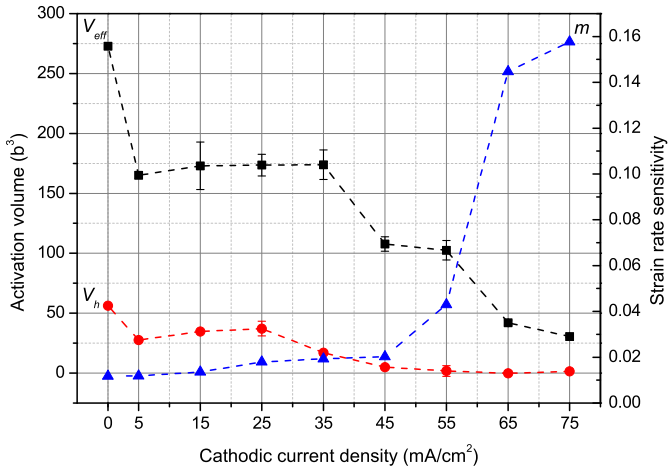

(b)

Figure 3.7: Parameters for thermally activated process of dislocations at different hydrogen concentrations. (a) Yield stress (left ordinate), ratios of effective stress and internal stress compared with total external stress (right ordinate); (b) Activation volume (left ordinate) and strain rate sensitivity coefficient (right ordinate).

and $\dot{\sigma}_{i,j+1}$ from the tangents of the stress-time curve at the onset of a relaxation

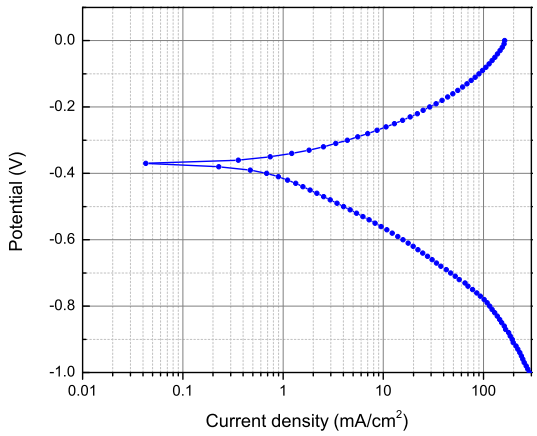

Figure 3.8: Polarization curve of pure iron in the electrolyte used in this study

cycle (63):

$$V_h = kT\frac{\ln\left(\dot{\sigma}_{i,j+1}/\dot{\sigma}_{i,j}\right)}{\Delta\sigma_j}(j = 1, 2, 3...) \tag{3.12}$$

Where $\Delta\sigma_j$ denotes stress drop in the jth cycle. After obtained the apparent activation volume V_a from a logarithmic fitting of the $\Delta\sigma$-time curve, V_{eff} can be determined by Eq. (3.9).

The average dislocation velocity v can be represented by the strain rate sensitivity m,

$$v = (\frac{\sigma}{\sigma_0})^m \tag{3.13}$$

where σ_0 is the stress needed for dislocation moving in a unit speed. Since each stage of stress relaxation test is close to steady state, following Hart's definition of m in a tensile test (87), strain rate sensitivity of bcc iron used in this study can be expressed by an equation as bellow:

$$\mathrm{d}(\ln\sigma) = m\mathrm{d}(\ln\dot{\varepsilon}) \tag{3.14}$$

where σ is applied stress, and $\dot{\varepsilon}$ is the related strain rate. Combining with Eq. 2.13, $\mathrm{d}(\ln\dot{\varepsilon}) = \mathrm{dln}\,(-\dot{\sigma})$, one can find:

$$m = \frac{\mathrm{d}(\ln\sigma)}{\mathrm{d}[\ln\left(-\dot{\sigma}\right)]} \tag{3.15}$$

m can be derived from the slope of a linear fitting of $[\ln(-\dot{\sigma})]$ against $\ln\sigma$.

The Burgers vector $|\vec{b}| = 0.248$ nm for iron was used in the calculation of the activation volume. The activation volume and strain rate sensitivity coefficient at different current densities are shown in Fig. 3.7(b). Generally, across the whole of the hydrogen concentration range, the activation volume decreases with hydrogen concentration increases. The hardening term of an activation volume V_h gradually decreases to 0, and the strain rate sensitivity coefficient m expands.

3.3.5 Evolution of dislocations behavior

3.3.5.1 Mobile dislocation density

Under relaxation conditions, at time t the plastic strain rate $\dot{\epsilon_p}(t)$ and stress rate $\dot{\sigma}(t)$ have a relation (71):

$$\dot{\epsilon_p}(t) = -\dot{\sigma}(t)/E \tag{3.16}$$

where E is the elastic modulus for the specimen and machine, thus the Orowan's equation,

$$\dot{\epsilon_p} = \varphi b \rho_m v \tag{3.17}$$

can change to:

$$\dot{\sigma}(t) = -E\varphi b \rho_{m(t)} v \tag{3.18}$$

where φ denotes a geometric constant for the same dislocation structure in one experiment. By combining Eqs. 3.18 and 3.13, the mobile dislocation density at an arbitrary time $\rho_{m(t)}$ is:

$$\rho_{m(t)} = -\frac{\dot{\sigma}(t)}{\varphi b E v_0 \exp(\Delta\sigma_{eff} V_{eff}/MkT)} \tag{3.19}$$

and the mobile dislocation density at the onset of the stress relaxation curve $\rho_{m(0)}$ is:

$$\rho_{m(0)} = -\frac{\dot{\sigma}_{i1}}{\varphi b E v_0} \tag{3.20}$$

we define the quotient of $\rho_{m(t)}$ and $\rho_{m(0)}$ as the mobile dislocation density ratio:

$$\frac{\rho_{m(t)}}{\rho_{m(0)}} = \frac{\dot{\sigma}(t)}{\dot{\sigma}_{i1} \exp\left(V_{eff}\Delta\sigma(t)/MkT\right)} \tag{3.21}$$

in the case $\rho_{m(t)}$ is the mobile dislocation density at the beginning of the jth relaxation ($\rho_{m,ij}$), then $\Delta\sigma(t) = 0$. Thus Eq. 3.21 reduces to:

$$\frac{\rho_{m,ij}}{\rho_{m(0)}} = \frac{\dot{\sigma}_{ij}}{\dot{\sigma}_{i1}} (j = 1, 2, 3...) \tag{3.22}$$

the mobile dislocation density ratios at different cathodic current densities are plotted as a function of time in Fig. 3.9.

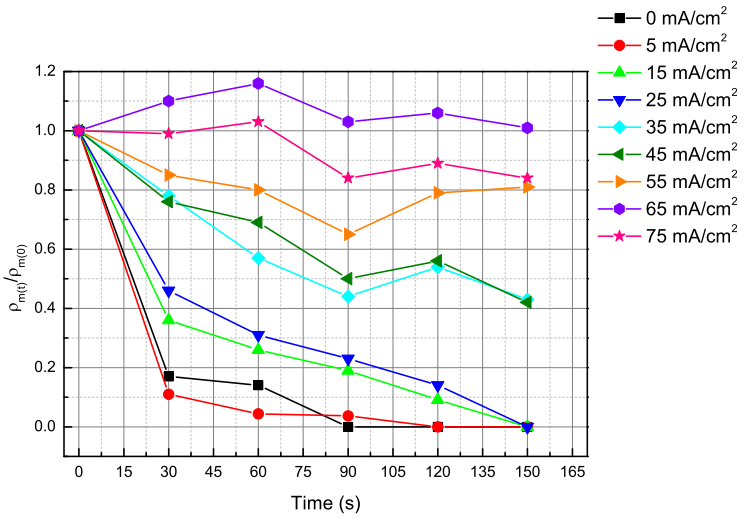

Figure 3.9: Mobile dislocation density ratios for different hydrogen flux rates versus duration of the applied flux.

As Fig. 3.9 shows, for low hydrogen concentrations (0 mA/cm^2 - 25 mA/cm^2) the mobile dislocation density ratios decrease gradually towards zero. Here it takes more relaxation cycles for the mobile dislocation to reach zero at higher hydrogen concentrations. For an example, the data of mobile dislocation density ratios at 65 mA/cm^2 arranged horizontally signifying that $\rho_{m(t)}$ is exhausted slowly as the hydrogen concentration increases. This indicates that the hydrogen shielding effect is sufficiently strong to weaken the co-existing solute-drag effect of blocking obstacles impeding the motion of dislocations moving with the hydrogen.

When hydrogen flux at 45 mA/cm^2, $\rho_{m(t)}/\ \rho_{m(0)}$ shows almost no exhaustion along time axis, which provides evidence that immovable dislocation may be re-activated by the continuation of injection of hydrogen into the lattice.

3.3.5.2 Total dislocations

The dislocation structures were observed by TEM at two beam conditions with the same reflection vector $g = [110]$ excited, and the typical results are shown in Fig. 3.10.

Dislocation structure of a stress relaxed hydrogen-free specimen(at a initial strain of 5%) in Fig. 3.10(a) and that of uniaxial deformed specimen in Fig. 3.4(a) show no differences in the microstructure and density. This suggests that there is only quasi-elastic deformation taking place in the reloading process of stress relaxation test, and that only the mobile dislocation density varied with time as stress decayed. There are tangling dislocations in Fig. 3.10(c) to Fig. 3.10(d), and the density of the tangling structures increase with the hydrogen concentration. The average dislocation density in the 75 mA/cm^2 sample (Fig. 3.10(d))is nearly one tenth that of ordinary 30% fractured specimen shown in Fig. 3.4(d), but fracture was induced for this hydrogen charged specimen at low total plastic strain, as observed in Fig. 3.6(b) above.

To confirm the tangled structure, a larger scale of dislocation distribution at different hydrogen concentration is shown in Fig. 3.11. The diffraction pattern and the reflection vector used for the TEM observation is marked in the left corner. All the foils were tilted to the same $\vec{g}$ vector, and bright field images were taken with $3\vec{g}[110]$ be strongly excited. The average thickness of observed area was calibrated by using g/3g dark field condition (88), and indicated below Fig. 3.11.

Compared with the upper left hydrogen-free dislocation structure in Fig. 3.11, with hydrogen there are some dislocation free zones (marked with arrow heads) surrounded by tangled dislocations. The area of the dislocation free zones, also the density of tangled dislocations, increase as C_H becomes higher. The tangling behaviour reveals that repulsive interactions between dislocations get weaker. The tangled dislocation structures also appear around the grain boundary as shown in GB area marked in the middle left of Fig. 3.11.

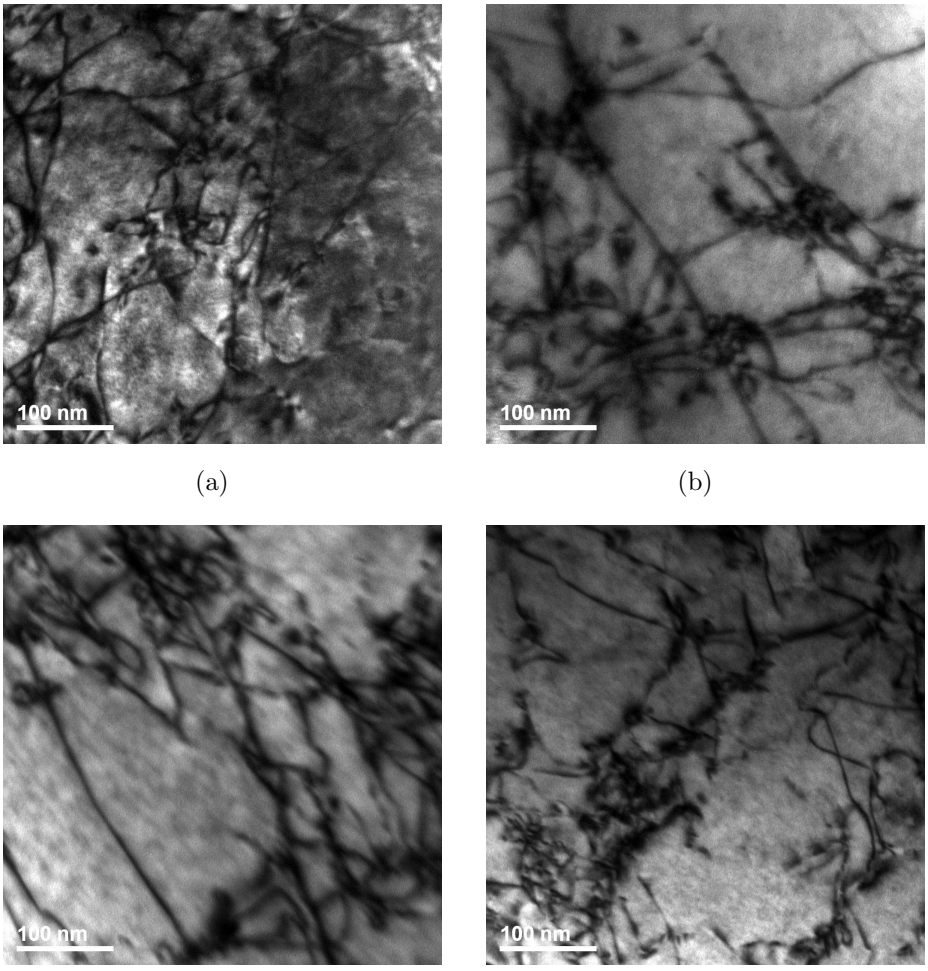

(a) (b)

(c) (d)

Figure 3.10: TEM images of dislocation structures. (a) after stress relaxation, without hydrogen charging; (b) after stress relaxation with 25 mA/cm^2 cathodic current density; (c) after stress relaxation with 45 mA/cm^2; (d) after stress relaxation with 75 mA/cm^2 (fractured).

3.3.6 Activation energy

With Eq. (3.6), the thermal activation energy is related to the dislocation velocity v and temperature (49):

$$\Delta G = -kT \ln\left(\frac{v}{\nu_D d}\right) = -kT \ln\left(\frac{\dot{\epsilon}_p}{\dot{\epsilon}_0}\right) \tag{3.23}$$

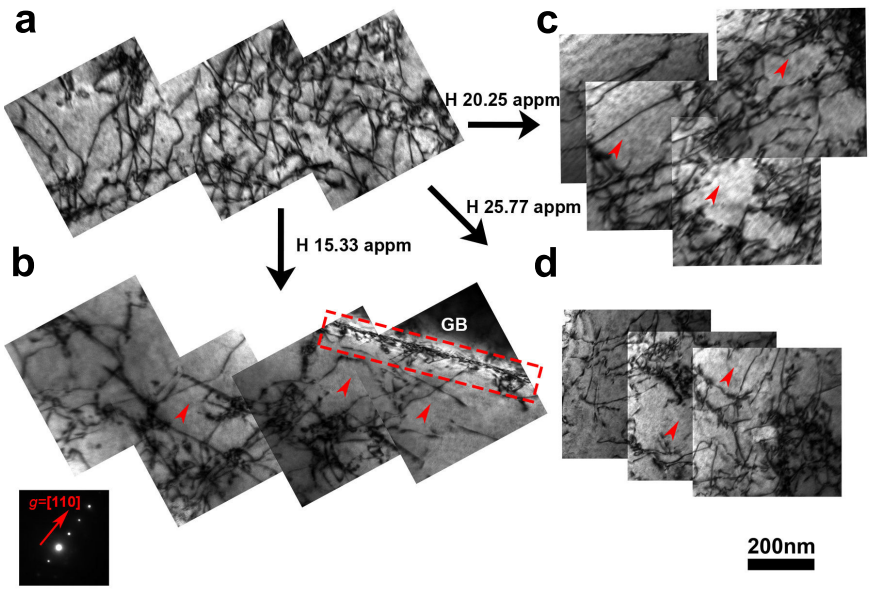

Figure 3.11: Dislocation structures after stress relaxations in air and at different hydrogen concentrations. (a) In air, thickness t= 270 nm; (b) C_H= 15.33 appm, t= 240 nm; (c) C_H= 20.25 appm, t= 270 nm; (d) C_H= 25.77 appm, t= 250 nm.

where $\nu_D \approx 10^{13}$ s^{-1} is the Debye frequency, d is distance over which dislocation moves after a successful activation event, and $\dot{\epsilon}_0$ is a characteristic strain rate. The zero stress thermal activation energy in Eq. 3.5 becomes:

$$\Delta F = -kT \ln(\frac{\dot{\epsilon}_p}{\dot{\epsilon}_0}) + \sigma_{eff} V_{eff}/M \tag{3.24}$$

Based on stress relaxation tests at different temperatures, ΔF and ΔG can be obtained from linear fitted intercept and slope of plotting $\sigma_{eff} V_{eff}$ versus T (83). However, by using D_0 in Table 3.1, the diffusion coefficient D of hydrogen atoms is 7.02×10^{-9} m^2s^{-1} at 293 K. With the large value, it is predicable that the hydrogen concentration changes considerably as the temperature varies. Therefore, conventional way for determining thermal activation energy is not proper to be directly applied to the hydrogen charged iron. In this study a new calculation method is developed to solve this problem.

Assuming that a additional Gibbs free energy $\delta\Delta G_H$ and a zero stress activation energy $\delta\Delta F_H$ are induced by hydrogen, Eq. 3.23 can be written as:

$$\Delta G + \delta\Delta G_H = -kT \ln(\frac{\dot{\epsilon}_p^H}{\dot{\epsilon}_0}) \tag{3.25}$$

where $\dot{\epsilon}_p^H$ is the plastic strain rate with hydrogen (not the constant strain rate in tensile test). Equation 3.24 with hydrogen becomes:

$$\Delta F + \delta\Delta F_H = -kT \ln(\frac{\dot{\epsilon}_p^H}{\dot{\epsilon}_0}) + \sigma_{eff}^H V_{eff}^H/M \tag{3.26}$$

Combing Eqs. 3.16, 3.23 and 3.25 gives the expression of $\delta\Delta G_H$:

$$\delta\Delta G_H = -kT \ln(\frac{\dot{\sigma}^H}{\dot{\sigma}}) \tag{3.27}$$

where $\dot{\sigma}^H$ is the stress rate with hydrogen. Considering Eqs. 3.16, 3.24 and Eq. 3.26 gives:

$$\delta\Delta F_H = -kT \ln(\frac{\dot{\sigma}^H}{\dot{\sigma}}) + (\sigma_{eff}^H V_{eff}^H - \sigma_{eff} V_{eff})/M \tag{3.28}$$

where V_{eff}^H and σ_{eff}^H are the effective activation volume and the effective stress measured from the hydrogen charged samples, respectively. All of the parameters

in the right hand side of Eq. 3.27 and Eq. 3.28 are already known from thermal activation analysis in the previous sections. The activation energy in the hydrogen charged samples can be obtained and the values are as shown in Fig. 3.12 shows the evolution of activation energy calculated by this method. From Fig. 3.12(a), the activation energy for the pure iron used in this study is 0.43 ± 0.12eV($\approx 0.06\mu b^3$), and Fig. 3.12(b) shows that $\delta\Delta G^H$ and $\delta\Delta F^H$ decreases as hydrogen concentration (cathodic current density) increases.The value of $\delta\Delta G^H$ become almost constant at high H concentration. Decrease of $\delta\Delta F^H$ shows no strong relationship with cathodic current densities.

3.4 Discussion

3.4.1 Dislocation density

The calculation of effective activation volume and the evaluation of mobile dislocation density obtained before rely upon the assumption that ρ_m remains constant (quasi-elastic loading) during the reloading process. As reported by Bonade (73), an unbalance between operating exhaustion and multiplication mechanisms of dislocation is likely to exist, which will result as an unreliable value of thermal activation parameters by former equations. In order to make sure that there is only change of mobile dislocation density during stress decay process, after repeat relaxation test the average total dislocation densities at different hydrogen flux intensities were measured by choosing at least 3 fields in each TEM foil, and are plotted with error bars in Fig. 3.13. There are less differences in the average total dislocation densities at different cathodic current densities. Nano-indentation and calculation work have found a multiplication of dislocations after long-time hydrogen charging (89). However, the repeated stress relaxation test is one kind of transient tensile tests operated in a short time range, this multiplication of dislocations can be disregarded, and the thermal activation analysis performed in this study is reliable.

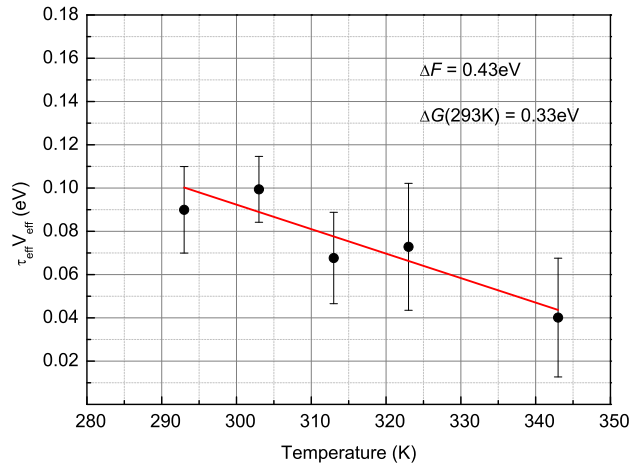

(a)

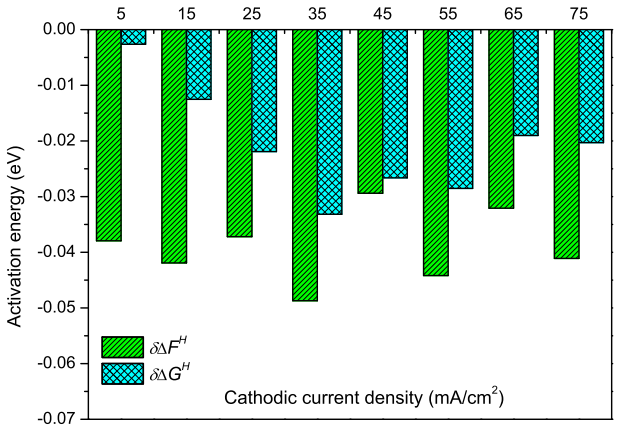

(b)

Figure 3.12: Hydrogen-induced activation energy. (a) Activation energy in hydrogen-free specimens measured by stress relaxation tests at different temperatures; (b) Hydrogen induced activation energies at different current densities.

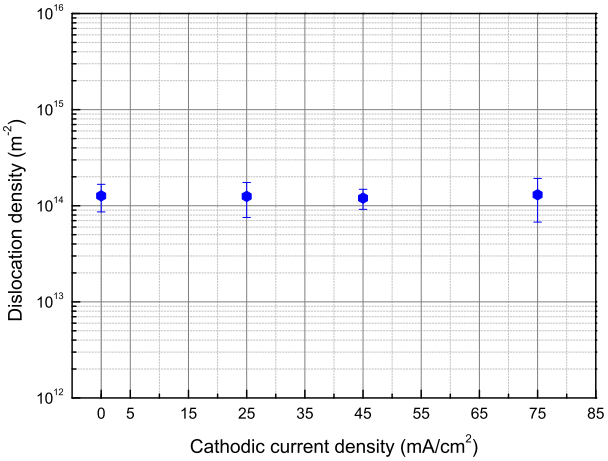

Figure 3.13: Average dislocation densities in samples after hydrogen charging with different cathodic current densities.

3.4.2 Activation volume

In pure iron, there are four main types of the short-range barriers impeding dislocation motion (90): (1) forest dislocations; (2) solute atoms; (3) Peierls-Nabarro barriers; (4) energy barriers due to the cross slip mechanism. These barriers are considered to be the main contributors to the stress hardening effect. Assuming that the distance from dilatation line formed by hydrogen atoms to a dislocation is r, according to Sofronis' analysis by finite element method (58, 91), hydrogen atmosphere induces a stress field which varies like r^{-2}, it affects dislocation and obstacle interaction in a short range and also decrease the interaction energy width between them. Such screening of short-range interaction indicates the decrease of the effective thermal activation volume. A similar conclusion for Ni has been made by Sirois et al. (54), we argue that hydrogen have the same behaviour in BCC iron.

Further, the calculations by Chateau et al. (41) implied that the hydrogen shielding effect is a diffusion assisted stress relaxation process, i.e. the decrease in the interaction stress field depends on the concentration and distribution of hydrogen. Hydrogen induced stress relaxation in local area increases linearly as the concentration changes $(C_H - C_0)$ (41): $\sigma_{kk}^H = -2EV_H(C_H - C_0)/[3(1-\nu)]$

where σ_{kk}^{H} is the hydrostatic stress provided by hydrogen atoms, V_H is hydrogen's partial molar volume, and ν is Poisson's ratio. The stress field of dislocation is relaxed by σ_{kk}^{H}, and the interactions with impurity atoms or other short-range barriers are supposed to be decreased linearly as a function of C_H.

However, the decreasing V_{eff} has a plateau at C_H from 5 mA/cm^2 to 25 mA/cm^2, and effective stress increases slowly as shown in Fig. 3.7(b). At these hydrogen concentrations, the yield stresses are in a stable level (see Table 3.2). In this plateau region, it is reasonable to consider that there are other factors which can neutralise the hydrogen effect, resulting in unchanged activation length and resolved stress for operating dislocations. The factors could be:

1. other solute atoms which can impede dislocation motion;
2. the solute-drag effect of hydrogen itself;
3. variation of dislocation structures induced by hydrogen.

The first possibility can be dismissed as the concentration and distribution of C, N and other solutes can hardly be changed during stress relaxation, they induce constant variation of activation volume. Kirchheim and co-workers (27, 28) pointed out that there are two aspects of the effect of hydrogen interstitial atoms: one that hydrogen enhances dislocation mobility by decreasing line energy; and the other that hydrogen exerts drag on dislocation, i.e., hydrogen can act both to slow down and speed up the dislocation motion. The effect of hydrogen solute-drag cannot be neglected. However, for the high diffusion ability of H atoms, at room temperature the second possibility could have less contribution.

We argue that the third factor is the main contributor to the variation of activation volume. As there is no multiplication of dislocations in stress relaxation process, the evolution of dislocation structure is mainly due to hydrogen effect. Once hydrogen is introduced, the short-range interaction is reduced, hence the effective activation volume decreases immediately and tangled dislocations are formed. As the repulsive interaction between dislocations is inversely proportional to the distance between dislocations, it becomes harder to reduce the interaction

range to a lower value once the tangled dislocations are formed. Hydrogen shielding effect on the tangled dislocations can be suppressed, that is the most possible reason for the unchanged yield stress and thermal activation length.

At concentrations higher than a threshold value, 17.98 appm in this study, as the hydrogen shielding effect increases, the dislocation free zone becomes larger and more tangled structure was found. This is a sign that, as hydrogen accumulating in the dislocation trapping sites, the impeding effect in tangled substructure can be neglected and hydrogen shielding effect mainly controls the dislocation motion.

3.4.3 Internal stress

During plastic deformation, the source of the internal stresses is the sum of the stresses resulting from the various arrangements of the dislocations and obstacles in the specimens.

As suggested by Kruml (86), the quality the internal stress calculated from Eq. 3.11 depends strongly on the type of crystal and stress relaxation condition. We have tried all the three methods developed by Kruml, and indicate that the internal stress of hydrogen-free iron does have 90% of the total stress, i.e. by the classical power law, 206 MPa.

By another method, the Taylor law: $\sigma_\mu = ME\alpha b\sqrt{\rho}$, in which α is a constant typically ranges 0.2 to 0.5, indicating the obstacle strength. As it is another model describing the dislocation motion, calibrating α is out of range of this work. However, using an typical α value of 0.23 for iron (92), internal stress is 147 MPa. The internal stress from our stress relaxation test is 204 MPa (see Appendix A), which may be overestimated. Indeed, under different external stresses, the internal stresses calculated by Kruml express the same tendency as the results from dip tests. Thus it is reasonable to compare the effective stress ratio in Fig. 3.7.

In FCC metal, the long-range elastic interaction between edge dislocation, especially edge partial of screw dislocation, shielded by dislocation is considered to be key factor due to hydrogen embrittlement. In BCC metal, however, there is no edge partial for screw dislocation. We suggest that in BCC iron, hydrogen

mainly influences the short-range interactions and changes the substructure of dislocations. Because of the formation of tangled structure, the internal stress reduces and softening can be observed.

The details of the internal stress development make it possible to postulate that the arrangements of dislocations and obstacles have been changed in hydrogen charged samples, leading to a tangling dislocation structures during deformation as observed by TEM above. The tangling structures gives proof that the shielding stress field caused by H in short range can make the repulsive stress field between dislocations become attractive, which has been proposed by the HELP theory based on calculation of the interaction of two edged dislocations (91). As shown in Fig. 3.14, by observation using scanning electron microscope (SEM), the fracture surface of specimen after relaxation test (total strain is around 5%) at 75 mA/cm^2 is found to be mainly intergranular fracture, with a small amounts of transgranular fracture. In Fig. 3.14(a), there are many secondary cracks (arrow) and grain boundary yawning (circle) on the fracture surface. Under a higher magnification in Fig. 3.14(b), micro-pores, and micro-cracks were observed. It implies that because of the high stressed regions formed by tangling dislocation structures, a segregation of H would lead to void formation at slip band or grain boundary, and thus the formation of micro-cracks would be encouraged too. The motion of dislocations could be blocked by those voids and micro-cracks. As the dislocations still have a high mobility caused by H shielding effect, suggested by Birnbaum (2), this would lead to coalescence of the leading dislocations at the head of a pile-up under external stress, and the formation of cracks will be encouraged.

3.4.4 Activation energy

The reduction in the thermal Gibbs energy is caused by the increase in effective stress discussed above. The decrease in the zero stress activation energy indicates that the energy barriers between dislocations and obstacles are reduced, which would be consistent with the result of the hydrogen charged Ni observed by Sirois and co-workers (54). Our study attempted to obtain a relation between H concentrations and the variations of activation energy, and it is found that at high H

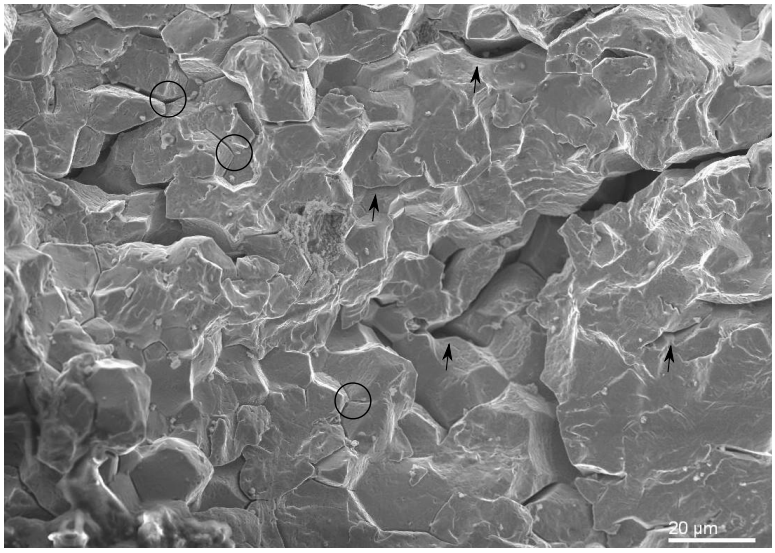

(a)

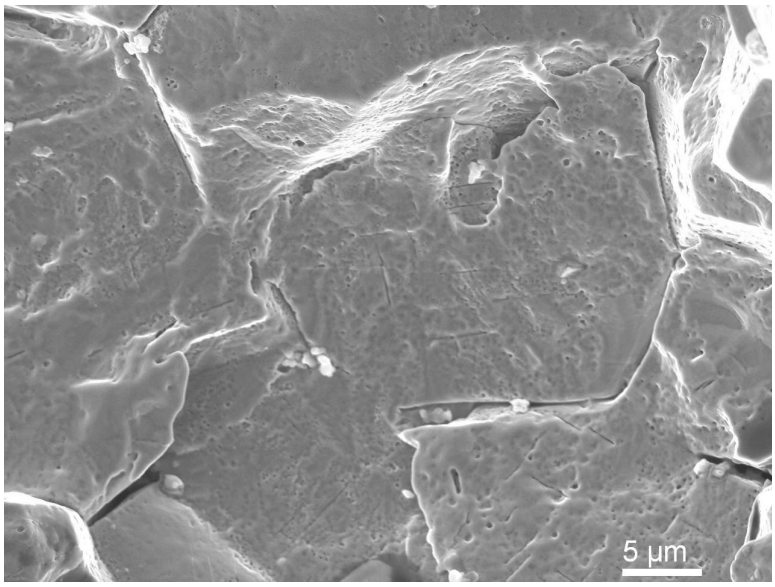

(b)

Figure 3.14: Fracture surface of stress relaxed specimen with cathodic current density of 75 mA/cm^2. (a) Intergranular fracture with secondary cracks and grain boundary yawning; (b) High magnification image showing micro-pores and cracks.

concentration degradation of activation energy is independent of cathodic current density, $\delta\Delta G^H$ is almost constant. Hydrogen decreases thermal activation energy consistent with a hydrogen related decrease in the strength of the dislocation obstacles which has been proposed by HELP theory.

In practical applications, aiming to improve the mechanical properties of components, some high strength compounds have large dislocation or precipitate densities which supply trapping sites for hydrogen. In such metals, the threshold value for the hydrogen shielding effect to completely dominate the deformation process can be easily reached (16). In the case of utilizing these materials in engineering structures, a result could be that even a low value of external stress will introduce a considerable effective stress with the resulting initiation of microcracks a likely result, due to the high density of tangling dislocations. This stresses need for careful investigation when using metal components with high densities of dislocations or precipitate exposed to hydrogen.

3.4.5 Dislocation velocity

The critical velocity for dislocation to break away from trapped hydrogen can be calculated using the concept of drift velocity of the dislocation atmosphere (54): $v_c = 4DkT/E_b r_c$, where r_c is the dislocation core radius, is about 3.46 Å for Fe. Thus hydrogen atoms can escape (or de-trap) from mobile dislocation with velocities higher than $v_c = 6.5$ m/s.

In the uniaxial tensile process, the dislocation velocity can be estimated from the Orowan equation. Using $\dot{\epsilon} = 10^{-4}$ s^{-1}, $\phi = 1$ and $\rho = 1.1 \times 10^{14}$ m^{-2}, the dislocation velocity is around 3.7 nm/s, which is much lower than v_c. During the stress relaxation process, as the total strain rate is zero, the dislocation velocity should be calculated from the plastic strain rate in Eq. 3.16. For the hydrogen free iron, from stress relaxation curve, at the onset of relaxation curve $\dot{\epsilon}_{p(0)} = 0.12 \times 10^{-4}$ s^{-1}, thus $v_{(0)} = 0.44$ nm/s. Note that dislocation velocity decreases as the plastic strain rate reduces in the relaxation cycle. With 25.77 appm hydrogen, $\dot{\epsilon}_{p(0)} = 0.40 \times 10^{-4}$ s^{-1}, $v_{H(0)} = 1.48$ nm/s. Combining Eqs. 3.17, 3.23 and 3.25, the dislocation velocity in the presence of H v_H indubitably yields:

$$\frac{v_H}{v} = \exp \frac{-\delta\Delta G}{kT} \tag{3.29}$$

using $\delta\Delta G$ in Fig. 3.12, v_H is about 3 times more than v, which matches the results from Orowan equation well.

3.5 Summary

Hydrogen in the matrix of iron increases the rate of stress relaxation. With samples strained to the same elongation, increases in hydrogen concentration increases the ratio of effective stress compared with the total external stress, and correspondingly reduces the ratio of internal stress. Softening caused by hydrogen could be observed as the internal stress and the yield stress clearly decreased beyond a critical value of hydrogen concentrations.

The results of the activation volume measurements and stress components analysis implied two distinguishable effects of hydrogen on the plastic deformation: a solute-drag effect (leading to strengthening of the metal) and a hydrogen shielding effect (leading to a HELP effect), working in a competitive relationship. The hardening term of the activation volume and dislocation velocity increases at a slow rate with small amounts of hydrogen. At higher H concentrations, there was a steep reduction in activation volume and a rise in dislocation velocity which demonstrates that the shielding effect dominates the deformation process.

Both of the thermal activation free energy and zero stress activation energy degrade at all hydrogen concentrations, and degradation of the activation energy is observed to be constant under relative high hydrogen concentrations (45 mA/cm^2 - 75 mA/cm^2). Considering the observed decrease in internal stress under hydrogen charging, it suggests that hydrogen reduces the energy barriers between gliding dislocations and the stress field of the pinning obstacles in b.c.c. iron, which is consistent with HELP theory.

By observations of the dislocation structure with TEM, the average dislocation density shows no differences under all the stress relaxation conditions investigated here. However, the mobile dislocation density has a lower rate of exhaustion than the hydrogen-free case. The interaction of dislocations and other localized stress fields arises as a result of the presence of hydrogen. A high density of tangling dislocations was observed at high H concentration and this indicate the repulsive

stress field between dislocations can become attractive by H shielding effect, which possibly leading to crack behavior even at a low total plastic strain.

Chapter 4

Apply the stress relaxation test to hydrogen charged iron-based alloy

4.1 Introduction

The purpose of this chapter is to evaluate the behavior of dislocations at different hydrogen concentration in pure iron, Fe-8Cr alloy and F82H steel (IEA heat). The precipitate density is increased in these alloys as adding alloy elements, the results from those metals would be helpful for understanding hydrogen-dislocation interaction in complicated structures. Dislocation activation volumes for dislocation overcoming energy barriers and variations of mobile dislocation density will be obtained from thermal activation analysis (60, 61, 62). Combining with microstructure observations using TEM, the results here would enable an understanding in details for the hydrogen effect on plastic behavior in Fe-Cr alloys.

4.2 Experimental methodology

Three kinds of material were used for fabricating samples, chemical compositions of the samples are shown in Table 4.1. The pure iron and Fe-8Cr model alloy were cold rolled to plates with a thickness around 0.3 mm. The F82H steel was

also made into 0.3 mm plates by slicing from received bulk. All the samples have the same dimensions as illustrated in Section 3.2 Fig. 3.1.

The Fe and Fe-8Cr plates were put into vacuum quartz tube (1×10^{-4} Pa) and annealed for 1 h at 873 K and 1073 K respectively. There was no heat treatment applied on the F82H steel. Electrochemical polishing with Acetic acid: Perchloric acid = 19:1 was taken to provide smooth surface and eliminate stress concentration on the surface, and the final thickness is around 0.25 mm. The tops of the tensile specimen were coated with polymer to protect them from cathodic charging.

Table 4.1: Main chemical compositions of tensile specimens (wt%).

Sample	Cr	W	Ta	V	C and N	etc.
Pure iron	-	-	-	-	0.04	Bal.
Fe-8Cr	8.00	-	-	-	0.04	Bal.
F82H	7.71	1.95	0.02	0.16	0.11	Bal.

The isothermal repeated stress relaxation tests were performed on an Instron 5564 universal test machine with an electrolytic cell for cathodic hydrogen charging at a constant temperature of 293 K. The electrolyte for the cathodic charging was 0.5 mol/l H_2SO_4 with 50 g/l Thiourea (promoter). The strain rate was set to $1 \times 10^{-4}s^{-1}$ which is slow enough for hydrogen to be transported by dislocation (72). The specimen was initially subjected to strain after yield point. Then the tensile cross-head was stopped and this state was maintained for 30 s and the strain is constant during relaxation. The decay of the stress was recorded as a function of time with an acquisition frequency of 0.3 s^{-1} for stress data. Subsequently the specimen was drawn to the stress same as the onset of the previous relaxation, and then the cross-head was stopped again. Every 30 s in this test is one cycle and which was repeated till no relaxation was recorded in the relaxation stage. While there is only elastic deformation between end of one cycle and onset of the next cycle, without undesired nucleation of total dislocations, the stress relaxation test gives an information of the mobile dislocation behavior (73). Continuous cathodic charging was applied in the whole relaxation progress

at cathodic current densities from 5 mA/cm^2 to 75 mA/cm^2 with an interval of 10 mA/cm^2. The surfaces of specimens were carefully examined to establish if there was surface blistering after the stress relaxation tests. To obtain the zero stress thermal activation energy, the stress relaxation tests of the hydrogen-free samples were also conducted at temperatures from 293 K to 373 K with strain rate of 1×10^{-4}s^{-1}.

The results of repeated stress relaxation tests were analyzed based on the method raised by Spätig (63), which has been illustrated in Chapter 3 too. In order to observe dislocation microstructures in hydrogen charged areas, preparation of hybrid foil was applied for TEM observations in this study (74). One mm diameter disks were punched out of the hydrogen charged areas and inserted into 3 mm 316F austenite stainless steel disks. The hybrid foils were thinned by a Struers Tenupol-5 electro-polisher, and subjected to TEM observations (JEM-2010) immediately after polishing in order to inhibit surface oxidation. Hydrogen-free specimens were also observed after stress relaxation test. The fracture surfaces for specimens after stress relaxation test, mainly Fe and F82H steel, were observed using scanning electron microscope (SEM, JSM-6500F).

4.3 Results

4.3.1 Hydrogen concentration

The hydrogen concentrations in different alloys are needed for further comparison of thermal activation parameters. Hydrogen concentrations in this Chapter are calculated using the method presented Section 3.3.1. The parameters for hydrogen concentration calculation is shown in Table 4.2. Same as in Section 3.3.1 the trapping sites per dislocation trap $\alpha^{(d)}$ and grain boundary trap $\alpha^{(g)}$ are set to 1 (81). Lattice sites per solvent atom is 6 for BCC metal. The dislocation density and precipitate density are determined by TEM observation which will be shown in next sections. Fig.4.1 shows calculation results for the hydrogen concentrations. Different from iron specimens, precipitates (mainly carbides) in Ferritic alloys have a higher binding energy which are able to trap more hydrogen than NILS and dislocation trap sites, therefore even at the lowest cathodic current

density (5 mA/cm^2) there are relatively high hydrogen concentrations in Fe-8Cr and F82H steel.

Table 4.2: Parameters for calculation hydrogen concentration

Parameter	Value
Lattice site density N_L (m^{-3}) (80)	8.46×10^{28}
Lattice parameter a (m) (80)	2.8865×10^{-10}
Trapping sites per trap $\alpha^{(d)}$,$\alpha^{(g)}$	1
Trapping sites per precipitate (6)	2.6×10^5
Lattice sites per solvent atom β	6
Dislocation density (m^{-2})	Iron: 1.2×10^{14}
	Fe8Cr: 0.7×10^{14}
	F82H: 1.5×10^{14}
Precipitate density (m^{-3})	Iron: 0
	Fe8Cr: 1.9×10^{19}
	F82H: 1×10^{21}
Permeation constant φ_0 (78)	3.70×10^{-6}
Diffusion constant D_0(m^{2}s^{-1}) (82)	1.1×10^{-7}
Trap binding energy (kJ/mol) (6)	$E_b^{(d)} = 30$
	$E_b^{(c)} = 85$
	$E_b^{(g)} = 50$

4.3.2 Stress relaxation curves

There are big differences between relaxation curves of hydrogen-free sample and hydrogen charged one. As shown in Fig. 4.2, charging hydrogen increases the possible number of relaxation cycles and also the relaxation rate for all specimens. After 160 s, only the relaxation tests for hydrogen charged samples can continue the repeated relaxation tests.

At 75 mA/cm^2 pure iron specimens fracture with total strain less than 6% (after 19 relaxation cycles), which indicates that the increase of hydrogen concentration arises the possibility of crack initiation. In F82H steel, hydrogen concentration is more than 1000 appm and the tensile specimen fractures just after the

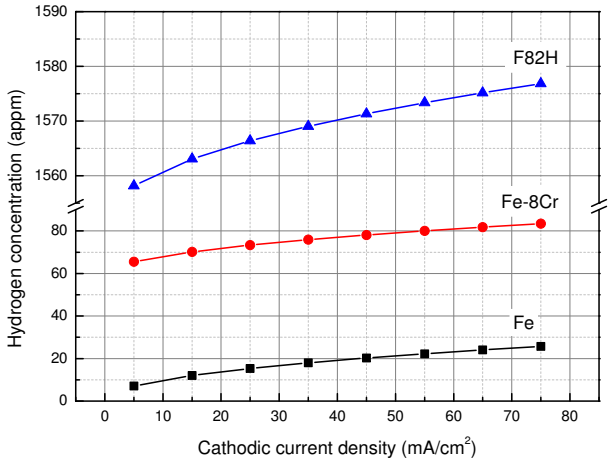

Figure 4.1: Hydrogen concentrations in three kinds of samples

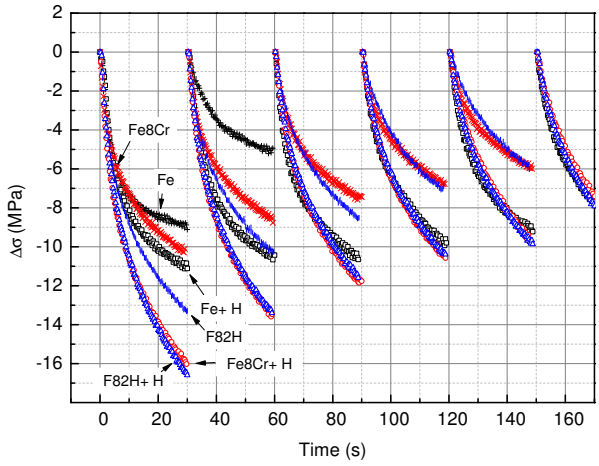

Figure 4.2: Stress relaxation curves of samples with and without hydrogen

yield point when cathodic current density is 45 mA/cm^2. However, such fracture was never observed in Fe-8Cr model alloy even at extra high current density of 125 mA/cm^2.

4.3.3 Activation volume and strain rate sensitivity

The effective activation volume (V_{eff}), strain hardening term of activation volume (V_h) and strain rate sensitivity (m) are illustrated in Fig. 4.3(a), Fig 4.3(b) and Fig. 4.3(c) respectively. The activation volumes of the three samples decrease as hydrogen concentration increases, the hardening term of an activation volume V_h gradually decreases to zero, and the strain rate sensitivity coefficient m expands. As described by HELP theory (58), the effect of hydrogen shielding is to decrease the range of interaction between dislocation and barrier, which is equivalent to reduce the effective activation volume as observed in the study here.

There is a plateau of activation volume at low hydrogen concentration (5 mA/cm^2-35 mA/cm^2) for pure iron in Fig. 4.3(a). Up to current densities more than 35 mA/cm^2, the activation volume decreases steeply to a value lower than 50 b^3 which signifies the interaction between glide and forest dislocations can be disregarded (90). However, the effective activation volumes of Fe-8Cr and F82H are decreased rapidly without a plateau like that. According to the numerical calculation work by Chateau et al. (41), hydrogen shielding effect is a diffusion assisted stress shielding process and the decrease of interaction stress field depends on hydrogen concentration and distribution. The degradation of activation volume as hydrogen concentration increases in this experiment is in good agreement with the calculation result.

V_h for pure iron increases at 5 mA/cm^2 - 35 mA/cm^2 in Fig. 4.3(b).This indicates that, at low hydrogen concentration, the hydrogen solute solution effect and tangled dislocation may reduce the influence of shielding effect on the dislocation-obstacle interaction. When cathodic current density increases up to 35 mA/cm^2, V_h decreases rapidly toward zero. As shown in Fig. 4.3(c) after a slow increasing period at the low current densities, the strain rate sensitivities increase steeply and the pure iron samples have the largest slope. Although the F82H samples have the most H concentration among three samples, value of m is much lower than the others.

As there are more precipitates pinning dislocation motion exist, large H concentration is required for decreasing the interaction of dislocation and precipitate. The results of internal stress ratio calculated by Eq. 3.11 (Section 3.3.4.1) are

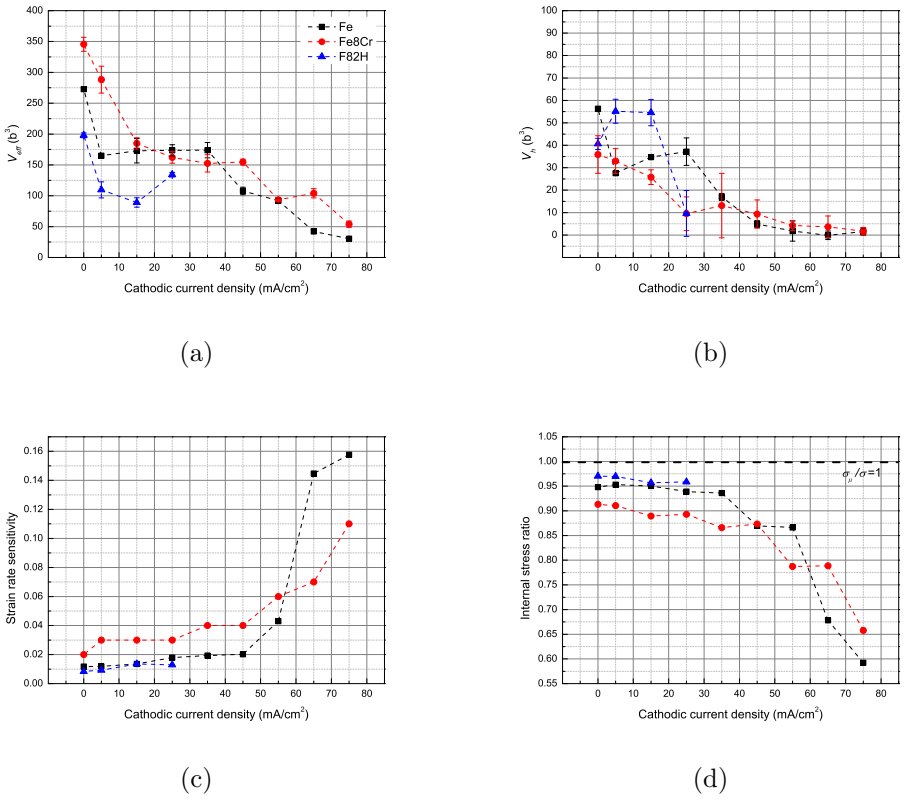

Figure 4.3: Variation of thermal activation parameters of three kinds of samples. (a) effective activation volume; (b) hardening partial of activation volume; (c) strain rate sensitivity; (d) thermal stress and athermal stress.

shown in Fig. 4.3(d). For all specimens, τ_μ/τ decreases as H concentration increases. At 5 mA/cm^2, the internal stress of Fe-8Cr decreases to the same level as Fe at 45 mA/cm^2, this might caused by the distribution of dislocations, solute atoms and precipitates in the matrix. At high H concentrations for both Fe-8Cr and F82H steel, the decreased internal stress ratios are smaller than pure iron. The precipitates in Fe-8Cr and F82H could have ability to inhibit the dislocation mobility even with hydrogen charged.

4.3.4 Evolution of mobile dislocations

The mobile dislocation density ratio of each kinds of sample have calculated out by the method used in Section 3.3.5.1 and shown in Fig. 4.4. Exhausting rate of

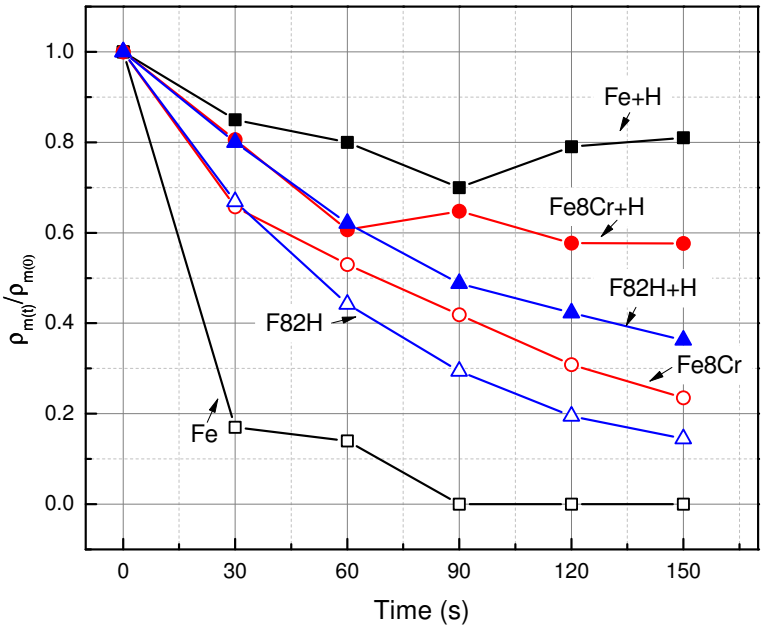

Figure 4.4: Evolution of mobile dislocation density ratio of three kinds of samples.

mobile dislocation density becomes lower as cathodic current density increases. In pure iron the mobile dislocation density ratios at 65 mA/cm^2 are almost constant as time changes, which signifies the mobility of dislocation is activated by hydrogen.

In Fe-8Cr and F82H steel samples, there are barriers (solute elements and precipitates) pinning the activated dislocations and the dislocations in those alloys have larger resistance compared with in iron. In this case, the hydrogen shielding effect has a competition relationship with the pinning effect of precipitates, and it can weaken the dislocation-precipitate interaction. But the degradation of the internal stress is not enough for releasing all dislocations from the pinning. For

the existing of such competition, the decrease of $\rho_{m(ij)}/\rho_{m(0)}$ is faster in the two alloys.

Such results make it possible to postulate that here the arrangements of dislocations and obstacles have been changed in hydrogen charged samples which will be illustrated by TEM in the next section. Dislocation structures have been observed by TEM with two beam conditions by an uniform reflection vector of $g = [110]$ excited for all samples. Typical results are shown in Fig. 4.5. From the microstructure shown in Fig. 4.5(a) and Fig. 4.5(b), tangled dislocation are found in hydrogen charged Fe. Similar structures are also found in Fe-8Cr model alloy as shown Fig. 4.5(c) and Fig. 4.5(d). For hydrogen-free sample in Fig. 4.5(c), dislocation segments can be pinned by precipitates, which is typical structure when dislocation overcomes precipitate. With hydrogen, tangled dislocations arrange in a narrow area between two precipitates, as shown in Fig. 4.5(d), which indicates the dislocation motion is impeded by the pinning of precipitates even at high H concentrations. As shown in Fig. 4.5(e) and Fig. 4.5(f) (calibrated in Table 4.2), the densities of dislocation and precipitate in F82H are much larger than in Fe-8Cr. Polygonized dislocation structures were found in the hydrogen charged specimen, and some of the dislocations have network structures.

4.4 Discussion

4.4.1 Average dislocation densities after stress relaxation test

The average dislocation densities in different cathodic current densities were calculated from several areas in the same TEM foil as plotted in Fig. 4.6. There is less difference of average dislocation densities in the same kind of samples. Nano-indentation and calculation works (89) have proved the multiplication of dislocations during hydrogen charging process . However, the transient tests using in this study are lasted for short time, thus even under a high hydrogen flux the nucleation of dislocations could be negligible in this study.

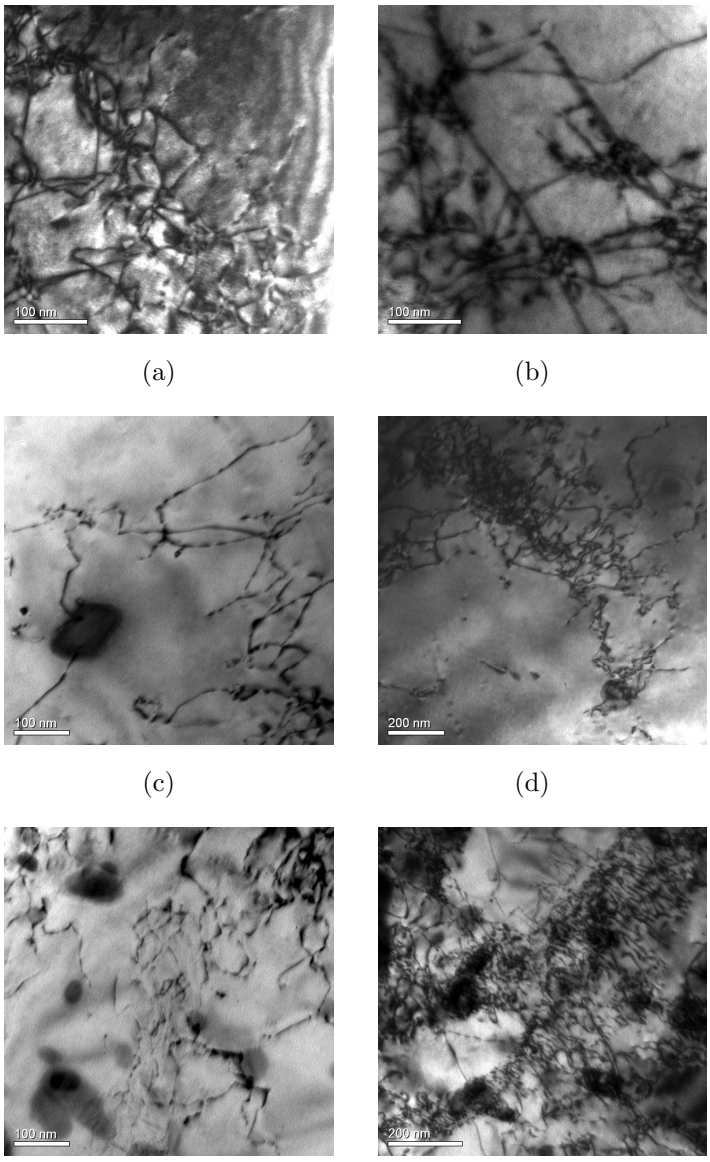

Figure 4.5: Evolution of dislocation structures in specimens at different conditions: (a) pure iron, without hydrogen; (b) pure iron, 25mA/cm^2; (c) Fe-8Cr, without hydrogen; (d) Fe-8Cr, 25mA/cm^2; (e) F82H, without hydrogen; (f) F82H, 15mA/cm^2.

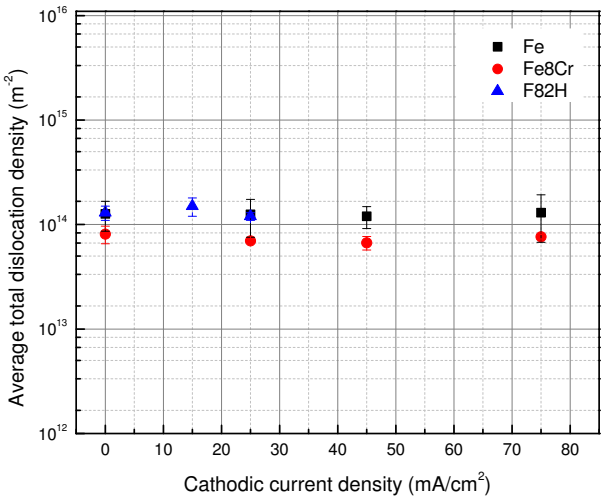

Figure 4.6: Evolution of average dislocation densities in the three kinds of samples.

4.4.2 Activation energy and the pinning effect of precipitates

Figure 4.7(a) shows the zero stress activation energy measured by the relaxation tests in different temperatures. Compared with pure iron, the activation energy of Fe-8Cr and F82H are increased because of the pinning effect of precipitates.

As shown in Fig. 4.7(b), the ΔG^H and ΔF^H of pure iron decrease as hydrogen concentration increases. The reduction of Gibbs energy is contributed by the increase of effective stress presented before. The decrease of zero stress activation energy indicates the energy barriers impeding dislocation motion are reduced, which is consistent with the result of hydrogen charged Ni reported by Sirois and co-workers (54).

In Fig. 4.7(c), the zero stress activation energy and Gibbs energy of Fe-8Cr have a little degradation (< 0.02 eV) at all cathodic current densities, and at high H concentration the value of activation energy is almost constant. As shown in Fig. 4.7(d), the hydrogen concentration in F82H steel is the largest among the three samples, and decreased activation energy is the most stable one. These

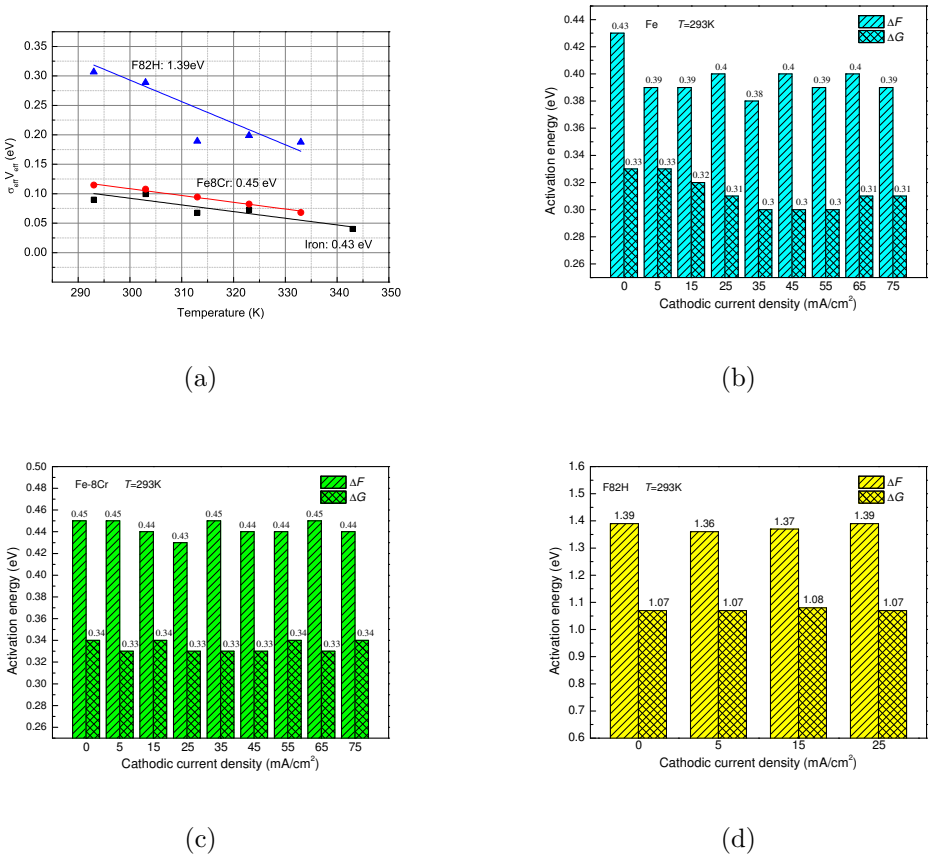

Figure 4.7: Activation energies in different kinds of samples: (a) zero stress activation energies in hydrogen-free samples; (b) the evolution of zero stress activation energies in Fe and Fe-8Cr; (c) the variation of Gibbs energies at 293K in Fe and Fe-8Cr; (d) the variation of thermal activation energy and Gibbs energy in F82H steel;

results provide that the precipitates and solute elements in Fe-based alloys have ability to decrease the hydrogen shielding effect. Although the dislocation have a high mobility as analyzed in Fig. 4.4, the barrier energy for dislocation to overcome is stable even at high hydrogen concentration.

The large scale segregation of dislocations in Fig. 4.5 would induce pile-ups behind precipitates and interfaces. As the dislocations still have high mobility, suggested by Birnbaum (2), this would lead to coalescence of the leading disloca-

tions at the head of a pile-up under external stress, and the formation of cracks will be encouraged. As illustrated in Fig. 4.3, the levels of activation volume V_{eff} and V_h are degraded by hydrogen signify that in F82H steel there are dislocations with high mobility which are impeded by large density of precipitates. The crack initiation for F82H in high hydrogen concentration could be enhanced and the fracture of specimens just after the yield point was observed in this experiment.

4.4.3 Contradictory effect of hydrogen

Kirchheim and co-workers (27, 28) pointed out that there are two aspects of the effect of hydrogen: one that hydrogen enhances dislocation mobility by decreasing line energy; and the other that hydrogen exerts drag effect on dislocation, i. e., hydrogen can act both to slow down and speed up dislocation motion.

In this part, the decreased activation volumes and increased strain rate sensitivities in high current densities of pure iron match with the HELP theory, while the increase of athermal stress at current density below 35 mA/cm^2 is different from the softening (decrease of flow stress) phenomenon observed in FCC metals(1, 2). We note that H induced solute-solution effect must be considered in the case small amount of H atoms are imposed. H atoms can be trapped by the stress field of dislocations, and the enhanced local plasticity increases linearly as the concentration changes $(C - C_0)$, which has been suggested by Chateau et. al (41): $\sigma^H_{kk} = -2MV_H(C - C_0)/[3(1 - \nu)]$.

As discussed in Section 3.4.2, hydrogen can shielding the dislocation motion, and also the hydrogen solute-solution effect and tangled dislocation can impede the shielding effect at low hydrogen concentrations by increasing the resistance in front of the moving direction of dislocations. The plateau shown in the activation volume curve in Fig. 4.3(a) (5 mA/cm^2 - 35 mA/cm^2) should due to competition of two effects. At high hydrogen concentrations, steep reduction of activation volume and rise of dislocation velocity are found, which demonstrates the relaxation of internal stress caused by the hydrogen shielding effect dominates the plastic deformation, and the H induced tangled-impeding and solute-solution effect could be screened by this effect too.

In the two alloys, because the hydrogen concentration is 10 times and 100 times more than in pure iron, and the hydrogen shielding effect has possibility to control the dislocation motion even at low cathodic current densities, the activation volume results of Fe-8Cr model alloy and F82H steel have no plateau as the pure iron. The competition of the two contradictory aspects of the hydrogen effect could be one of the key points for determining the mechanical properties of those BCC metals.

4.5 Summary

In iron, Fe-8Cr and F82H, hydrogen concentrations have been calculated by the Sievert's law as a function of cathodic current densities. Due to the existing of precipitates in Fe-8Cr model alloy and F82H steel, the hydrogen concentration is 10 times and 100 times more than in pure iron respectively.

Many common points was found from the result of stress relaxation tests in the three kinds of samples. The rate of stress relaxation in iron, Fe-8Cr and F82H are increased by hydrogen. Hydrogen charging decreases the internal stress ratio referring to the same stress for each sample. According to observations of dislocation structure in TEM, the total dislocation shows no difference in all stress relaxation conditions for the same kinds of samples. However, the mobile dislocation density has shown a low exhausting rate in specimens with hydrogen.

In pure iron, the hardening term of activation volume and dislocation velocity increase in a slow rate with small amount of hydrogen mainly caused by the hydrogen solute-solution effect. At high hydrogen concentrations, the hydrogen shielding effect increases a lot, and steep reduction of activation volume and rise of dislocation velocity are found, which demonstrates the shielding of internal stress field caused by the hydrogen mainly influences the plastic deformation. The mobile dislocation density rate data shows the dislocation mobility and dislocation interaction is enhanced by hydrogen, it results as high tangled density of dislocations, and even fracture with low dislocation density.

In Fe-8Cr and F82H, the hydrogen concentration is higher than in pure iron. The activation volume and internal stress decrease immediately at low cathodic current densities. However, the hydrogen enhanced dislocation motion is impeded

by the precipitates, thus the mobile dislocation exhausting rate in these two alloys is higher than in iron. In Fe-8Cr, it induces tangled dislocation between precipitates. In F82H, polygonized and network dislocation structures are found, and obvious embrittlement is found when cathodic current density up to 45 mA/cm^2.

The calculation of thermal activation free energy and zero stress activation energy shows that hydrogen reduces the energy barriers between gliding dislocations and the stress field of the pinning obstacles. The large scale segregation of dislocations would induce pile-ups behind precipitates and interfaces, as the dislocations still have high mobility caused by H shielding effect would lead to coalescence of the leading dislocations at the head of a pile-up under external stress, and the formation of cracks will be encouraged by this mechanism.

Chapter 5

Strain field of interstitial hydrogen atom in BCC iron and its effect on H-dislocation interaction

5.1 Introduction

In this part we introduce the analysis of electron structure of H-BCC iron system and the strain field of H atom based on density functional theory (DFT). For the first time, we combine the DFT calculation results with the classical calculation method developed by Cochardt et. al (93), which evaluates the interaction of interstitial atom with dislocation and has been proved to be in good agreement with experimental results for C interstitial atoms in BCC iron. The interaction of H with both edge type and screw type dislocations will be discussed. Hydrogen effects on dislocation motion will also be discussed based on repeated transients tests.

5.2 Simulation methodology

The first principle calculations are applied within the density functional theory. The Perdew-Burke-Ernzerhof (PBE) parametrization is used for the approximation of the exchanged-correlation (xc) function (94). Spin polarized calculation is performed with an initial magnetic moment of 2.20 for iron atoms. The grid-based projector-augmented wave (GPAW) method where the wave functions are expanded on a real space grid is also used (95). The grid spacing is set to 0.18 Å in all calculations. 0.1 eV of smearing is applied for the bulk calculations. The calculated lattice constant of Fe BCC bulk is 2.8369 Å which is a slight shrink (1%) with the respect to the experimental value (2.8665 Å), which can be attributed to the applied xc-functional (96).

Bulks of BCC iron with $(2 \times 2 \times 2)$ cell have been created (Fe_{16}) and vacancy defect has been created in some bulks by delete one iron atom in the cell (Fe_{15}). Periodic boundary conditions are considered for all the bulks. H atoms are inserted initially into tetrahedral positions of the cell, for the experimental evidence indicated such hydrogen occupancy for BCC Fe (97). $(4 \times 4 \times 4)$ k points of the Brillouin zone sampling which uses the Monkhorst-Pack scheme is carried out (98, 99). These conditions give bulk modulus (162 GPa) and magnetic moment (2.17 μ_B) for Fe_{16}, which are in good accordance with the results from experiment (165 ± 5 GPa, 2.22 μ_B) and other calculations (100). For comparison, strain field of H atom in FCC iron is also calibrated using a repeated $(2 \times 2 \times 2)$ cell (32 atoms) with $2 \times 2 \times 2$ k points. All calculations were made for 0 K. The variations of electron charges by adding hydrogen into the iron bulk is analyzed by a fast and robust algorithm implemented by Tang et. al (101) based on the Bader partitioning scheme (102). For confirmation the validity of the DFT result in large scale, molecular dynamics calculation using embedded atom method (EAM) was carried out on a $Fe_{106561}H_1$ cell. The EAM potential is based on the Fe potential from Ackland et al. (103) which fits well to bulk, vacancy, and surface data from DFT.

The elastic interaction between H and dislocations was studied following the classical method developed by Cochardt et al. (93). In BCC iron the symmetry of both the octahedral site and tetrahedral site are expected to produce a strain

field with local tetragonal symmetry. Since the exact atomic arrangement can be calculated using DFT method in this study, a strain tensor S_H of a unit cell containing one H atom can be obtained in a form of:

$$S_H = \begin{pmatrix} \epsilon_{11} & 0 & 0 \\ 0 & \epsilon_{22} & 0 \\ 0 & 0 & \epsilon_{33} \end{pmatrix} \tag{5.1}$$

If stress tensor $T_D = \sigma_{ij}^D$ of the dislocation field is expressed in the same coordinate system as the strain tensor $S_H = \epsilon_{ij}^H$, the elastic interaction energy U_{DH} can be written as:

$$U_{DH} = -(T_D, S_H)a^3 = -\Sigma_{ij}\sigma_{ij}^D\epsilon_{ij}^H a^3 \tag{5.2}$$

where a is the lattice constant. For the strain tensor which are not in the same coordinate system with σ_{ij}^D, crystallographic relations is used for transforming the interstitial strain tensor into the same coordinate as the stress field of dislocations, for details can refer to the calculations focused on carbon atoms (93). Consider an Fe crystal with a screw dislocation in the [111]-direction, using a similar model as Cochardt's (93), the interaction energy of this screw dislocation and an interstitial H atom is found to be:

$$U_{DH}^S = \frac{\sqrt{2}bGa^3\cos\varphi}{3\pi r}(\epsilon_{11} - \epsilon_{22}) \tag{5.3}$$

in which φ is angle between $[2\overline{11}]$-axis and the normal direction of plane containing the screw dislocation and zero point of the coordinate, a is lattice constant, b is Burgers vector (2.48 nm). U_{DH}^S decreases inversely with r and is zero for a pure dilation ($\epsilon_{11} = \epsilon_{22}$).

The interaction energy of hydrogen atom and an edge dislocation laying in $< 211 >$ with b in the direction $< \overline{1}11 >$ can be obtained as:

$$\begin{aligned} U_{DH}^E = \frac{Gba^3}{2\pi r(1-\nu)}\{&\frac{1}{3}\sin\psi(1+\nu+2\cos^2\psi)(\epsilon_{11}+\epsilon_{22}+\epsilon_{33}) \\ &-\frac{1}{2}\sin\psi\cos 2\psi(\epsilon_{22}+\epsilon_{33}) \\ &-\frac{\sqrt{6}}{3}\cos\psi\cos 2\psi(\epsilon_{33}-\epsilon_{22})+\nu\sin\psi\epsilon_{11}\} \end{aligned} \tag{5.4}$$

where angle ψ is the angle between $< \overline{1}11 >$ and the radius vector from the dislocation to the considered elementary cell, and ν is Poisson's ratio.

5.3 Results and discussion

5.3.1 Electronic structure

The total density of states (DOS) at Fermi level for Fe_{16} is 15.16 states/Ry atom (theoretical value: 15.37 (104)), and for Fe_{15} is 15.64 states/Ry atom. The DOS at the Fermi level in the H-containing BCC iron is found to be reduced. This is different from FCC iron with H occupied at octahedral site, in which the DOS increases as reported by Gavriljuk's group (48).

As shown in Fig. 5.1, there is a strong peak for projected DOS (PDOS) appearing at -8.62 eV ($E - E_F$) for iron atom which is the nearest neighbor (Fe_{nn}) to interstitial H. The -8.62 eV peaks in all Fe orbitals correspond to the H-1s states which indicate strong bonding interaction between Fe and H.

The total charge of H, individual iron atom (with no neighbor H atoms, Fe_{in}) and the Fe_{nn} atom resulted from the Bader analysis are shown in Table 5.1. The total charge of Fe_{in} remains the same as in the hydrogen free bulk. Charge variation of $+0.4024e^-$ occurs on the H atom, and $-0.0724e^-$ occurs on the nearest neighbor Fe atom. It has been reported that charge transference of $-0.31e^-$ appears from Fe_{nn} atom near an edge dislocation of BCC iron (105).

With a grid refinement number of 4, the distributions of all-electron density (in a unit of $Bohr^{-3}$) for Fe_{nn}, H and vacancy are calculated and characterized by plotting contour surfaces with different isovalues in Fig. 5.2. Fe_{nn} atom expresses bonding behavior with H atom in Fig. 5.2a, and the distance of Fe_{nn}-H bond is less than the Fe_{nn}-Fe_{in} bond as shown in Table 5.1. Hydrogen atoms increase the electron charges in tetrahedral sites of the bulk (Fig. 5.2b) and also in the vacancy (Fig. 5.2c and Fig. 5.2d).

Although the H-induced variations in DOS at Fermi level for BCC iron are in opposite tendency with FCC iron, the result that hydrogen decreases electron density of Fe atom is in accordance with the FCC iron system (48). Unlike the carbon atom enhances local electron density of iron atoms and assists the covalent character of inter-atomic bonds (106), hydrogen increases the concentration of electrons in lattice and promotes the metallic character of atom interactions.

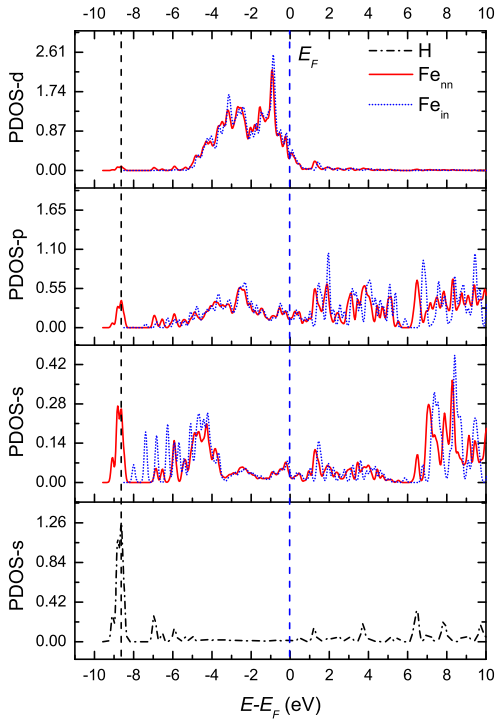

Figure 5.1: Projected density of states over iron and H atoms.

Compared with covalent bonds, the metallic character could increase the local plasticity of metal and the mobility of dislocations.

5.3.2 Elastic interaction of H and dislocations

After relaxation via DFT calculations, H atoms are stable in the tetrahedral sites of the lattice. The atomic forces in three axis for H atom are 0.000 eV/Å and for Fe atoms are lower than 0.008 eV/Å. The strain field of an interstitial atom is

Table 5.1: Variation of charges and bonding behavior in BCC iron containing H.

Atom	Bader charge	Bond	Distance (Å)
Fe_{in}	25.9437	Fe_{in}-Fe_{nn}	2.392
Fe_{nn}	25.8713	Fe_{nn}-H	1.681
H	1.4024		

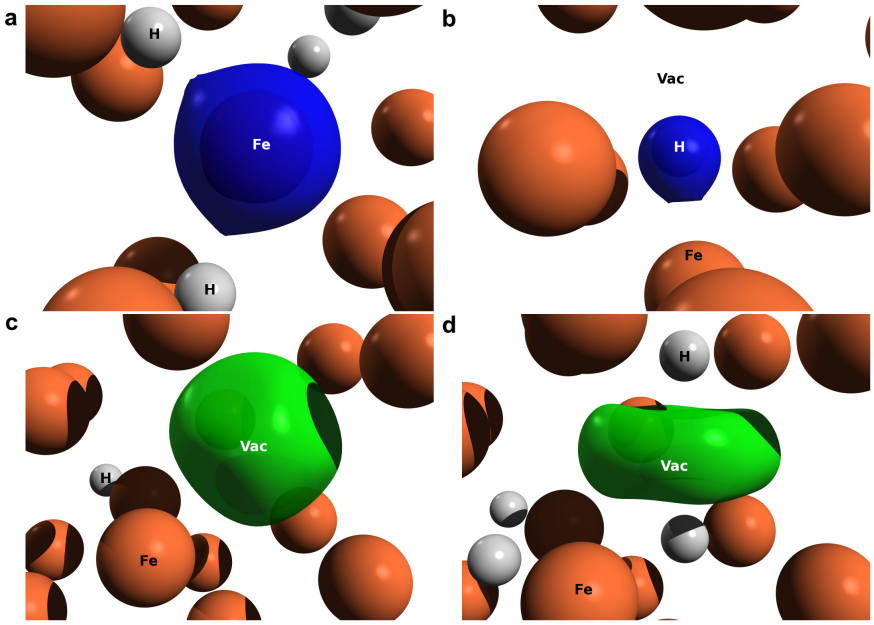

Figure 5.2: Contour surfaces of electron density in Fe-H system by Bader analysis. (a) Fe_{nn} atom, contour surface at isovalue of 0.08 Bohr^{-3}. (b) Interstitial H atom at tetrahedral site of iron lattice, contour surface with isovalue of 0.08 Bohr^{-3}. (c) Hydrogen-free vacancy, contour surface with isovalue of 0.02 Bohr^{-3}. (d) Vacancy binding with H atom, contour surface with isovalue of 0.02 Bohr^{-3}.

calculated from the displacement of Fe_{nn} atoms after relaxation, $\epsilon_{ii} = (L_i - a)/a$, where L_i is length in the i axis of one cell after introducing H. By our DFT method, the strain tensor of C in octahedral sites of iron is calculated to be $\{\epsilon_{11}, \epsilon_{22}, \epsilon_{33}\} = \{0.21, -0.018, -0.018\}$, which is comparable to experiment value $\{0.38, -0.026, -0.026\}$ used in Cochardt's calculation (93). The strain field of one H atom in $Fe_{16}H_1$ is calculated to be $\{0.014, 0.041, 0.041\}$. The MD calculation in large scale results as a strain tensor of $\{0.015, 0.059, 0.059\}$, which shows good agreement with the DFT calculation. The three components were considered to be identically equaled in none-DFT calculations for supporting HELP theory (2, 41). However, using the same parameter as BCC calculation in a FCC (2 2 2) cell ($Fe_{16}H_1$) the strain tensor is calculated to be $\{0.127, 0.127, 0.127\}$ which is isotropic.

Following the Cochardt's model, the interaction energy of hydrogen atoms at position $r = b$ and an edge dislocation laying in $< 211 >$ with b in the direction $< \bar{1}11 >$ is calculated. Since H atom may cause the less dilatation of 0.014 along axes 1, 2 or 3, there are three sets of constant in Eq. (5.2). The interaction energies are plotted in Fig. 5.3a, where angle ψ is the angle between $< \bar{1}11 >$ and the radius vector from the dislocation to the considered elementary cell. It is shown that the lowest interaction energy locates at $\psi = 270$ degrees, and thus H atoms prefer to stay below the extra half plane of edge dislocations. The lowest energy comes from H atom with strain field of $\{0.014, 0.041, 0.041\}$, and the minimum $U^E_{DH} = -0.24$ eV.

The interaction for a screw dislocation in [111]-direction and H atoms at position $r = b$ is calculated and shown in Fig. 5.3b, where φ is angle between $[2\overline{11}]$-axis and the normal direction of plane containing **r** and **b**. Because of the trigonal symmetry of $< 111 >$ axis, there is a phase difference of ± 120 degrees for H atom in different positions. The angular dependence of U^S_{DH} characterized in Fig.5.3b indicates that there are three equivalent positions of lowest energy at $\varphi = 0, 120$ and 240 degrees with minimum $U^S_{DH} = -0.051$ eV.

During plastic deformation, the cross slip of perfect screw dislocation is more important than the behavior of edge dislocations, for the unrecoverable jogs it forms. As the group of Chateau pointed out (41), hydrogen atom influence the cross slip of perfect screw dislocation in FCC mainly by screening interaction

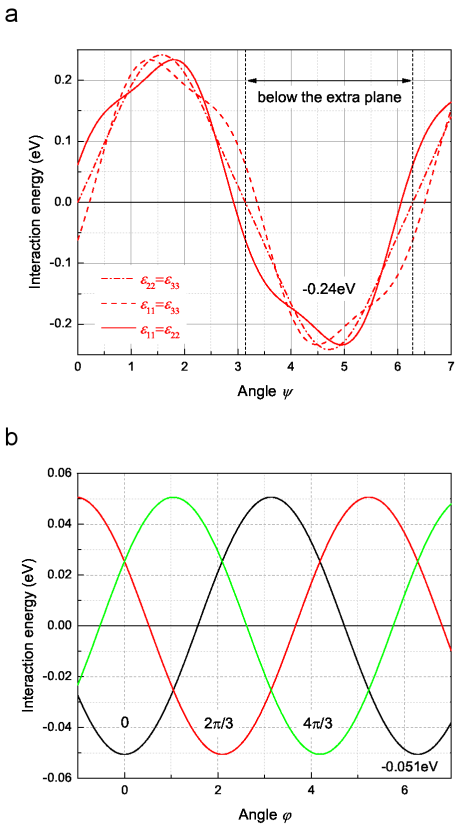

Figure 5.3: Elastic interactions of Hydrogen and different kinds of dislocation. (a) Edge dislocation laying in$< 211 >$, b=$< \bar{1}11 >$. (b) Screw dislocation in [111]-direction.

of two edge partials, but this theory can not be applied to BCC metal directly due to there is no partial dislocations. By comparing the accumulation of H around a screw and an edge dislocation, one can find that the segregation of H atom takes place only below the glide plane of an edge dislocation but all around a screw dislocation, roughly the screw can bind twice as many H atoms as an edge dislocation. Although the elastic interaction energy away from the screw dislocation core is much less than the case of edge dislocation, increase of local H concentration could magnify the H-screw interactions and influence the mechanical property of BCC metals.

5.4 Summary

In summary, H in BCC iron can increase the electron densities at tetrahedral sites and vacancy, and that the hydrogen-enhanced metallic character of inter-atomic bonds can increase the mobility of dislocations and contribute to the HELP theory. Two components of strain tensor for H interstitial atom are calculated to be unequal, which is expected to cause elastic interaction of H with screw dislocations, as it does with edge dislocations. For the angular dependence of H-edge dislocations interaction, H atoms prefer to stay under extra atomic plane, while for screw dislocation there are more positions for the lowest interaction energy and high local H concentration is possible. The repeated transients tests for H-charged α-iron indicate that significant hydrogen enhanced plasticity can be observed with relative high H concentrations, and in those cases, the H-screw interaction should be considered, and it is possible to lead for a new understanding of hydrogen embrittlement in BCC iron.

The problem of H-dislocation interactions is much complicated. Here we focused on emphasizing for the influence of unequal strain field, and in the future work, further calculations for the details of hydrogen effect on screw dislocation motion will be reported.

Chapter 6

Hydrogen-induced change of core structures of edge and screw dislocations in body-centered cubic iron

6.1 Introduction

Much attention has been paid on the hydrogen and dislocation interactions, which is of importance for understanding the internal mechanism of hydrogen embrittlement problem. However, if we review the past researches, most of the H-dislocation interaction models actually focus on edge dislocation (91) or edge partials of screw dislocation (41). For instance, in HELP mechanism, the scresw-H interaction is ruled out due to a assumption of isotropic strain field for H atoms. This assumption have no problem with FCC metals, as we argued in Chapter 5 (107), due to the anisotropic strain field of H atoms in BCC metals, a short-range screw-H interaction is possible. Many DFT and MD calculations have reported the trapping of hydrogen on the screw core and changes in kink pair nucleation (108, 109, 110), but there is a paucity of studies on the hydrogen effect on evolution of dislocation core structure. The screw-H interaction in BCC iron needs to be investigated by simulation and experimental works.

In this part, the analysis of dislocation core structures and the Peierls barriers at different hydrogen concentrations will be introduced using a DFT based embedded atom method (EAM) potential. The edge-H and screw-H interaction will be discussed based on the simulation results.

6.2 Simulation methodology

The MD simulations are performed using the LAMMPS code (111), with a DFT based Fe-H EAM potential reported by Ramasubramaniam et al (108). Simulations are carried out by integrating Newton′s equations of motion for all atoms using a time step of 1 fs. The optimization of structure was performed by the conjugate gradient (CG) algorithm, with a force tolerance of 0.001 eV/Å. The resulted lattice parameter a for iron is 2.8553 Å.

Here we consider an isolated edge dislocation with Burgers vector 1/2[111], slip plane normal $[\bar{1}10]$, and line direction $[\bar{1}\bar{1}2]$. Using the method of Cai (112), we first create a perfect crystal satisfying the periodic boundary conditions (PBC) with dimensions 20[111], 20$[\bar{1}10]$, 30$[\bar{1}\bar{1}2]$ along the X, Y, Z axes. Then the 1/4 of the atomic layers normal to the $[\bar{1}10]$ direction are removed to create two free surfaces, and edge dislocation was introduced as dipole. As one of the two dislocations in the dipole is intentionally introduced into the vacuum region, only one dislocation remains after minimization. The edge dislocation system contains 106560 atoms (97.64 nm×80.75 nm×209.67 nm). As illustrated in Fig. 6.1a, the dislocation was detected by using common neighbour analysis (113). By the similar method, a isolated $1/2\langle 111\rangle\{\bar{1}10\}$ screw dislocation was created, as shown in Fig. 6.1b. The screw dislocation system contains 108000 atoms (98.87 nm×80.75 nm×209.67 nm). The glide planes for the two dislocations are located at the half length of Y axis, thus the image forces produced by two free surface are negligible (114).

The Peierls barriers were investigated using the nudged elastic band (NEB) method, which enabled us to search the energy saddle-point and minimum energy path (MEP) between initial and final states. The initial configuration for NEB calculation was obtained by NPT ensemble with a Nose-Hoover thermostat, and the system was thermally equilibrated at 0.01 K for 50 ps. Then a NVT ensemble

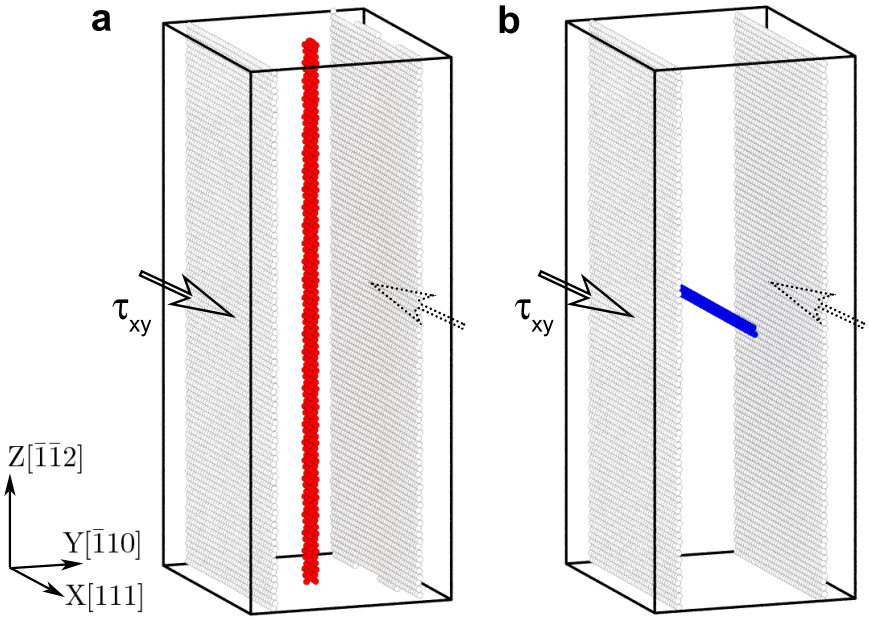

Figure 6.1: Schematic geometric of two types of dislocation used in simulation: (a) $1/2\langle 111\rangle\{\bar{1}10\}$ edge dislocation; (b) $1/2\langle 111\rangle\{\bar{1}10\}$ screw dislocation.

was used instead and external stress τ_{xy} was applied on the surface atoms with a constant strain rate of 1.5×10^7 s^{-1}, as shown in Fig. 6.1. By the Peach-Koehler forces introduced by τ_{xy}, edge and screw dislocations move $1b$ forward along +X and -Z direction respectively, and these are the final configurations for NEB calculations. The dislocation displacement can be controlled by the average difference in displacement per atom between two $\{\bar{1}10\}$ surface, Δu. According to Orowan′ law, when $\Delta u = b$, the dislocation crosses the entire cell. Thus, for a displacement of $1b$, Δu increases by b/N_P with N_P denotes the number of Peierls valleys along the moving direction. Peierls energy and evolution of dislocation core structure were analysed at different hydrogen concentrations. Hydrogen atoms were initially putted near the dislocation core ($1b$ distance), and their positions were optimised by the CG method. We will use H atom per dislocation length (nm^{-1}) to measure the hydrogen concentration.

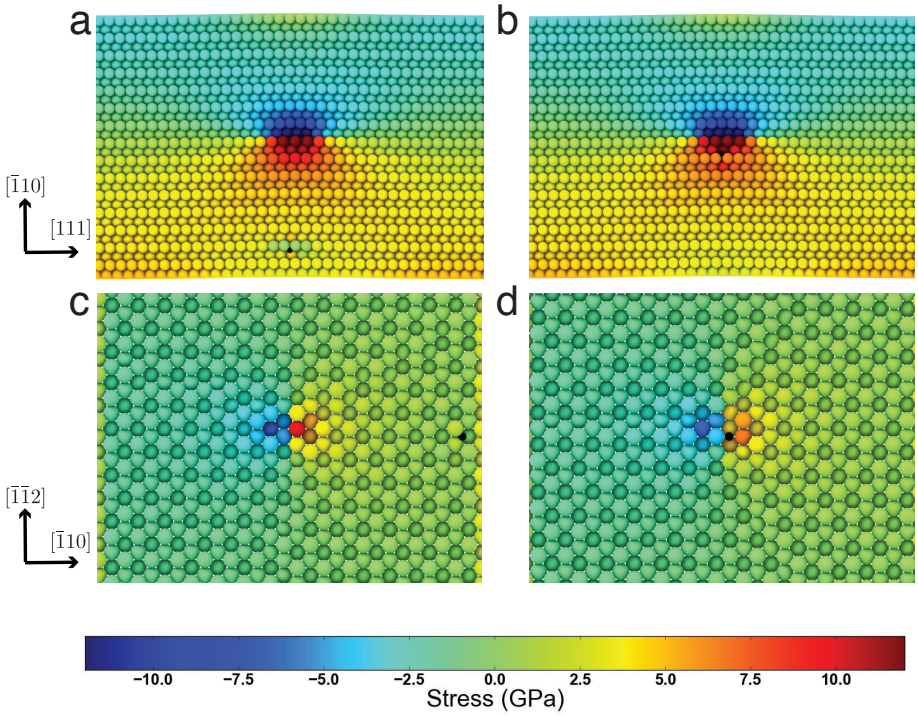

Figure 6.2: Changes in self-stress field of dislocations by putting hydrogen atoms (in black) in different positions (a) σ_{xx} of edge dislocation, distance of H from dislocation: 26Å; (b) σ_{xx} of edge dislocation, distance of H from dislocation: 2Å; (c) σ_{xz} of screw dislocation, distance of H from dislocation: 28Å; (d) σ_{xz} of screw dislocation, distance of H from dislocation: 2Å

6.3 Results

6.3.1 Trap energy of H atom

The stress field of edge dislocation, and screw dislocation can be obtained directly from the MD simulation, as shown in Fig. 6.2. Independent of distance from dislocations, hydrogen atoms weak the stress field of edge dislocation beneath the half atomic plane in Figs. 6.2(a) and (b). In case of screw dislocations in Figs. 6.2(c) and (d), different from edge dislocation, hydrogen decreases the self-stress field in short-range (Fig. 6.2(d)).

Following calculation in Chapter 5, the trap energy distribution around edge

and screw dislocation have angular dependency. In MD simulation, it is more direct to get the hydrogen trapping energy at different positions. The trap energy of hydrogen atom on dislocations can be calculated following the equation (108):

$$E_{trap} = [E(Fe_0^N, H^n) - E(Fe_0^N)] - [E(Fe_d^N, H^n) - E_d^N] \tag{6.1}$$

where N and n in the right side denotes crystals containing N Fe atom and n H atom, $E(Fe_0^N)$ and $E(Fe_0^N, H^n)$ are potential energies of a perfect crystal without and with hydrogen, and $E(Fe_d^N)$ and $E(Fe_d^N, H^n)$ are potential energies of a dislocation system without and with hydrogen. Note that trap energy here is different from the interaction energy in Chapter 5, always we have "trap energy = - interaction energy" (interaction energy here is actually the segregation energy of hydrogen).

The trap energy of hydrogen at $[\bar{1}10]$ direction with different distances from dislocation core in Fig. 6.2 is calculated and plotted in Fig. 6.3, which is like a "line scan" of H trap energy around dislocations. In Fig. 6.3(a) the trap energy is find to have a high value at negative distance from core position, this indicates that hydrogen is much more stable when it stays under the extra plane of edge dislocation. Such result matches the DFT calculation in Chapter 5 well. The screw dislocation have a wavy trap energy and the energy decreases fast as increasing the distance. This is because that hydrogen are trapped in different positions in different atomic layers ($\{\bar{1}10\}$ planes). The trap energy of hydrogen at edge and screw dislocation core is calculated to be 0.40 eV (ref. value 0.46 eV (108)) and 0.26 eV (ref. value 0.29 eV (108)), respectively. At $1b$ distance from dislocation core the energies are 0.25 eV and 0.08 eV, which are comparable to DFT+Cochardt method in Chapter 5.

The interaction energy map around a screw dislocation is calculated to verify the results in Fig. 5.3(b). To do this, hydrogen atoms were given initial coordinates as ($r\sin\varphi$, $r\cos\varphi$) in $\{111\}$ plane, where r is the radius from dislocation core, and φ has the same meaning as in Eq. 5.3, ranges from 0° to 360° with a internal of 15°. The result of this mapping is shown in Fig. 6.4. The blue area indicates the stable positions for hydrogen atoms. The interaction energy have the same angular dependency as presented in DFT calculation, 0°, 120° and

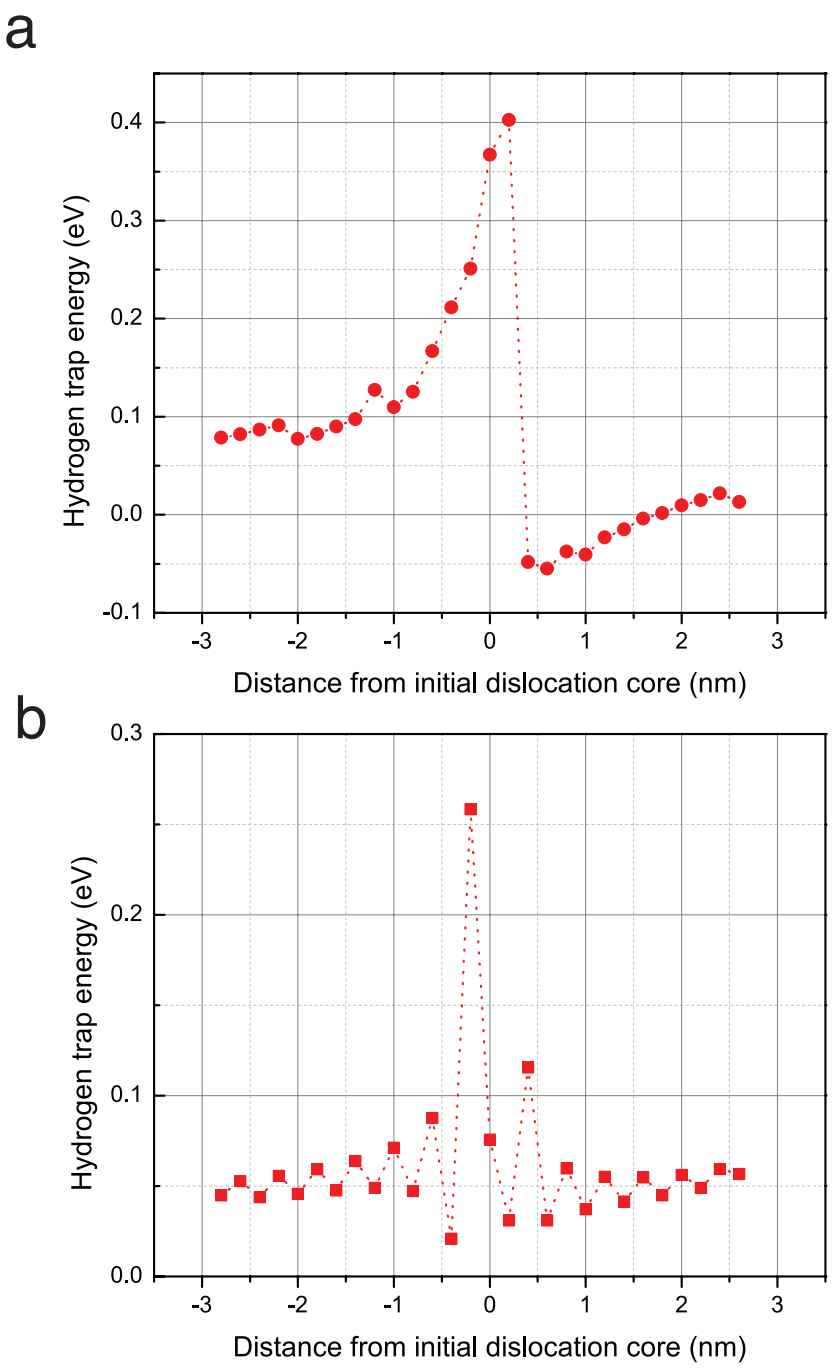

Figure 6.3: Trap energy of hydrogen at several distances from dislocation core: (a) edge dislocation, hydrogen has a high trap energy (stable) under the extra atomic plane; (b) screw dislocation, angular dependence.

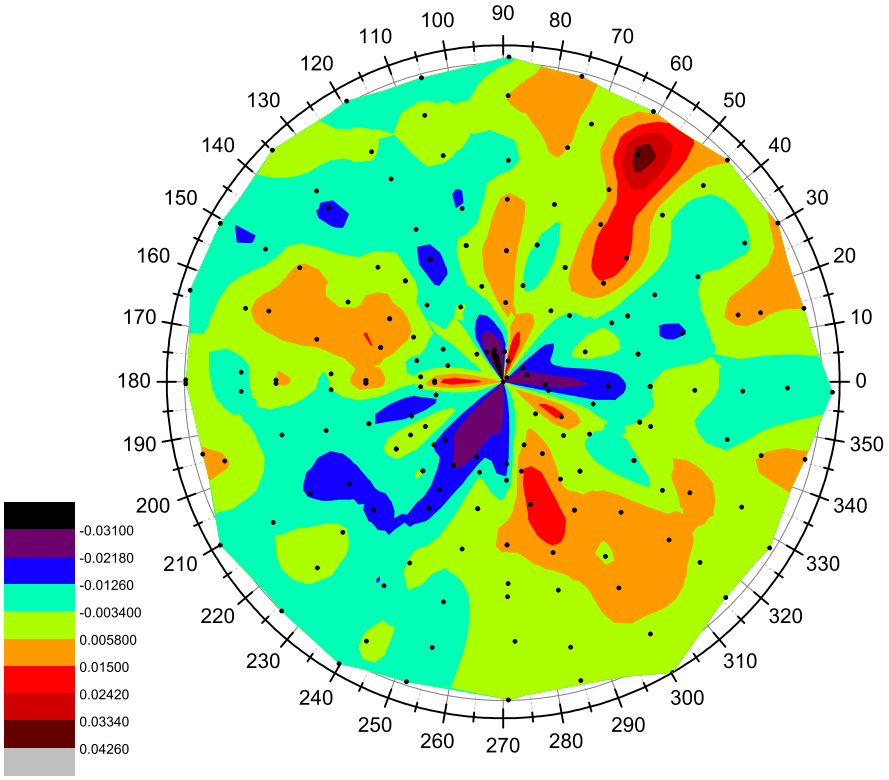

Figure 6.4: Mapping of interaction energy of hydrogen atoms around a screw dislocation core.

240°. Such dependency has its large effect when hydrogen located at $2b$ to $20b$ distances from dislocation core and it is a short range effect.

6.3.2 Peierls potentials

By plotting stress versus strain in the NVT shear process, the shear modulus μ can be obtained by linear fitting of elastic region, and the stress at time when dislocation moves large distance is the Peierls stress σ_p. The energy of a straight dislocation line is $E = E_{core} + Kb^3 ln(R/r_c)$ per b (114), where E_{core} is dislocation core energy, K depends on the elastic constants, R is a long-range cutoff, and r_c is short-range cutoff. We took a $r_c = 2b$ and the E_{core} was obtained by subtract the potential energy of perfect lattice from that of a dislocation-centred cylinder with $R = r_c$. The σ_p, μ, and E_{core} for dislocation with different hydro-

Table 6.1: Peierls stress (σ_p), Shear modulus(μ) and dislocation core energy (E_{core}) at different hydrogen concentrations.

C_H (nm^{-1})	σ_p (GPa)	μ(GPa)	E_{core} (meV/Å)
edge-0	0.057	74.58	395.74
edge-0.05	0.045	71.48	387.90
edge-0.14	0.028	71.08	361.16
edge-0.24	0.024	65.32	332.45
edge-0.33	0.019	57.37	306.91
edge-0.43	0.013	52.25	284.20
screw-0	0.90	69.93	278.59
screw-0.10	0.46	69.70	263.19
screw-0.30	0.32	69.55	210.03
screw-0.51	0.30	69.47	155.21
screw-0.71	0.31	69.54	101.67
screw-0.91	0.31	70.77	10.27

gen concentrations are shown in Table 6.1. The σ_p and E_{core} of all dislocations decrease as the number of hydrogen atoms increases. The shear modulus of edge system decreases with the appearance of hydrogen, which indicates that hydrogen can influence the edge dislocation motion via the second order interaction in HELP theory (2), by contrast, μ for screw dislocation system is hardly changed. The expected H interaction with screw dislocation according to the second order interaction was not observed (41, 91).

Figure 6.5 shows energy barriers for dislocations moving at different hydrogen concentrations. In Fig. 6.5a, Peierls potential (E_p) of hydrogen-free edge dislocation is about 0.7 meV/b. With hydrogen the height of barrier decreases and at $C_H = 0.43$ E_p is only 0.05 meV/b. The hydrogen-free screw dislocation in Fig. 6.5b have a E_p around 10 meV/b, which is consistent with the calculation using the classical EAM potential of Mendelev (115). Same as the Medelvel′s potential, there is a local minimum at the $0.5b$ position. This intermediate metastable configuration, already reported in Refs. (116) and (117), corresponds to the split core described by Takeuchi (118). The E_p of screw dislocation also decreases as C_H increases. The camel hump peak changes to a single hump one at C_H higher

than 0.30 nm^{-1}.

6.3.3 Dislocation core structures

Without hydrogen, the migration of edge dislocation has no formation of kinks or change of core structure. Equilibrated hydrogen positions are under the extra atomic plane of edge dislocation as marked with arrow heads in Fig. 6.6. With 0.24 nm^{-1} hydrogen (Fig. 6.6a), a column of atoms propagates towards the [111] direction, with a height of $a[\bar{1}\bar{1}2]$ and width around $a/2[111]$. In the final image, the atoms propagated towards [111] reaches the $1b$ position at first, and the dislocation velocity is increased by hydrogen. At higher hydrogen concentration (Fig. 6.6b), the height of propagated atom columns become longer. At the $0.5b$ position, some of the propagated columns combine with each other and the edge dislocation moves forward in a form similar to the classical kink-pair motion. But the structure here is not exactly a kink structure that always has a bowing-out shape with several Burgers vectors (110). We will recall this structure as hydrogen induced broaden-core in the later discussions. The broaden-core always appears near the H atom positions which locally have low energy per atom, which suggests the decrease of dislocation core energy are responsible for the formation of this core structure.

The core structure of screw dislocation is illustrated using the differential displacement map (DDM) as shown in Fig. 6.7 where the small vectors indicate the relative [111] displacement of neighbouring Fe atoms. The easy-core configuration in Fig. 6.7a(I) and a(III) are typical non-polarized (or non-degenerate) cores (118), and the numbers in the figure represent the dislocation helicity located at each triangle (119). The metastable configuration in Fig. 6.7a(II) contains two +1.0 easy-core structure separated by a hard-core triangle with -1.0 helicity, and this is the so-called split-core structure. The existence of this core structure is a debate (120) and we will discuss it later. The optimised hydrogen positions are located on the migration path of screw dislocation, and $0.7b$ away from the initial dislocation position. In Fig. 6.7b(I), with hydrogen the helicity of triangle at easy-core position changes to +1.1. The displacement vectors near to the hydrogen atoms appear to be heterogeneous, which are connected with the local

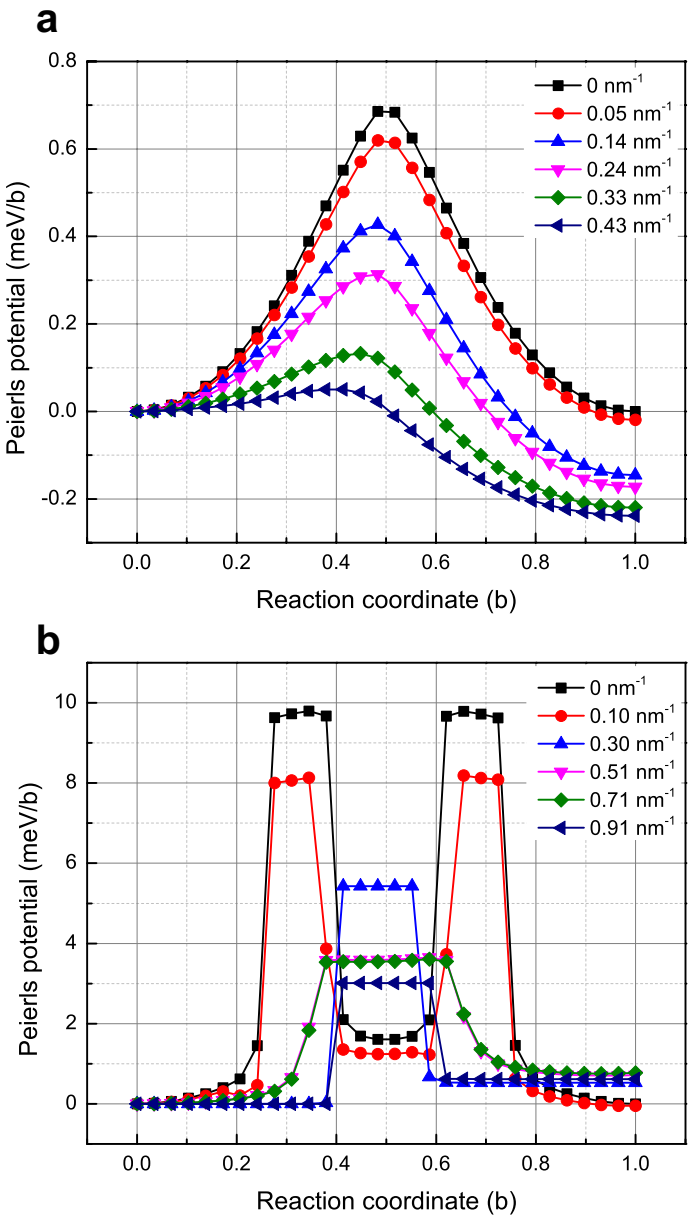

Figure 6.5: Potential energy barriers along MEPs of dislocations with different hydrogen concentrations: (a) edge dislocation; (b) screw dislocation.

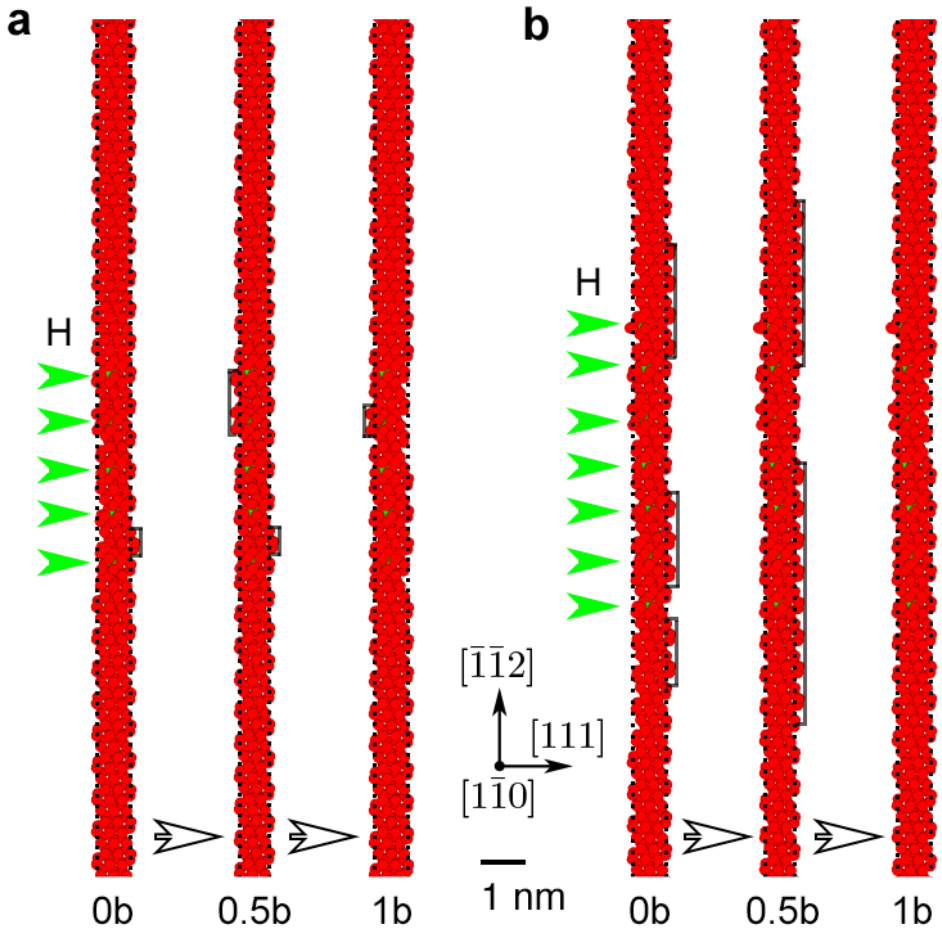

Figure 6.6: The evolution of core structures of edge dislocation at different hydrogen concentrations: (a) at hydrogen concentration of 0.24 nm^{-1} ; (b) at hydrogen concentration of 0.33 nm^{-1}.

strain field induced by hydrogen in different layers. When dislocation migrates to the $0.5b$ position a extra +0.8 core appears in the left of the easy-core position, which is different from the structure of split-core in Fig. 6.7a(II). Such screw core with hydrogen will be called as a quasi-split type in this report. As shown in Fig. 6.7b(III), the final configuration contains two easy-cores with +1.0 and +1.1 helicity separated by a -1.1 hard-core configuration.

6.4 Discussion

Hydrogen influenced screw dislocation motion should be emphasised here, because of high Peierls potential and the unrecoverable jogs it causes. Unlike the edge-H interaction, the shear modulus of screw-H system is unchanged, it indicates that the change of core structure in short range is the main reason for the decreased Peierls potential. As illustrated before, this result is at variance with the guess from HELP theory, which is builded based on assuming isotropic strain field of H atoms.

The Peierls barrier of screw-H changes from camel-hump to single-hump shape. The shape of Peierls barrier is depending on whether the split-core and hard-core are metastable or not (119). Pair and EAM potentials have evidenced the existence of camel-hump (121, 122, 123). However, recently the DFT calculations on iron (119, 120) ruled out the split-core structure as saddle point and support a single-hump. Despite the debate of saddle point, the EAM potentials and DFT simulations agree that screw dislocation migrates between two easy-core positions. According to our results, the final easy-core structure can be changed to a quasi-split core by hydrogen. This core structure have potential energy only 0.5 meV higher than the stable easy-core structure but much lower than the hydrogen free split-core. The single-hump obtained by the EAM potential is a consequence of the core structure. This core structure variation for screw dislocation should take responsibility to the change of dislocation mobility and mechanical property for BCC metals. We note that the screw-H interaction is strongly depending on the hydrogen trapping position (107, 110), investigation using different trap sites is needed in the future work.

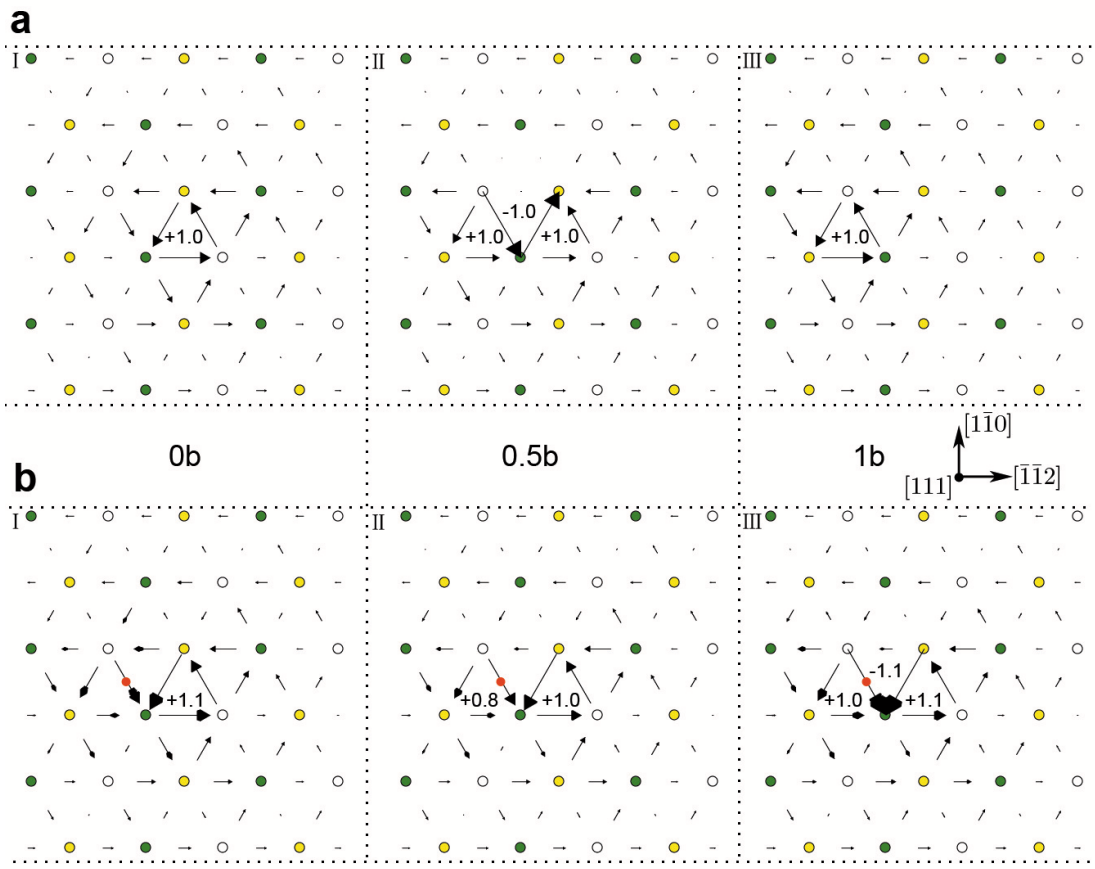

Figure 6.7: The differential displacement maps of screw dislocation with and without hydrogen. Atomic positions are represented by three different colours to emphasise the fact that they belong to three different {111} layers: (a) hydrogen free; (b) at hydrogen concentration of 0.51 nm^{-1}, column of hydrogen atoms is marked with red dots.

6.5 Summary

In summary, we applied the empirical embedded-atom method potentials to investigate the evolution of edge and crew dislocation core structure at different hydrogen concentrations. With hydrogen, the core energy and Peierls potential decreases. The edge dislocation mobility is increased by formation of a broaden-core structure. A quasi-split core structure is observed for screw dislocation with high hydrogen concentration. Because of the formation of such core structure, the screw Peierls barrier changes from camel-hump to single-hump type. Hydrogen influence the screw dislocation motion not due to the change of elastic constants, but the change of core structure.

Chapter 7

Conclusions and recommendations

7.1 Overview

This dissertation focused on studying the pervasive hydrogen embrittlement problems in metals. For more than 130 years, there are many theory model proposed to understanding this problem. The hydrogen embrittlement has been mainly attributed to the hydrogen influenced dislocation mobility by the former researches. However, except the HELP theory, almost all the theory models are lack of evidences. There is a number of independent studies required to gain a better understanding of hydrogen effect on dislocation motion in BCC iron, including:

- Better methods to evaluate the hydrogen-dislocation interactions;
- Understanding the hydrogen-induced softening in BCC metal;
- Relation between hydrogen enhanced plasticity and failure;
- Binding energy of hydrogen trapped in dislocation and hydrogen interaction with different type of dislocations;
- Hydrogen influence on the dislocation core structures.

In order to understand the hydrogen embrittlement mechanism in BCC iron, verify and improve the existed theory model, a series of experimental and computational work has been done in this dissertation. For the first time, the repeat stress relaxation test is applied on iron and ferritic alloy under hydrogen charging environment, and the thermal activation behaviour of dislocation is studied. To understand the possible hydrogen screw dislocation interaction, originally, a computational method combing DFT calculation and classical elastic theory is proposed in this dissertation. The dislocation core structure is studied by DFT based MD simulations. These studies may give a new approach for answering the existed questions and lead to a deep understanding on the hydrogen embrittlement in BCC metals.

7.2 Hydrogen-induced softening in BCC metal

The hydrogen effect on dislocation motion has been discussed based on stress relaxation tests with hydrogen charging. Many common points were found from the result of stress relaxation tests on iron and ferritic alloys.

1. The rate of stress relaxation in iron, Fe-8Cr and F82H are increased by hydrogen.

2. Hydrogen charging decreases the internal stress ratio referring to the same stress for each sample.

3. According to observations of dislocation structure in TEM, the total dislocation shows no difference in all stress relaxation conditions for the same kinds of samples.

4. The mobile dislocation density has shown a low exhausting rate in specimens with hydrogen.

In iron, Fe-8Cr and F82H, hydrogen concentrations have been calculated by the Sievert's law as a function of cathodic current densities. Due to the existing of precipitates in Fe-8Cr model alloy and F82H steel, the hydrogen concentration is 10 times and 100 times more than in pure iron respectively. The mechanism

of hydrogen effect on mechanical properties of these BCC metals are concluded as bellows:

1. At hydrogen concentrations lower than 20 appm, in pure iron the yield stress increases 5 MPa and effective stress decreases slightly. Meanwhile, the effective activation volume is maintained in the same level, which indicates the activated dislocation motion should be driven by a competition of the hydrogen solute drag effect and shielding effect. At high hydrogen concentrations, the hydrogen shielding effect increases linearly as a function of hydrogen concentrations and the solute drag effect is inhibited by the influence too, consequently the effective stress increases steeply and linear reduction of activation volume is found. The immobile dislocations is monitored to have possibility to be activated during stress relaxation with hydrogen. The mobile dislocation density exhausts in slow rate with hydrogen, accompany with the low physical activation volume, the shielding effect induces high density of tangled dislocations. Both of the thermal activation free energy and zero stress activation energy degrade at all hydrogen concentrations, and degradation of the activation energy is observed to be constant under high hydrogen concentrations. The large scale segregation of dislocations would induce pile-ups during plastic deformation. As the dislocations still have high mobility, with sufficient hydrogen concentrations, coalescence of the leading dislocations at the head of a pile-up under external stress, and the initiation of cracks would be encouraged by this mechanism.

2. The short-range interaction of dislocation and energy barrier is the dominator point for the hydrogen effect in BCC metals. This interaction varies the thermal activation energy in a narrow range, but makes the dislocations be tangled or network or even cell structures. The mechanical property changes mainly due to the organised dislocation structures in local area.

3. Hydrogen has two aspect effect in these metals: 1) shielding the dislocation-barrier interaction due to hydrogen concentration difference; 2) impeding dislocation motion in low concentration due to solute-solution effect and

the produced tangled dislocation. Normally the softening will be observed in well annealed steel. However, the two-aspect effect may invoke increase of flow stress in some case, which is depending on the deformation history, surface condition and internal structure of metals.

7.3 Relation between hydrogen enhanced plasticity and failure

In Fe-8Cr and F82H, the hydrogen concentration is higher than in pure iron. The activation volume and internal stress decrease immediately at low cathodic current densities. However, the hydrogen enhanced dislocation motion is impeded by the precipitates, thus the mobile dislocation exhausting rate in these two alloys is higher than in iron. In Fe-8Cr, it induces tangled dislocation between precipitates. In F82H, polygonized and network dislocation structures are found, and obvious embrittlement is found when cathodic current density up to 45 mA/cm^2. The calculation of thermal activation free energy and zero stress activation energy shows that hydrogen reduces the energy barriers between gliding dislocations and the stress field of the pinning obstacles. The large scale segregation of dislocations would induce pile-ups behind precipitates and interfaces, as the dislocations still have high mobility caused by H shielding effect would lead to coalescence of the leading dislocations at the head of a pile-up under external stress, and the formation of cracks will be encouraged by this mechanism.

7.4 Quantification of the hydrogen-dislocation binding energy in iron by DFT

The strain field of H in iron is of crucial importance in understanding the H-dislocation interactions. By introducing the analysis of electron structure of H-BCC iron system and the strain field of H atom based on DFT, this dissertation find that H in BCC iron can increase the electron densities at tetrahedral sites and vacancy, and that the hydrogen-enhanced metallic character of inter-atomic bonds can increase the mobility of dislocations and contribute to the HELP theory. Two

components of strain tensor for H interstitial atom are calculated to be unequal, which is expected to cause elastic interaction of H with screw dislocations, as it does with edge dislocations. For the angular dependence of H-edge dislocations interaction, H atoms prefer to stay under extra atomic plane, while for screw dislocation there are more positions for the lowest interaction energy and high local H concentration is possible.

During plastic deformation, the cross slip of perfect screw dislocation is more important than the behavior of edge dislocations, for the unrecoverable jogs it forms. It has been pointed out that hydrogen atom influence the cross slip of perfect screw dislocation in FCC mainly by screening interaction of two edge partials, but the theory can not be applied to BCC metal directly due to there is no partial dislocations. By comparing the accumulation of H around a screw and an edge dislocation, one can find that the segregation of H atom takes place only below the glide plane of an edge dislocation but all around a screw dislocation, roughly the screw can bind twice as many H atoms as an edge dislocation. Although the elastic interaction energy away from the screw dislocation core is much less than the case of edge dislocation, increase of local H concentration could magnify the H-screw interactions and influence the mechanical property of BCC metals. Combing the DFT calculation with the repeated transients tests for H-charged α-iron, it indicates that significant hydrogen enhanced plasticity can be observed with relative high H concentrations. In those cases, the H-screw interaction should be considered, and it is possible to lead for a new understanding of hydrogen embrittlement in BCC iron.

7.5 Hydrogen altered dislocation core structures

In the HELP mode the screw-H interaction is ruled out due to a assumption of isotropic strain field for H atoms. This assumption have no problem with FCC metals, as argued in the DFT calculation part of this dissertation, due to the anisotropic strain field of H atoms in BCC metals, the screw dislocation and hydrogen interaction is possible. From our stress relaxation texts, this interaction could be a short-range type, and the core dislocation structure may dominate

the hydrogen effect in BCC metal. In order to provide this point, the empirical embedded-atom method potentials is employed in this dissertation and the evolution of edge and crew dislocation core structure is calculated at different hydrogen concentrations.

With hydrogen, the core energy and Peierls potential decreases for all dislocations. The edge dislocation mobility is increased by formation of a broaden-core structure. A quasi-split core structure is observed for screw dislocation with hydrogen, this core structure have potential energy only 0.5 meV higher than the stable easy-core structure but much lower than the hydrogen free split-core. For the formation of such core structure, the screw Peierls barrier changes from camel-hump to single-hump type. Unlike the edge-H interaction, the shear modulus of screw dislocation system is unchanged, and it indicates that the change of core structure in short range is the main reason for the decrease of Peierls potential. Hydrogen influence the screw dislocation motion in BCC iron not due to the change of elastic constants, but the change of core structure.

7.6 Recommendations for the future work

The problem of H-dislocation interactions is much complicated, it is not possible to explain the the hydrogen embrittlement with one theory model. While this dissertation has answered the research questions related to hydrogen-dislocation interactions posed in Chapter 1, further research questions also arise from this better understanding. Some potential research areas are as follows:

1. ***Organised dislocation effect on the mechanical properties.*** In this dissertation, tangled dislocation is found to impeding the further movement of mobile dislocations, though all dislocations become to move in a high velocity with high enough hydrogen concentration. This change process could be investigated by *in situ* TEM or MD simulation, and the hydrogen embrittlement may be controllable by producing center dislocation structure in metals. The organised dislocation structures also observed in ferritic alloys, which may have strong connection to the fracture model of hydrogen embrittlement.

2. ***Mechanism for the formation of intergranular fracture.*** The cell structures observed under surface of iron intergranular fracture have commonalities to the small size grain boundaries in fine grain metals. It is possible that such structures can arrest the dislocation emitting from the crack tip, and force the crack to propagate along grain boundaries. This research have potential for understanding the connection between fracture surface and the dislocation structure just beneath it.

3. ***Methods for mitigating hydrogen effects need to be determined and validated.*** Connecting with the mechanical properties, those methods could pay attention to the grain size, microstructure, surface treatments, new alloys, coatings, liners etc..

4. ***Dislocation core structure change by different interstitial atoms.*** As emphasised in this dissertation, the core structure variation must be verified by more accurate calculations and observations. A detail study on interstitial atom effect in BCC metal by using DFT can give us a deep understanding to the solute effect in different materials. Advances in electron microscopes (TEM, HRTEM and STEM, etc.) offer an exciting opportunity in this point.

5. ***What makes hydrogen so special?*** This is a question cannot be answered if we do not research the hydrogen effect for a wide range of materials. And also the similar study may be made to different interstitials, interstitial clusters, and even interstitial-vacancy clusters. The binding-energy, electron structure, and Griffith potency could be listed.

References

[1] P J Ferreira, I M Robertson, and H K Birnbaum. **Hydrogen Effects on the Interaction Between Dislocations**. *Acta Materialia*, **46**(5):1749–1757, 1998. vii, 14, 16, 20, 24, 67

[2] H K Birnbaum and P Sofronis. **Hydrogen-Enhanced Localized Plasticity— A Mechanism for Hydrogen-Related Fracture**. *Materials Science and Engineering: A*, **176**(1–2):191–202, 1994. vii, 1, 13, 15, 16, 50, 66, 67, 76, 86

[3] J Völkl and G Alefeld. **Diffusion of Hydrogen in Metals**. In Georg Alefeld and Johann Völkl, editors, *Topics in Applied Physics*, pages 321–348. Springer Berlin / Heidelberg, 1978. xi, 8

[4] W H Johnson. **On Some Remarkable Changes Produced in Iron and Steel by the Action of Hydrogen and Acids**. In *Proceedings of the Royal Society of* , 1874. 1

[5] R A Oriani and P H Josephic. **Equilibrium Aspects of Hydrogen-Induced Cracking of Steels**. *Acta Metallurgica*, **22**(9):1065–1074, 1974. 1, 12

[6] J P Hirth. **Effects of Hydrogen on the Properties of Iron and Steel**. *Metallurgical and Materials Transactions A*, **11**(6):861–890, 1980. 1, 9, 11, 29, 58

[7] S M Myers, M I Baskes, H K Birnbaum, J W Corbett, G G Deleo, S K Estreicher, E E Haller, P Jena, N M Johnson, R Kirchheim, S J Pearton, and M J Stavola. **Hydrogen Interactions With Defects in Crystalline Solids**. *Reviews of Modern Physics*, **64**(2):559–617, 1992. 1

[8] C J Mcmahon Jr. **Hydrogen-Induced Intergranular Fracture of Steels**. *Engineering Fracture Mechanics*, **68**(6):773–788, 2001. 1

[9] A W Thompson. **The Relation Between Changes in Ductility and in Ductile Fracture Topography: Control by Microvoid Nucleation**. *Acta Metallurgica*, **31**(10):1517–1523, 1983. 1

[10] M Nagumo, M Nakamura, and K Takai. **Hydrogen Thermal Desorption Relevant to Delayed-Fracture Susceptibility of High-Strength Steels**. *Metallurgical and Materials Transactions A*, **32**(2):339–347, 2001. 1

[11] Y Murakami, T Kanezaki, and Y Mine. **Hydrogen Effect Against Hydrogen Embrittlement**. *Metallurgical and Materials Transactions A*, **41**(10):2548–2562, 2010. 1

[12] S Bechtle, M Kumar, B P Somerday, M E Launey, and R O Ritchie. **Grain-Boundary Engineering Markedly Reduces Susceptibility to Intergranular Hydrogen Embrittlement in Metallic Materials**. *Acta Materialia*, **57**(14):4148–4157, 2009. 1

[13] T Michler and M P Balogh. **Hydrogen Environment Embrittlement of an ODS RAF Steel – Role of Irreversible Hydrogen Trap Sites**. *International Journal of Hydrogen Energy*, **35**(18):9746–9754, 2010. 1

[14] M Beghini, G Benamati, L Bertini, I Ricapito, and R Valentini. **Effect of Hydrogen on the Ductility Reduction of F82H Martensitic Steel After Different Heat Treatments**. *Journal of Nuclear Materials*, **288**(1):1–6, 2001. 1

[15] K Splichal, J Berka, J Burda, and M Falcn Ík. **Hydrogen Embrittlement and Fracture Mode of Eurofer 97 Ferritic-Martensitic Steel**. *International Journal of Pressure Vessels and Piping*, **89**(0):42–47, 2012. 1

[16] C san Marchi, D K Balch, K Nibur, and B P Somerday. **Effect of High-Pressure Hydrogen gas on Fracture of Austenitic Steels**. *Journal of Pressure Vessel Technology*, **130**(4):041401(9 Pages), 2008. 1, 52

[17] A M Brass and J Chene. **Influence of Deformation on the Hydrogen Behavior in Iron and Nickel Base Alloys: a Review of Experimental Data**. *Materials Science and Engineering: A*, **242**(1):210–221, 1998. 1

[18] G Muller, M Uhlemann, A Ulbricht, and J Bohmert. **Influence of Hydrogen on the Toughness of Irradiated Reactor Pressure Vessel Steels**. *Journal of Nuclear Materials*, **359**(1-2):114–121, 2006. 1

[19] H Matsui, H Kimura, and S Moriya. **Effect of Hydrogen on the Mechanical-Properties of High-Purity Iron 1 Softening and Hardening of High-Purity Iron by Hydrogen Charging During Tensile Deformation**. *Materials Science and Engineering*, **40**(2):207–216, 1979. 1

[20] S Moriya, H Matsui, and H Kimura. **Effect of Hydrogen on the Mechanical-Properties of High-Purity Iron 2 Effect of Quenched-in Hydrogen Below Room-Temperature**. *Materials Science and Engineering*, **40**(2):217–225, 1979. 1

[21] T Boniszewski and G C Smith. **Influence of Hydrogen on Plastic Deformation Ductility, and Fracture of Nickel in Tension**. *Acta Metallurgica*, **11**(3):165–178, 1963. 1

[22] B E Wilde and T Shimada. **Surface Modification - a Potential new Approach to Combatting Hydrogen Induced Fracture in Steel**. *Scripta Metallurgica*, **22**(4):551–556, 1988. 1

[23] A Kimura and H K Birnbaum. **On the Kinetics of Intergranular Embrittlement of Nickel by Hydrogen Transport from the External Surface**. *Scripta Metallurgica*, **21**(2):219–222, 1987. 1, 2

[24] J W Watson, Y Z Shen, and M Meshii. **Effect of Cathodic Charging on the Mechanical-Properties of Aluminum**. *Metallurgical Transactions A*, **19**(9):2299–2304, 1988. 1

[25] S Ohnuki, T Yasuda, T Suda, S Watanabe, and B M Oliver. **Effect of Alloying Elements and Neutron-Irradiation on Hydrogen Behavior in V Alloys**. *Journal of Nuclear Materials*, **329**:481–485, 2004. 1

[26] D P Abraham and C J Altstetter. **The Effect of Hydrogen on the Yield and Flow-Stress of an Austenitic Stainless-Steel**. *Metallurgical and Materials Transactions A*, **26**(11):2849–2858, 1995. 2, 19, 25

[27] M Maxelon, A Pundt, W Pyckhout-Hintzen, and R Kirchheim. **Small Angle Neutron Scattering of Hydrogen Segregation at Dislocations in Palladium**. *Scripta Materialia*, **44**(5):817–822, 2001. 2, 48, 67

[28] R Kirchheim. **Reducing Grain Boundary, Dislocation Line and Vacancy Formation Energies by Solute Segregation:: ii Experimental Evidence and Consequences**. *Acta Materialia*, **55**(15):5139–5148, 2007. 2, 48, 67

[29] A Donato and R Andreani. **Material Requirements and Perspectives for Future Thermonuclear Fusion Reactors**. *Fusion Technology*, **29**(1):58–72, 1996. 2

[30] E Serra and G Benamati. **Hydrogen Behaviour in Aged low Activation Martensitic Steel F82H for Fusion Reactor Applications**. *Materials Science and Technology*, **14**(6):573–578, 1998. 2

[31] M L Grossbeck, K Ehrlich, and C Wassilew. **An Assessment of Tensile, Irradiation Creep, Creep Rupture, and Fatigue Behavior in Austenitic Stainless Steels With Emphasis on Spectral Effects**. *Journal of Nuclear Materials*, **174**(2–3):264–281, 1990. 2

[32] O V Ogorodnikova, M A FüTterer, E Serra, and G Benamati. **Calculations of the Tritium re-Emission Rate in the Demo First Wall**. *Journal of Nuclear Materials*, **270**(3):368–371, 1999. 2

[33] J W Davis and D J Michel, editors. *Proceedings of the Topical Conference on Ferritic Alloys for use in Nuclear Energy Technology*. TMS–AIME, 1984. 2

[34] H Hagi, Y Hayashi, and N Ontani. **Diffusion Coefficient of Hydrogen in Pure Iron Between 230 and 300 K**. *Trans jim*, 1979. 7, 8

[35] R A Oriani. **The Diffusion and Trapping of Hydrogen in Steel**. *Acta Metallurgica*, **18**(1):147–157, 1970. 7, 8, 28

[36] J J Au and H K Birnbaum. **Magnetic Relaxation Studies of the Motion of Hydrogen and Deuterium in Iron**. *Acta Metallurgica*, **26**(7):1105–1116, July 1978. 9

[37] W Y Choo and J Y Lee. **Thermal Analysis of Trapped Hydrogen in Pure Iron**. *Metallurgical and Materials Transactions A*, 1982. 9

[38] A J Kumnick and H H Johnson. **Deep Trapping States for Hydrogen in Deformed Iron**. *Acta Metallurgica*, **28**(1):33–39, January 1980. 9

[39] E Chornet and R W Coughlin. **Chemisorption of Hydrogen on Iron**. *Journal of Catalysis*, 1972. 9

[40] G Meyrick and R Wagoner. **Physical Metallurgy of Steel**. *Class Notes and Lecture Material for MSE*, 2001. 8, 10

[41] J P Chateau, D Delafosse, and T Magnin. **Numerical Simulations of Hydrogen-Dislocation Interactions in FCC Stainless Steels Part 1: Hydrogen-Dislocation Interactions in Bulk Crystals**. *Acta Materialia*, **50**(6):1507–1522, 2002. 8, 13, 20, 24, 47, 60, 67, 76, 79, 86

[42] A Seeger. **Positive Muons as Light Isotopes of Hydrogen**. In Georg Alefeld and Johann Völkl, editors, *Topics in Applied Physics*, pages 349–397. Springer Berlin / Heidelberg, 1978. 9

[43] H Kanzaki. **Point Defects in Face-Centred Cubic Lattice—I Distortion Around Defects**. *Journal of Physics and Chemistry of Solids*, **2**(1):24–36, March 1957. 9

[44] G Bauer, E Seitz, H Horner, and W Schmatz. **Lattice Distortions due to Deuterium in Niobium**. *Solid State Communications*, 1975. 11

[45] H. Peisl. **Lattice Strains due to Hydrogen in Metals**. In Georg Alefeld and Johann Völkl, editors, *Hydrogen in Metals i*, **28** of *Topics in Applied Physics*, pages 53–74. Springer Berlin / Heidelberg, 1978. 11

[46] H Metzger and H Peisl. **Huang Diffuse X-ray Scattering from Lattice Strains in High-Concentration ta-h Alloys**. *Journal of Physics f: Metal Physics*, **8**(3):391–402, January 1978. 11

[47] K Takita and K Sakamoto. **low Temperature Internal Friction Peak and Hydrogen Cold-Work Peak in Deformed α-Iron**. *Scripta Metallurgica*, **10**(5):399–403, 1976. 11

[48] V G Gavriljuk, V N Shivanyuk, and B D Shanina. **Change in the Electron Structure Caused by C, N and H Atoms in Iron and its Effect on Their Interaction With Dislocations**. *Acta Materialia*, **53**(19):5017–5024, 2005. 11, 73

[49] I M Robertson, H K Birnbaum, and P Sofronis. *Dislocations in Solids*, **15** of *Dislocations in Solids15724859*. Elsevier, 2009. 11, 42

[50] R A Oriani. **A Mechanistic Theory of Hydrogen Embrittlement of Steels**. *Berichte der Bunsengesellschaft für Physikalische Chemie*, **76**(8):848–857, 1972. 12

[51] R A Oriani. **Hydrogen Embrittlement of Steels**. *Annual Review of Materials Science*, **8**(1):327–357, August 1978. 12

[52] S P Lynch. **Environmentally Assisted Cracking: Overview of Evidence for an Adsorption-Induced Localised-Slip Process**. *Acta Metallurgica*, **36**(10):2639–2661, October 1988. 12

[53] C D Beachem. **A new Model for Hydrogen-Assisted Cracking (Hydrogen "Embrittlement")**. *Metallurgical Transactions*, **3**(2):441–455, February 1972. 12

[54] E Sirois and H K Birnbaum. **Effects of Hydrogen and Carbon on Thermally Activated Deformation in Nickel**. *Acta Metallurgica et Materialia*, **40**(6):1377–1385, 1992. 13, 14, 19, 25, 47, 50, 52, 65

[55] D S Shih, I M Robertson, and H K Birnbaum. **Hydrogen Embrittlement of Alpha-Titanium - insitu TEM Studies**. *Acta Metallurgica*, **36**(1):111–124, 1988. 13

[56] I M Robertson and H K Birnbaum. **An Hvem Study of Hydrogen Effects on the Deformation and Fracture of Nickel**. *Acta Metallurgica*, **34**(3):353–366, 1986. 13, 20, 24

[57] G M Bond, I M Robertson, and H K Birnbaum. **Effects of Hydrogen on Deformation and Fracture Processes in High-Purity Aluminum**. *Acta Metallurgica*, **36**(8):2193–2197, 1988. 13, 20, 24

[58] P Sofronis. **The Influence of Mobility of Dissolved Hydrogen on the Elastic Response of a Metal**. *Journal of the Mechanics and Physics of Solids*, **43**(9):1385–1407, 1995. 13, 20, 24, 47, 60

[59] D Caillard and J L Martin. *Thermally Activated Mechanisms in Crystal Plasticity*. Pergamon, Amsterdam, 2003. 16, 34

[60] P Feltham. **Stress Relaxation in Alpha-Iron at low Temperatures**. *Philosophical Magazine*, **6**(67):847–850, 1961. 16, 25, 55

[61] F Guiu and P L Pratt. **Stress Relaxation and the Plastic Deformation of Solids**. *Physica Status Solidi*, **6**(1):111–120, 1964. 16, 25, 55

[62] D J Lloyd, P J Worthing, and J D Embury. **Dislocation Dynamics in Copper-tin System**. *Philosophical Magazine*, **22**(180):1147–1160, 1970. 16, 25, 55

[63] P Spätig, J Bonneville, and J L Martin. **A new Method for Activation Volume Measurements - Application to Ni3(Al,Hf)**. *Materials Science and Engineering: A*, **167**(1-2):73–79, 1993. 19, 25, 38, 57

[64] R A Oriani and P H Josephic. **Hydrogen-Enhanced Load Relaxation in a Deformed Medium-Carbon Steel**. *Acta Metallurgica*, **27**(6):997–1005, 1979. 19, 25

[65] T Tabata and H K Birnbaum. **Direct Observations of Hydrogen Enhanced Crack-Propagation in Iron**. *Scripta Metallurgica*, **18**(3):231–236, 1984. 20

[66] M A Lee, J L Sundberg, and I H Bernstein. **Frequency, Preference, and the Concurrent Process Model**. *Bulletin of the Psychonomic Society*, **29**(6):508–508, 1991. 20

[67] V G Gavriljuk, V N Bugaev, Y N Petrov, A V Tarasenko, and B Z Yanchitski. **Hydrogen-Induced Equilibrium Vacancies in FCC Iron-Base Alloys**. *Scripta Materialia*, **34**(6):903–907, 1996. 20

[68] W Kohn and L J Sham. **Self-Consistent Equations Including Exchange and Correlation Effects**. *Physical Review*, **140**(4a):A1133–A1138, November 1965. 21

[69] P E Bl'ochl. **Projector Augmented-Wave Method**. *Physical Review B*, **50**(24):17953–17979, December 1994. 22

[70] G Kresse. **Efficient Iterative Schemes for ab initio Total-Energy Calculations Using a Plane-Wave Basis set**. *Physical Review B*, **54**(16):11169–11186, October 1996. 22

[71] D Caillard and J L Martin. *Thermally Activated Mechanisms in Crystal Plasticity*, **8**. Elsevier Science, 2003. 25, 39

[72] J K Tien, A W Thompson, I M Bernstein, and R J Richards. **Hydrogen Transport by Dislocations**. *Metallurgical Transactions A*, **7**(6):821–829, 1976. 26, 56

[73] R Bonade and P Spätig. **The Evolution of the Mobile Dislocation Density During Successive Stress Relaxation Transients**. *Materials Science and Engineering A*, **483-84**:203–206, 2008. 27, 45, 56

[74] R Schäublin and M Victoria. **Differences in the Microstructure of the F82H Ferritic/Martensitic Steel After Proton and Neutron Irradiation**. *Journal of Nuclear Materials*, **283–287, Part 1**(0):339–343, 2000. 27, 57

[75] G Y Chin, W L Mammel, and M T Dolan. **Taylors Theory of Texture for Axisymmetric Flow in Body-Centered Cubic Metals**. *Transactions of the Metallurgical Society of AIME*, **239**(11):1854–1855, 1967. 28

[76] U F Kocks. **Polyslip in Polycrystals**. *Acta Metallurgica*, **6**(2):85–94, 1958. 28

[77] J M Rosenber and H R Piehler. **Calculation of Taylor Factor and Lattice Rotations for BCC Metals Deforming by Pencil Glide**. *Metallurgical Transactions*, **2**(1):257–259, 1971. 28

[78] D L Johnson and J K Wu. **Hydrogen Transport in Carbon Steels as a Function of Carbon Content and Heat Treatment Near 298 k**. *Journal of Materials for Energy Systems*, **8**(4):402–408, 1987. 29, 58

[79] J K Wu. **Electrochemical Method for Studying Hydrogen in Iron, Nickel and Palladium**. *International Journal of Hydrogen Energy*, **17**(12):917–921, 1992. 29

[80] J R Davis. *Metals Handbook: Desk Edition*. crc Press, 2nd edition, 1998. 29, 58

[81] P Sofronis, Y Liang, and N Aravas. **Hydrogen Induced Shear Localization of the Plastic Flow in Metals and Alloys**. *European Journal of Mechanics-a/Solids*, **20**(6):857–872, 2001. 29, 57

[82] H Hagi. **Diffusion Coefficient of Hydrogen in Iron Without Trapping by Dislocations and Impurities**. *Materials Transactions*, **35**:112–117, 1994. 29, 58

[83] H Conrad. **Grain Size Dependence of the Plastic Deformation Kinetics in cu**. *Materials Science and Engineering: A*, **341**(1):216–228, 2003. 34, 44

[84] A H Cottrell. *Dislocations and Plastic Flows in Crystals*. Oxford University Press, London, 1953. 35

[85] P Groh and R Conte. **Stress Relaxation and Creep in Alpha-Iron Filamentary Single Crystals at low Temperature**. *Acta Metallurgica*, **19**(9):895–902, 1971. 35

[86] T Kruml, O Coddet, and JL Martin. **About the Determination of the Thermal and Athermal Stress Components from Stress-Relaxation Experiments**. *Acta Materialia*, **56**(3):333–340, 2008. 36, 49

[87] E W Hart. **Theory of the Tensile Test**. *Acta Metallurgica*, **15**(2):351–355, 1967. 38

[88] David B Williams and C Barry Carter. *Transmission Electron Microscopy: a Textbook for Materials Science* . Springer US, Boston, MA, 2009. 41

[89] R Kirchheim. **Revisiting Hydrogen Embrittlement Models and Hydrogen-Induced Homogeneous Nucleation of Dislocations**. *Scripta Materialia*, **62**(2):67–70, 2010. 45, 63

[90] G A Sargent. **Stress Relaxation and Thermal Activation in Niobium**. *Acta Metallurgica*, **13**(6):663–671, 1965. 47, 60

[91] P Sofronis and H K Birnbaum. **Mechanics of the Hydrogen-Dislocation-Impurity Interactions 1 Increasing Shear Modulus**. *Journal of the Mechanics and Physics of Solids*, **43**(1):49–90, 1995. 47, 50, 79, 86

[92] H Wiedersich. **Hardening Mechanisms and the Theory of Deformation**. *Journal of Metals*, **15**:423–428, 1963. 49

[93] A.W Cochardt, G Schoek, and H Wiedersich. **Interaction Between Dislocations and Interstitial Atoms in Body-Centered Cubic Metals**. *Acta Metallurgica*, **3**(6):533–537, 1955. 70, 71, 72, 76

[94] John P. Perdew, Kieron Burke, and Matthias Ernzerhof. **Generalized Gradient Approximation Made Simple**. *Physics Review Letter*, **77**:3865–3868, 1996. 71

[95] J. J. Mortensen, L. B. Hansen, and K. W. Jacobsen. **Real-Space Grid Implementation of the Projector Augmented Wave Method**. *Physics Review: B*, **71**:035109, 2005. 71

[96] M KöRling and J HäGlund. **Cohesive and Electronic Properties of Transition Metals: the Generalized Gradient Approximation**. *Physics Review: B*, **45**:13293–13297, 1992. 71

[97] John Hirth. **Effects of Hydrogen on the Properties of Iron and Steel**. *Metallurgical and Materials Transactions A*, **11**:861–890, 1980. 71

[98] Hendrik J. Monkhorst and James D. Pack. **Special Points for Brillouin-Zone Integrations**. *Physics Review: B*, **13**:5188–5192, 1976. 71

[99] James D. Pack and Hendrik J. Monkhorst. **"Special Points for Brillouin-Zone Integrations"–a Reply**. *Physics Review: B*, **16**:1748–1749, 1977. 71

[100] V Cocula, CJ Pickard, and EA Carter. **Ultrasoft Spin-Dependent Pseudopotentials**. *Journal of Chemical Physics*, **123**, 2005. 71

[101] W Tang, E Sanville, and G Henkelman. **A Grid-Based Bader Analysis Algorithm Without Lattice Bias**. *Journal of Physics: Condensed Matter*, **21**(8):084204, 2009. 71

[102] R. F. W. Bader. *Atoms in Molecules: A Quantum Theory*. Oxford University Press, 1990. 71

[103] G J Ackland, M I Mendelev, D J Srolovitz, S han, and A V Barashev. **Development of an Interatomic Potential for Phosphorus Impurities in α-Iron**. *Journal of Physics: Condensed Matter*, **16**(27):S2629, 2004. 71

[104] J. Callaway and C. S. Wang. **Energy Bands in Ferromagnetic Iron**. *Physics Revive: b*, **16**:2095–2105, sep 1977. 73

[105] M E Pronsato, G Brizuela, and A Juan. **The Electronic Structure and Location of H Pairs in BCC Fe Edge Dislocation**. *Applied Surface Science*, **173**(3–4):368–379, 2001. 73

[106] S M Teus, V N Shivanyuk, B D Shanina, and V G Gavriljuk. **Effect of Hydrogen on Electronic Structure of FCC Iron in Relation to Hydrogen Embrittlement of Austenitic Steels**. *Physica Status Solidi (A)*, **204**(12):4249–4258, 2007. 73

[107] Shuai Wang, Keisuke Takahashi, Naoyuki Hashimoto, Shigehito Isobe, and Somei Ohnuki. **Strain Field of Interstitial Hydrogen Atom in Body-Centered Cubic Iron and its Effect on Hydrogen–Dislocation Interaction**. *Scripta Materialia*, **68**:249–252, March 2013. 79, 90

[108] A Ramasubramaniam, M Itakura, and E A Carter. **Phys. rev. b 79, 174101 (2009): Interatomic Potentials for Hydrogen in α–Iron Based on Density Functional Theory**. *Physical Review B*, 2009. 79, 80, 83

[109] Byeong joo lee and je Wook Jang. **A Modified Embedded-Atom Method Interatomic Potential for the Fe–H System**. *Acta Materialia*, **55**(20):6779–6788, December 2007. 79

[110] M wen, S Fukuyama, and K Yokogawa. **Atomistic Simulations of Effect of Hydrogen on Kink-Pair Energetics of Screw Dislocations in BCC Iron**. *Acta Materialia*, **51**(6):1767–1773, April 2003. 79, 87, 90

[111] Steve Plimpton. **Fast Parallel Algorithms for Short-Range Molecular Dynamics**. *Journal of Computational Physics*, **117**(1):1 – 19, 1995. 80

[112] W Cai, J Li, and S Yip. **Molecular Dynamics**. In Rudy J M Konings, editor, *Comprehensive Nuclear Materials*, pages 249–265. Elsevier, Oxford, 2012. 80

[113] J Dana Honeycutt and Hans C Andersen. **Molecular Dynamics Study of Melting and Freezing of Small Lennard-Jones Clusters**. *The Journal of Physical Chemistry*, **91**(19):4950–4963, September 1987. 80

[114] John P Hirth and Jens Lothe. *Theory of Dislocations*. John Wiley & Sons, new York, 2ed edition, 1982. 80, 85

[115] M I Mendelev, S Han, D J Srolovitz, G J Ackland, D Y Sun, and M Asta. **Development of new Interatomic Potentials Appropriate for Crystalline and Liquid Iron**. *Philosophical Magazine*, **83**(35):3977–3994, December 2003. 86

[116] Christophe Domain and Ghiath Monnet. **Simulation of Screw Dislocation Motion in Iron by Molecular Dynamics Simulations**. *Physical Review Letters*, **95**(21):215506, November 2005. 86

[117] J Chasussidon, M Fivel, and D Rodney. **The Glide of Screw Dislocations in BCC Fe: Atomistic Static and Dynamic Simulations**. *Acta Materialia*, **54**(13):3407–3416, August 2006. 86

[118] S Takeuchi. **Core Structure of a Screw Dislocation in the b.c.c. Lattice and its Relation to Slip Behaviour of α-Iron**. *Philosophical Magazine*, **39**(5):661–671, May 1979. 86, 87

[119] M Itakura, H Kaburaki, and M Yamaguchi. **First-Principles Study on the Mobility of Screw Dislocations in BCC Iron**. *Acta Materialia*, **60**(9):3698–3710, May 2012. 87, 90

[120] Lisa Ventelon and F Willaime. **Core Structure and Peierls Potential of Screw Dislocations in α-Fe from First Principles: Cluster Versus Dipole Approaches**. *Journal of Computer-Aided Materials Design*, **14**(s1):85–94, January 2008. 87, 90

[121] P A Gordon, T Neeraj, Y Li, and J Li. **Screw Dislocation Mobility in BCC Metals: The Role of the Compact Core on Double-Kink Nucleation**. *Modelling and Simulation in Materials Science and Engineering*, **18**(8):085008, November 2010. 90

[122] Mark R Gilbert and Sergei L Dudarev. **Ab initio Multi-string Frenkel–Kontorova Model for a b = a/2[111] Screw Dislocation in BCC Iron**. *Philosophical Magazine*, **90**(7-8):1035–1061, March 2010. 90

[123] Keiichi Edagawa, Takayoshi Suzuki, and Shin Takeuchi. **Motion of a Screw Dislocation in a two-Dimensional Peierls Potential**. *Physical Review B*, **55**(10):6180–6187, March 1997. 90

Declaration

I herewith declare that I have produced this paper without the prohibited assistance of third parties and without making use of aids other than those specified; notions taken over directly or indirectly from other sources have been identified as such. This paper has not previously been presented in identical or similar form to any other Japan or foreign examination board.

Signature:

Academic Achievement

Journal Articles

1. May L. Martin, Shuai Wang, Akihide Nagao, Mohsen Dadfarnia, Somei Ohnuki, Naoyuki Hashimoto, Petros Sofronis, Ian M. Robertson. Preparing. *Commonalities between liquid metal and hydrogen embrittlement of metals*
2. Shuai Wang, Naoyuki Hashimoto, Somei Ohnuki. Submitted. *Hydrogen-induced change in core structures of edge and screw dislocations in body-centered cubic iron*
3. Shuai Wang, Naoyuki Hashimoto, Yongming Wang, Somei Ohnuki. In Press, Available online 31 May 2013, Acta Materialia, 2013. *Activation volume and density of mobile dislocations in hydrogen charged Fe*
4. Shuai Wang, Keisuke Takahashi, Naoyuki Hashimoto, Shigehito Isobe, Somei Ohnuki. Scripta Materialia, 2013, 68 (5), 249–252. *Strain field of interstitial hydrogen atom in body-centered cubic iron and its effect on hydrogen-dislocation interaction*
5. Shuai Wang, Naoyuki Hashimoto, Somei Ohnuki. Materials Science & Engineering A, 2013, 562, 101–108. *Effects of hydrogen on activation volume and density of mobile dislocations in iron-based alloy*

6. Shuai Wang, Somei Ohnuki, Naoyuki Hashimoto, Keisuke Chiba Materials Science & Engineering A, 2013, 560, 332–338. *Hydrogen effects on tensile property of pure iron with deformed surface*

7. Shaoning Jiang, Farong Wan, Yi Long, Jianchao He, Shuai Wang, Somei Ohnuki. Gongneng Cailiao/Journal of Functional Materials, 2013, 44(2), 262–265. *Effect of isotope on irradiation damage in pure iron*

8. Tao Ma, Shigehito Isobe, Keisuke Takahashi, Yongming Wang, Shuai Wang, Naoyuki Hashimoto, and Somei Ohnuki. Journal of Physics and Chemistry C, 2012, 116 (32), 17089–17093. *Phase transition of Mg during hydrogenation of Mg-Nb_2O_5 evaporated composites*

9. Xianghua Kong, Shuai Wang, Yanhui Sun, Jianliang Zhang, Xiang Li, Facang Wang, Jianlin Geng Advanced Materials Research, 2010, 146–147, 301–305 *Analysis of carbide precipitates in API X80 medium-thickness plate*

10. Xianghua Kong, Shuai Wang, Haiping Zhao, Yedong He. Thin Solid Films, 2010, 518(15), 4211–4214. *Preparation of diamond-like carbon films by cathodic micro-arc discharge, in aqueous solutions*

Presentations on conferences

1. 2013, 2013 spring annual meeting of Japan institute of metals. *Hydrogen-dislocation interaction induced by an anisotropic strain field of interstitial hydrogen atom in body-centered cubic iron*

2. 2012, 2012 fall annual meeting of Japan institute of metals. *Hydrogen effect on thermal activation of dislocation motion in Fe and Fe-Cr based steel*

3. 2011, 2011 FALL ANNUAL MEETING OF JAPAN INSTITUTE OF METALS. *Investigation of Hydrogen-Dislocation Interaction in Fe-based Alloys by Dynamic Cathodic Hydrogen Charging Test*
4. 2010, 10TH JCS, HOLD BY ASIA CORE AT KYOTO UNIVERSITY. *Effect of He and H on Micro-structural Evolution in Ferritic/martensitic Steels During Irradiation.*